日本磁気学会
ISSN 2432-0250
Journal of the Magnetics Society of Japan
Electronic Journal URL: https://www.jstage.jst.go.jp/browse/msjmag

Vol.47 No.4 2023

Journal

JOURNAL OF THE MAGNETICS SOCIETY OF JAPAN

Vol.47 No.4 2023

日本磁気学会

ISSN 2432-0250

HP: http://www.magnetics.jp/ e-mail: msj@bj.wakwak.com

Electronic Journal: http://www.jstage.jst.go.jp/browse/msjmag

Journal of the Magnetics Society of Japan
Vol. 47, No. 4

Electronic Journal URL: https://www.jstage.jst.go.jp/browse/msjmag

CONTENTS

J. Magn. Soc. Jpn., **47**, 84-89 (2023)

<Review>

Dynamic magnetization process of magnetic nanoparticles for biomedical applications

Yasushi Takemura, Suko Bagus Trisnanto, and Satoshi Ota*

Division of Electrical and Computer Engineering, Yokohama National University, Yokohama 240-8501, Japan

*Department of Electrical and Electronic Engineering, Shizuoka University, Hamamatsu 432-8561, Japan

Magnetic nanoparticles have been used in various biomedical applications. Among these, magnetic particle imaging and hyperthermia are considered clinically useful diagnostic and therapeutic methods, respectively. An alternating magnetic field is applied to the magnetic nanoparticles in these methods. The magnetization response of a magnetic nanoparticle is essential, and the dependence of its field intensity and frequency determines its diagnostic and therapeutic performance. This article reviews the fundamental issues of the magnetization process and magnetization relaxation of magnetic nanoparticles and presents our recent experimental results.

Keywords: magnetic nanoparticles, superparamagnetic nanoparticles, magnetization relaxation, Brownian relaxation, Néel relaxation, hyperthermia, magnetic particle imaging.

1. Introduction

This article introduces the dynamic magnetization process of magnetic nanoparticles (MNPs) for biomagnetic applications, which was a research subject of MSJ Outstanding Research Award 2022.

The main subject in this article is the measurement and analysis of dynamic magnetization in MNPs by carrying out alternating current (AC) magnetization hysteresis and magnetization measurements under a pulsed magnetic field. Then, we elucidated the two-step magnetization process of the Néel and Brownian relaxations from these measurements. Although this two-step process has not been conventionally discussed, it is important to understand the magnetization properties of MNPs, particularly for biomedical applications such as hyperthermia and magnetic particle imaging (MPI).

Hyperthermia is a therapeutic treatment for cancer, wherein cancer cells are killed at temperatures above 42.5°C while normal cells remain undamaged[1]. Magnetic hyperthermia is a proposed treatment that uses self-heating from a magnetic material that is autonomously heated by its hysteresis and/or relaxation loss under an applied AC magnetic field[2-5]. MNPs are promising for use in hyperthermia, as they are easily delivered into the human body through blood vessels. After coating or conjugating biofunctional materials, MNPs can be selectively delivered to specific tumors or cells.

MNPs collected at the tumor or cancer cells can be used as "marker" in MPI[6-8]. The magnetization change of the MNPs under an applied AC magnetic field is detected by a receiver coil located outside the human body. The dynamic magnetization process essentially determines the sensitivity and spatial resolution of imaging[9-10].

Corresponding author:
Yasushi Takemura (e-mail: takemura@ynu.ac.jp).

2. Magnetic nanoparticles for biomedical applications

Iron oxide nanoparticles are widely used in biomedical applications as they are biocompatible and less toxic[11]. They are clinically used as contrast agents in magnetic resonance imaging (MRI). Particles exhibiting remanent magnetization and coercive force agglomerate after applying the magnetic field, causing occlusion of blood vessels. Therefore, superparamagnetic nanoparticles of Fe_3O_4 and γ-Fe_2O_3[12-16] are used as contrast agents in MRI and for clinical testing of hyperthermia[17].

3. Dynamic magnetization in magnetic nanoparticles

3.1 Brownian and Néel relaxations

MNPs with relatively small diameters, which typically exhibit superparamagnetic properties, are conventionally used in biomagnetic applications. In this section, we discuss the magnetization relaxation of MNPs with a single-domain structure. MNPs dispersed in solution are widely used owing to their chemical synthesis and delivery through an injection needle and catheter into the human body. These particles are subject to Brownian motion. The magnetic moment of each particle is randomly oriented by the thermal energy under an externally applied magnetic field, H_{ex}=0. The magnetic moment aligned in the direction of H_{ex}>0 is relaxed to a random orientation when H_{ex} is turned to be 0. The time constant of this relaxation, the Brownian relaxation time, τ_B, is given as[18]

$$\tau_B = \frac{3\eta V_H}{k_B T}, \qquad (1)$$

where η, V_H, k_B, and T are the dynamic viscosity of the fluid, hydrodynamic volume, Boltzmann's constant, and absolute temperature, respectively. There are several definitions of the diameter of MNPs. The primary and secondary diameters are the diameters of a single-core particle and the aggregated primary particles whose behavior in solution is characterized by the

hydrodynamic diameter, respectively. τ_B is determined from the secondary diameter. τ_B is sufficiently long compared to the observation time in the measurement when the particles are dispersed in a high-viscosity solution or when the hydrodynamic diameter is large. Particles with a small diameter in a low-viscosity solution exhibit superparamagnetic features owing to a short τ_B.

Superparamagnetic nanoparticles under an applied DC or AC magnetic field with a frequency $f << 1/(2\pi\tau_B)$ exhibit magnetization hysteresis curves with no area, considering that the magnetic moment associated with the magnetic easy axis of the nanoparticles follows the change in the applied magnetic field owing to particle rotation. In the case of $f > 1/(2\pi\tau_B)$, the particle rotation is delayed against the change in the field direction.

The Néel relaxation denotes the rotation of the magnetic moment of the nanoparticles. This relaxation is allowed even when the nanoparticles are physically fixed. The Néel relaxation time can be described as

$$\tau_N = \tau_0 \exp\left(\frac{K_u V_M}{k_B T}\right), \quad (2)$$

where K_u, V_M, and τ_0 are the magnetic anisotropy constant, the volume of the primary particle, and the attempt time, respectively. The details of these relaxations are introduced in references[18-20].

3.2 Effective relaxation time

The magnetization of MNPs dispersed in a liquid is aligned in the direction of the applied magnetic field and accompanied by both Brownian relaxation and Néel relaxation. The effective relaxation time τ_{eff} has been widely discussed using the following equation[18].

$$\tau_{eff} = 1/(1/\tau_B + 1/\tau_N) \quad (3)$$

Figure 1 shows an example of the calculated relaxation times depending on the core diameter d_{core} of the nanoparticle[21]. A particle monodispersed in water (η = 1.0×10^{-3} N・s/m^2) with a 15 nm thick coating layer was assumed in this calculation. When d_{core} < 15 nm, $\tau_N < \tau_B$. The effective relaxation time is useful for understanding the relaxation process and estimating the self-heating power of MNPs, as discussed in Section 4.3.

4. Measurement of dynamic magnetization in magnetic nanoparticles

4.1 Linear/nonlinear responses in dynamic magnetization

The dynamic magnetization process of MNPs can be measured using a detection coil[22-24]. Figures 2(a) and 2(c) show the waveforms of the applied AC magnetic field $H(t)$ and the magnetization of the MNPs $M(t)$, typically observed from superparamagnetic nanoparticles. If the magnetization rotation cannot follow the change in the applied AC magnetic field, $M(t)$ delays against $H(t)$, thereby exhibiting a phase delay, as shown in Figs. 2(b) and 2(d). Here, Figs. 2(a)/2(b) and 2(c)/2(d) correspond to the magnetization processes in the linear and nonlinear responses of the MNPs, respectively.

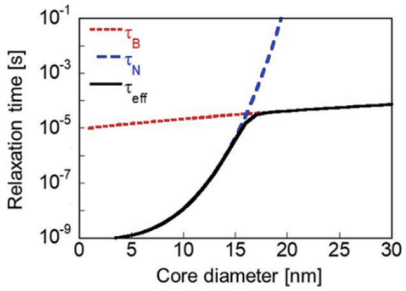

Fig. 1 Calculated Brownian, Néel, and effective relaxation times of magnetic nanoparticles depending on their core diameter, d_{core}[21]. Spherical nanoparticles coated with 15–nm layer are dispersed in water (η = 1.0×10^{-3} Ns/m^2). Anisotropy constant, K_u = 20 kJ/m^3, is used.

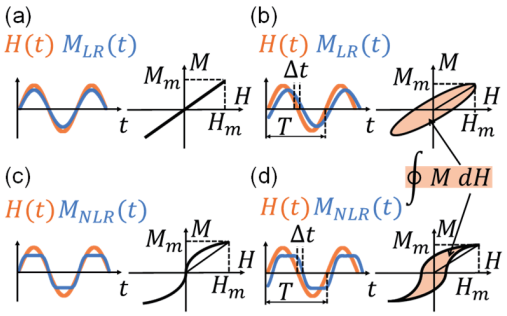

Fig. 2 Waveforms of applied magnetic field $H(t)$, magnetization of MNPs $M(t)$, and magnetization curves $M(t)$-$H(t)$ for linear response (a) without phase difference and (b) with phase difference, and nonlinear response (c) without phase difference and (d) with phase difference[25].

Figure 3 shows the DC and AC magnetization curves of the MNPs in the liquid and solid states[25]. A magnetic field of up to 0.4, 4, and 16 kA/m of DC or AC at 1–100 kHz was applied. The material used in this measurement was a water-based colloidal solution of γ-Fe_2O_3/Fe_3O_4 coated with carboxydextran supplied by Meito Sangyo Co., Ltd. The core diameter and hydrodynamic diameter were 21.6 nm and 35.8 nm, respectively. The MNPs were prepared by magnetic separation of Ferucarbotran, which is a source material for Resovist. Resovist is a contrast agent used clinically for magnetic resonance imaging. Details of the samples and measurements have been previously reported[26-28].

The liquid samples exhibited greater magnetization than the solid samples owing to the magnetization rotation of Brownian relaxation along with Néel relaxation[25,26]. The remanent magnetization and coercive force were almost zero for the DC magnetization curves of both the liquid and solid samples, which demonstrated the superparamagnetic nature of the samples. The area of the AC magnetization curves

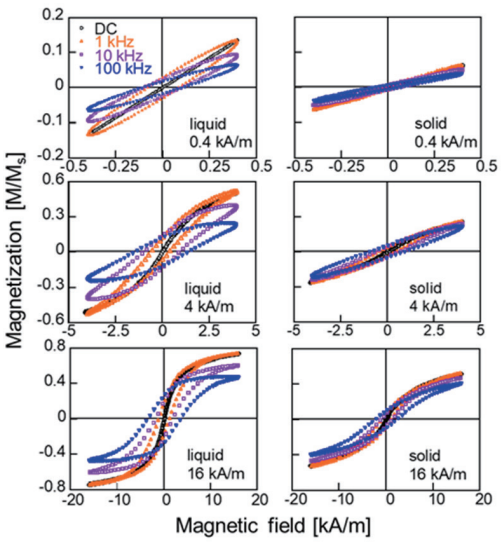

Fig. 3 DC and AC magnetization curves for liquid and solid samples of γ-Fe_2O_3/Fe_3O_4 nanoparticles. Magnetic fields of up to 0.4, 4, and 16 kA/m in DC or AC at 1–100 kHz are applied[25].

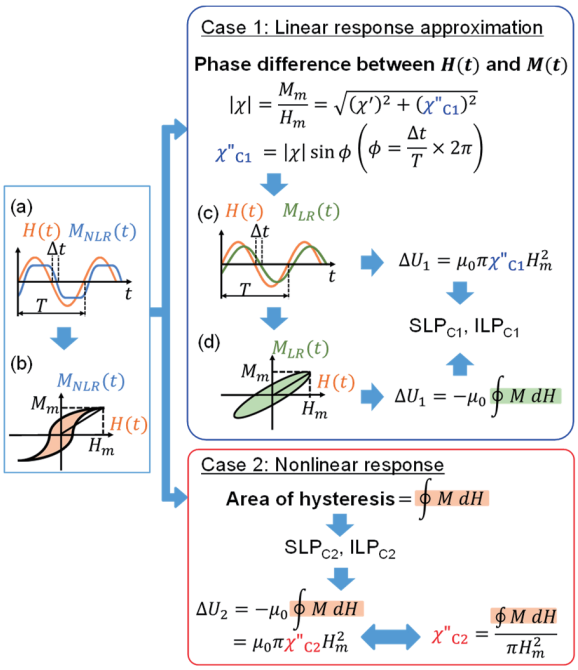

Fig. 4. Imaginary part of AC susceptibility χ'', specific loss power (SLP), and intrinsic loss power (ILP) of magnetic nanoparticles under nonlinear response to applied AC magnetic field. (a) Waveforms of applied magnetic field $H(t)$ and magnetization $M(t)$, (b) AC hysteresis derived from $H(t)$ and $M(t)$, (c) magnetization assuming linear response $M_{LR}(t)$, and (d) magnetization curve[25].

increased as the field frequency increased. Similarly, the magnetization values in the AC magnetization curves decreased as the field frequency increased. These frequency dependences can be attributed to the delay in the magnetization rotation against the change in the applied magnetic field[26]. Additionally, we reported measurements of AC magnetization under a DC bias magnetic field, which clarified the dynamics of aligned magnetization[10].

4.2 Calculation of specific loss power

In magnetic hyperthermia, the specific loss power (SLP) or specific absorption rate is an essential parameter, which is determined by measuring the self-heating temperature of the MNPs under an applied AC magnetic field. Wildeboer *et al.* suggested the instability of this measurement method owing to the temperature distribution in the samples and other factors[29].

We proposed quantifying the SLP of MNPs by measuring the AC hysteresis curves[30,31]. As discussed in the previous section, even a superparamagnetic magnetic nanoparticle with no area in the static hysteresis curve exhibits an area in the AC hysteresis curve, which is equivalent to the magnetization relaxation loss. Figure 4 summarizes the calculation of SLP and intrinsic loss power (ILP) as well as the AC susceptibility of MNPs under nonlinear response to the applied AC magnetic field. SLP was calculated using the imaginary part of the AC susceptibility based on linear response approximation, as indicated in Case 1 in Fig. 4. The SLP of the MNP under a nonlinear response was calculated using the area of the AC hysteresis curve (Case 2 in Fig. 4).

The advantage of the measurement of AC hysteresis curves is that we can quantify the SLPs of liquid, solid, power, intracellular, and possibly other states of the MNP samples. Conventional temperature measurement using a sensor probe is not suitable for some of these samples, especially for solid and intracellular MNP samples[31]. Figure 5 shows the microscopic images of the detached HeLa cells, which were collected and used as intracellular samples. Figure 6 shows the SLPs of the liquid, solid (fixed), and intracellular MNP samples. The liquid sample exhibited the highest SLP owing to higher magnetization caused by Brownian relaxation. The MNPs in the intracellular sample locally aggregated in the cells, which increased the dipole interaction of the MNPs and reduced the magnetization rotation of the Néel relaxation in the intracellular sample, resulting in a smaller SLP than that of the solid sample.

Furthermore, we measured the AC hysteresis curves of the MNPs with their oriented easy axes. The SLP of these MNPs was greater than that of MNPs with non-oriented easy axes[26].

4.3 Two-step relaxation process

The power dissipation by magnetization relaxation of the MNPs can also be derived as[18]

$$P = \pi\mu_0\chi_0 H_{ex}^2 f \frac{2\pi f\tau_{eff}}{1+(2\pi f\tau_{eff})^2}, \qquad (4)$$

where μ_0 and χ_0 are the permeability of vacuum and static

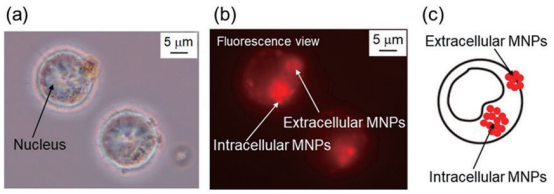

Fig. 5 Detached HeLa cells used for intracellular sample. (a) Phase contrast, (b) fluorescence view of microscopic images, and (c) illustration of intracellular and extracellular MNPs[31].

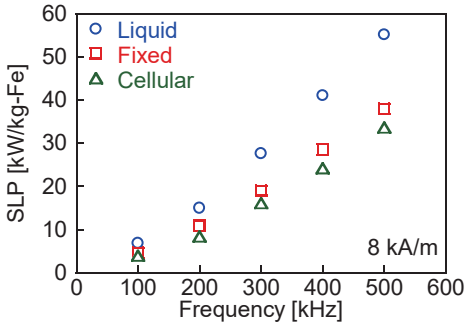

Fig. 6 Frequency dependence of specific loss powers of liquid, solid (fixed), and intracellular MNP samples[31].

susceptibility, respectively. As discussed in Section 3.2, the effective relaxation time τ_{eff}, shown in Eq. (3) is useful for estimating the self-heating power of the MNPs. Eq. (4) shows that the SLP of the MNP is dominantly dependent on the faster relaxation process of the Brownian and Néel relaxations.

MNPs with core diameters less than 10 nm exhibited relaxation times $\tau_N < \tau_B$. τ_{eff} essentially equals τ_N, and the power dissipation is dominantly determined by Néel relaxation, thereby indicating that the SLPs of the liquid and solid samples are equivalent. Nevertheless, we found that the SLP of the liquid sample was greater than that of the solid sample, which agrees with the difference in the AC hysteresis curves of the liquid and solid samples, as shown in Fig. 3[25,32]. These experimental results cannot be explained by the effective relaxation time τ_{eff} and further measurements of pulse excitation have been initiated.

Figure 7 shows the calculated responses of the magnetization and easy axis of MNPs[33]. The core and hydrodynamic diameters of d_c= 10 nm and d_h = 40 nm, and anisotropy constant of K_u =10 kJ/m^3 are summed, respectively. The upper figure shows the waveform of the applied pulsed magnetic field $H(t)$, which simulates the actual pulse signal of our experimental setup. The magnetization $M(t)$ shown in the lower figure corresponds to $H(t)$ without a time delay, as τ_N is sufficiently small. This magnetization response from 10^{-7} to 10^{-5} s is responsible for Néel relaxation. The lower figure also shows the response of the particles, indicated by the average angles of the easy axes. This particle response of Brownian relaxation starts at 10^{-5} s and relaxes at 10^{-3} s.

Two-step relaxation was clearly observed in our measurements, as shown in Fig. 8 [33]. The measured $M(t)$ exhibited Néel relaxation followed by Brownian relaxation. The waveforms of both relaxations agree with their relaxation times, depending on the diameter described by Eqs. (1) and (2), respectively. The details of the calculations and experiments are reported in Refs. 33 and 34. Recently, Bui *et al.* reported an analysis of magnetic susceptibility based on distinguished Brownian and Néel relaxations[35].

4.4 Dynamics of magnetization easy axis

As discussed in the previous section, we observed the temporal magnetization of the easy axis of MNPs. Furthermore, we clarified the effect of dipole interactions in multi-core MNPs on the magnetization response by pulse excitation.

The time evolution of the magnetic moment and easy axis in an individual magnetic nanoparticle dispersed in

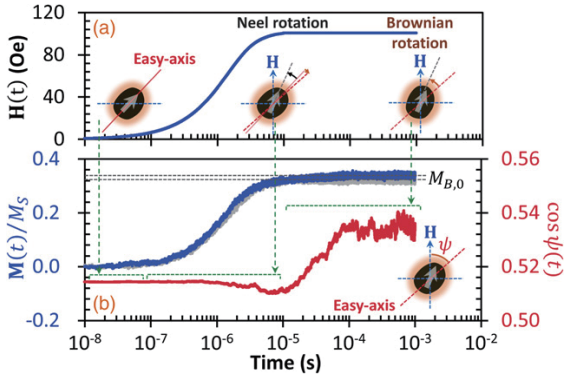

Fig. 7 Calculated magnetization response of magnetic nanoparticles. (a) Waveform of applied 100-Oe pulsed magnetic field $H(t)$ close to experimental conditions and (b) average responses of temporal magnetization $M(t)$ and field-relative easy-axis angle $\psi(t)$[33].

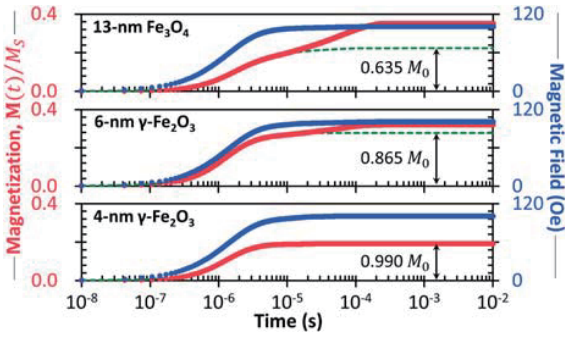

Fig. 8 Temporal magnetization responses of liquid samples of γ-Fe_2O_3 nanoparticles with different core diameters (13, 6, and 4 nm)[33].

a fluid was numerically simulated by the Landau-Lifshiz-Gilbert (LLG) equation[36,37] as

$$\frac{d\boldsymbol{m}}{dt} = \boldsymbol{\omega} \times \boldsymbol{m} - \frac{\gamma}{1+\alpha^2}\left[\boldsymbol{m} \times \left(\boldsymbol{H}_{\mathrm{eff}} - \frac{\boldsymbol{\omega}}{\gamma}\right) + \alpha \boldsymbol{m} \times \left\{\boldsymbol{m} \times \left(\boldsymbol{H}_{\mathrm{eff}} - \frac{\boldsymbol{\omega}}{\gamma}\right)\right\}\right], \quad (5)$$

where α is the damping parameter (α = 0.1) and γ is estimated as $\gamma = \mu_0 M_s V_M(1+\alpha^2)/(2\alpha\tau_N k_B T)$. $\boldsymbol{m}$ is the magnetic moment normalized by the saturation magnetic moment, M_s. $\boldsymbol{H}_{\mathrm{eff}}$ is an effective field comprising excitation field, an anisotropy field, and thermally fluctuating field. The anisotropy field was estimated as $\boldsymbol{H}_{\mathrm{an}} = 2K_u(\boldsymbol{m}\cdot\boldsymbol{n})\boldsymbol{n}/(\mu_0 M_s)$. The orientation of the easy axis is calculated using the unit vector and angular velocity of the easy axis, $\boldsymbol{n}$ and $\boldsymbol{\omega}$, respectively, given as: $d\boldsymbol{n}/dt = \boldsymbol{\omega} \times \boldsymbol{n}$. The random torque due to thermal disturbance is considered in $\boldsymbol{\omega}$.

The angle between the magnetization and easy axis ψ was evaluated for individual particles depending on the anisotropy energy[27]. ψ was calculated from the vector product of the unit vector of the magnetization and easy axis, $|\boldsymbol{m} \times \boldsymbol{n}|$. The original symmetry can be applied to the easy axis. The averaged value of ψ in Fig. 9 indicates that ψ decreased with large anisotropy energy as both K_u and the core diameter d_c increased. The anisotropy energy binds the magnetization to the rotatable easy axis. The increase in ψ owing to the effect of thermal fluctuation illustrates the superparamagnetic regime.

The effects of orientation and oscillation on the easy axis were empirically evaluated under an AC magnetic field. The AC magnetization curves of the solid sample subtracted from those of the liquid sample were evaluated[38]. Moreover, we prepared the mixture containing MNPs and epoxy resin cured under AC magnetic fields with frequencies between 0.2–100 kHz at an intensity of 8 kA/m[39]. This approach was used to ensure that the easy axis had a fixed orientation when measurements were conducted in the AC magnetic field, thereby indicating that the coercivities of the AC magnetization curves in the liquid sample increased for a long τ_B compared to the applied field frequency, considering the easy axis orientation toward the direction

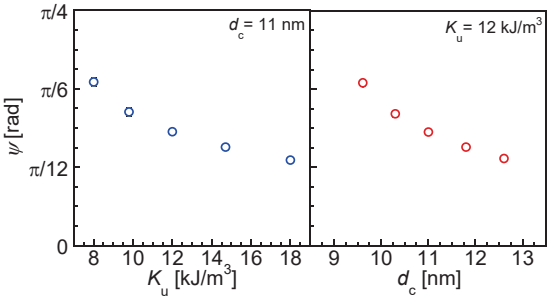

Fig. 9 Angle between magnetization and easy axis ψ depending on anisotropy energy determined by values of K_u and d_c. Easy axis is rotatable. ψ is calculated using expression $|\mathbf{m} \times \mathbf{n}|$. Statistical analysis is conducted in one cycle of applied field with a time interval of 100 ns (N= 100)[27].

of the applied magnetic field effectively increased the anisotropy energy. Conversely, the orientation of the easy axis decreased significantly for a long τ_N compared to the applied field frequency owing to the small magnetic torque caused by small magnetization.

5. Summary

The dynamic magnetization process of MNPs is essential for determining various properties of hyperthermia and MPI, which are major medical applications of MNPs. The measurements of the static and dynamic magnetization curves of MNP samples, including liquid, solid, and intracellular states, conducted in this study clarified the distinguished Brownian and Néel relaxations depending on the applied magnetic field intensity and frequency. The Brownian relaxation is accompanied by particle rotation and can be magnetically measured as the response of the magnetization easy axes of MNPs. Furthermore, we observed the dynamics of the easy axes in the measurements using both the AC and pulsed magnetic fields. These experimental results of our study are significant for understanding the magnetization dynamics of MNPs, which have not been previously considered.

Acknowledgements The experiments were performed in collaboration with our lab team coauthors in the references below. The authors wish to express their gratitude for the advice and support from Profs Keiji Enpuku and Takashi Yoshida from Kyushu University. This study was partially supported by JSPS KAKENHI JP20H05652, JP20H02163, JP22K14268, JP17K14693, JP17H03275, and JP15H05764.

References

1) R. J. Palzer and C. Heidelberger: *Cancer Res.*, **33**, 415 (1973).
2) Q. A. Pankhurst, J. Connolly, S. K. Jones, and J. Dobson: *J. Phys. D: Appl. Phys.*, **36**, R167 (2003).
3) Q. A. Pankhurst, N. K. T. Thanh, S. K. Jones, and J. Dobson: *J. Phys. D Appl. Phys.*, **42**, 224001 (2009).
4) K. M. Krishnan: *IEEE Trans. Magn.*, **46**, 2523 (2010).
5) S. Dutz and R. Hergt: *Int. J. Hyperthermia*, **29**, 790 (2013).
6) B. Gleich and J. Weizenecker: *Nature*, **435**, pp. 1214–1217 (2005).
7) D. Hensley, Z. W. Tay, R. Dhavalikar, B. Zheng, P. Goodwill, C. Rinaldi, and S. Conolly: *Phys. Med. Biol.*, **62**, 3483 (2017).
8) T. Yoshida and K. Enpuku: *Jpn. J. Appl. Phys.*, **48**, 127002 (2013).
9) A. Tomitaka, R. M. Ferguson, A. P. Khandhar, S. J. Kemp, S. Ota, K. Nakamura, Y. Takemura, and K. M. Krishnan: *IEEE Trans. Magn.*, **51**, 6100504 (2015).
10) S. Ota, K. Nishimoto, T. Yamada, and Y. Takemura: *AIP Adv.*, **10**, 015007 (2020).
11) A. Tomitaka, A. Hirukawa, T. Yamada, S. Morishita, and Y. Takemura: *J. Magn. Magn. Mater.*, **321**, 1482 (2009).
12) R. Medal, W. Shorey, R. K. Gilchrist, W. Barker, and R. Hanselman: *Arch. Surg.*, **79**, 427 (1959).
13) A. Jordan, R. Scholz, P. Wust, H. Fähling, and R. Felix: *J. Magn. Magn. Mat.*, **201**, 413 (1999).
14) K. Okawa, M. Sekine, M. Maeda, M. Tada, M. Abe, N. Matsushita, K. Nishio, and H. Handa: *J. Appl. Phys.*, **99**, 08H102 (2006).

15) T. Atsumi, B. Jeyadevan, Y. Sato, and K. Tohji: *J. Magn. Magn. Mater.*, **310**, 2841 (2007).
16) A. Ito and T. Kobayashi: *Thermal Med.*, **24**, 113 (2008).
17) K. Maier-Hauff, R. Rothe, R. Scholz, U. Gneveckow, P. Wust, B. Thiesen, A. Feussner, A. von Deimling, N. Waldoefner, R. Felix, and A. Jordan: *J Neurooncol.*, **81**, 53 (2007).
18) R. E. Rosensweig: *J. Magn. Magn. Mat.*, **252**, 370 (2002).
19) B. Mehdaoui, J. Carrey, A. Cornejo, C. Nayral, F. Delpech, B. Chaudret, and M. Respaud: *Appl. Phys. Lett.*, **100**, 05403 (2012).
20) H. Mamiya and B. Jeyadevan: *Sci. Rep.*, **1**, 157 (2011).
21) R. Kötitz, W. Weitschies, L. Trahms, W. Brewer, and W. Semmler: *J. Magn. Magn. Mat.*, **194**, 62 (1999).
22) H. Kobayashi, A. Hirukawa, A. Tomitaka, T. Yamada, M. Jeun, S. Bae, and Y. Takemura: *J. Appl. Phys.*, **107**, 09B322 (2010).
23) H. Kobayashi, K. Ueda, A. Tomitaka, T. Yamada, and Y. Takemura: *IEEE Trans. Magn.*, **47**, 4151 (2011).
24) J. Kim, D. Heo, J. Wang, H. Kim, S. Ota, Y. Takemura, C. Huh, and S. Bae: *Nanoscale*, **13**, 19484 (2021).
25) T. Yamaminami, S. Ota, S. B. Trisnanto, M. Ishikawa, T. Yamada, T. Yoshida, K. Enpuku, and Y. Takemura: *J. Magn. Magn. Mater.*, **517**, 167401 (2021).
26) G. Shi, R. Takeda, S. B. Trisnanto, T. Yamada, S. Ota, and Y. Takemura: *J. Magn. Magn. Mat.*, **473**, 148 (2019).
27) S. Ota and Y. Takemura: *J. Mag. Soc. Jpn.*, **43**, 34 (2019).
28) S. Ota, Y. Matsugi, T. Nakamura, R. Takeda, Y. Takemura, I. Kato, S. Nohara, T. Sasayama, T. Yoshida, and K. Enpuku: *J. Magn. Magn. Mat.*, **474**, 311 (2019).
29) R. R. Wildeboer, P. Southern, and Q. A. Pankhurst: *J. Phys. D: Appl. Phys.*, 47, 495003 (2014).
30) S. Ota, S. B. Trisnanto, S. Takeuchi, J. Wu, Y. Cheng, and Y. Takemura: *J. Magn. Magn. Mater.*, **538**, 168313 (2021).
31) S. Ota, T. Yamada, and Y. Takemura: *J. Nanomater.*, **2015**, 836761 (2015).
32) S. Ota, T. Yamada, and Y. Takemura: *J. Appl. Phys.*, **117**, 17D713 (2015).
33) S. B. Trisnanto, S. Ota, and Y. Takemura: *Appl. Phys. Express.*, **11,** 075001 (2018).
34) S. Ota and Y. Takemura: *J. Appl. Chem. C*, **123**, 28859 (2019).
35) T. Q. Bui, A. J. Biacchi, C. L. Dennis, W. L. Tew, A. R. H. Walker, and S. I. Woods: *Appl. Phys. Lett.*, **120**, 012407 (2022).
36) W. T. Coffey and Y. P. Kalmykov: *J. Magn. Magn. Mater.*, **164**, 133 (1996).
37) T. Yoshida, S. Bai, A. Hirokawa, K. Tanabe, and K. Enpuku: *J. Magn. Magn. Mater.*, **380**, 105 (2015).
38) S. Ota and Y. Takemura: *Appl. Phys. Express.*, **10**, 085001 (2017).
39) S. Ota, S. Ohkawara, H. Hirano, M. Futagawa, and Y. Takemura: *J. Magn. Magn. Mat.*, **539**, 168354 (2021).

Received Feb. 23, 2023; Accepted Mar. 19, 2023.

J. Magn. Soc. Jpn., **47**, 90-102 (2023)

<Review>

First-principles Studies on Spin-dependent Transport of Magnetic Junctions with Half-metallic Heusler Compounds

Y. Miura[*,**]

[*]Research Center for Magnetic and Spintronic Materials (CMSM), National Institute for Materials Science (NIMS), *1-2-1 Sengen, Tsukuba, Ibaraki 305-0032, Japan*

[**]Center for Spintronics Research Network (CSRN), Graduate School of Engineering Science, Osaka University, *Machikaneyama 1-3, Toyonaka, Osaka 560-8531, Japan*

Two types of magnetoresistance (MR), i.e., tunnel magnetoresistance (TMR) and current perpendicular to plane giant magnetoresistance (CPP-GMR), are theoretically discussed for systems with half-metallic (HFM) Co-based full Heusler compounds. In TMR, the non-collinear spin structure at the Co_2MnSi(CMS)/MgO(001) interface that results from thermal spin fluctuations significantly reduced the TMR ratio at room temperature (RT). Enhancement of the exchange stiffness of CMS/MgO was essential to suppress the reduction in TMR at RT. Furthermore, it is proposed that inserting of a B2-CoFe layer between CMS and MgO is a promising way to enhance the interface exchange stiffness constant. In CPP-GMR, the interface spin asymmetry γ in the Valet-Fert model was essential to enhance GMR at RT, because the temperature dependence of γ in experiments was much larger than that of the bulk spin asymmetry ß. I showed that the experimental CPP-GMR ratio increases with the decrease in the theoretical resistance-area product R_PA, which is roughly consistent with the R_P dependence of γ. This means that matching of the conductive channel between HMF and a non-magnetic metallic spacer is a key parameter to enhance γ. These findings will be very important for room temperature spintronics devices applied in future artificial intelligence hardware.

Key words: magnetoresistance, first-principles calculation, Heusler compound, TMR, CPP-GMR, ballistic transport, exchange stiffness

1. Introduction

I introduce "Theoretical Study on Spin-dependent Transport Properties in Magnetic Junctions" in this review paper, which was a research subject of MSJ Outstanding Research Award 2022.

The spin-dependent tunneling between two ferromagnetic (FM) electrodes separated by a non-magnetic (NM) layer provides magnetoresistance (MR) that depends on the relative magnetization directions of the ferromagnetic electrodes.[1–3] The effect is applied in magnetoresistive random access memory (MRAM) and ultra-sensitive magnetoresistive sensors, which are essential to realize artificial intelligence (AI) hardware and neuromorphic devices in the next-generation information society.[4,5] There are two types of MR devices according to the type of nonmagnetic layer, which are tunneling magnetoresistance (TMR) devices with an insulating barrier layer, and current-perpendicular-to-plane giant magnetoresistance (CPP-GMR) devices with a NM metal spacer. To realize AI-dedicated and neuromorphic spintronics devices, a large MR ratio and low resistance are required.

High TMR ratios over 300% at room temperature have been realized in magnetic tunnel junctions (MTJs) with single-crystalline MgO and bcc-FeCo[6–8] from coherent tunneling through the Δ_1 evanescent state in MgO and the highly spin-polarized Δ_1 band around the Fermi level in bcc-FeCo[9,10]. This means that in TMR devices, the spin dependence of the current can be characterized by the spin polarization of the Δ_1 state of the ferromagnetic electrodes at in-plane wave vector $\mathbf{k}_\parallel = \mathbf{0}$ rather than that of the total density of states (DOSs) around the Fermi level. In MgO-based MTJs, it is difficult to reduce the resistance while maintaining high TMR. Reducing the barrier thickness of MTJs decreases the TMR as well as the resistance, because the tunneling of non-spin-polarized Δ_5 and Δ_2 states is not negligible in a MgO layer with a thickness of a few monolayers. Thus, half-metallic ferromagnets (HMFs), which are metallic for the majority-spin band and insulating for the minority-spin band with complete (100%) spin polarization at the Fermi level, will be important to realize both high TMR and low resistance for MTJs with few-monolayer MgO thickness.

CPP-GMR devices composed of all-metallic layers have lower resistance than TMR devices, but their MR ratios are also typically more than an order of magnitude smaller. This is due to the presence of many scattering processes in all-metallic systems, because in a metallic system, not only electrons with $\mathbf{k}_\parallel = \mathbf{0}$ but also those with $\mathbf{k}_\parallel \neq \mathbf{0}$ contribute equally to the current. Thus, the spin-dependent transport in GMR devices can be characterized by the spin polarization of the total DOSs of the ferromagnetic electrodes rather than the spin polarization at the specific $\mathbf{k}_\parallel$, and HMFs again are

Corresponding author: Y. Miura
(e-mail: MIURA.Yoshio@nims.go.jp)

Table 1 Summary of experimental results on TMR ratio [%] at room temperature (RT) and low temperature (LT) for MTJs with Co-based full Heusler compounds Co_2YZ (exact temperatures differ between studies).

Bottom electrode	Barrier	Upper electrode	TMR % @ LT	TMR % @ RT	Year [Reference]
$Co_2(Cr_{0.6}Fe_{0.4})Al$	Al-O	$Co_2(Cr_{0.6}Fe_{0.4})Al$	26.5	16	2003[26]
Co_2MnAl	Al-O	$Co_{0.5}Fe_{0.5}$	40	27	2004[27]
Co_2FeAl	Al-O	$Co_{0.75}Fe_{0.25}$		47.3	2005[28]
Co_2MnSi	Al-O	Co_2MnSi	570	67	2006[29]
$Co_2Fe(Al_{0.5}Si_{0.5})$	Al-O	$Co_{0.75}Fe_{0.25}$	106	76	2006[30]
$Co_2(Cr_{0.6}Fe_{0.4})Al$	MgO	$Co_{0.5}Fe_{0.5}$	240	90	2007[31]
Co_2MnSi	MgO	$Co_{0.5}Fe_{0.5}$	753	217	2008[32]
Co_2MnSi	MgO	Co_2MnSi	700	180	2009[33]
$Co_2Fe(Al_{0.5}Si_{0.5})$	MgO	$Co_2Fe(Al_{0.5}Si_{0.5})$	832	386	2009[34]
Co_2FeAl	MgO	Co_2FeAl	308	130	2009[35]
Co_2FeAl	MgO	CoFe	700	330	2010[36]
$Co_2Mn_{1.29}Si$	MgO	$Co_2Mn_{1.29}Si$	1995	354	2012[37]
$Co_2(Fe_{0.5}Mn_{0.5})Si$	MgO	$Co_2(Fe_{0.5}Mn_{0.5})Si$	2610	429	2015[38]
Co_2FeAl	$MgAl_2O_4$	$Co_2Fe(Al_{0.5}Si_{0.5})$	616	342	2016[39]
$Co_2Mn_{1.3}Si_{0.84}$	MgO	$Co_2Mn_{1.3}Si_{0.84}$	2010	335	2016[40]
$Co_2Fe(Ga_{0.5}Ge_{0.5})$	$Cu(In_{0.8}Ga_{0.2})Se_2$	$Co_2Fe(Ga_{0.5}Ge_{0.5})$	100	40	2016[41]
$Co_2Fe(G_{a0.5}Ge_{0.5})$	$CuGaSe_2$	$Co_2FeGa_{(0.5}Ge_{0.5})$	250	100	2019[42]

important for obtaining large GMR.

Among the many theoretically predicted HMFs,[11–16] the Co-based full Heusler compounds Co_2YZ (Y = Cr, Mn, Fe, Z = Al, Si, Ga, Ge) are the most promising candidates for use in spintronics devices because of their high Curie temperatures above room temperature (RT). A characteristic feature of Co-based full Heusler compounds is that their electronic structure hardly changes with respect to the specific atomic disorder, such as B2-type disorder, where Y and Z atom sites are randomly occupied.[17–19] The robustness of high spin polarization against the atomic disorder of Co-based Heusler compounds is important in terms of the relaxation of experimental requirements, because it is expected that some degree of atomic disorder will occur during thin-film fabrication. The valence-band electronic structures of typical halfmetallic Co-based full Heusler compounds Co_2MnSi (CMS) were investigated by photoelectron spectroscopy to confirm the temperature dependence of the electronic structures.[20] The experimental valence band photoemission spectra at 30 K were in good agreement with density functional theory (DFT) calculations at zero temperature, and no distinct temperature dependence was observed in the experimental valence band spectra. Furthermore, the temperature dependence of the spin-polarization of CMS was shown to be small by spin-resolved hard x-ray photoelectron spectroscopy.[21] Recently, we calculated the temperature dependence of the bulk electronic structures of half-metallic Co-based Heusler compounds using the disordered local moment (DLM) method,[22] and found that the temperature dependence of the spin-polarization of the *sp* density of states (DOS) of $Co_2FeGa_{0.5}Ge_{0.5}$ (CFGG) is weaker than that of CMS.[23,24] Furthermore, several new Co-based Heusler compounds such as $Co_2MnGa_{1-x}As_x$ and $Co_2FeAl_{1-x}Sn_x$ were proposed by the machine learning method with finite temperature first-principles calculations using the DLM.[25]

Table 1 summarizes experimental studies on TMR ratios at low temperature (LT) and RT for Co-based full Heusler MTJs[26-42]. Half-metallic Co_2YZ compounds have been applied in TMR devices with an amorphous alumina barrier[26–30] and then in MTJs with a MgO barrier, and large TMR ratios were demonstrated.[31–38,40] Furthermore, new barrier materials such as $MgAl_2O_4$[39] and $Cu(In_{1-x}Ga_x)Se_2$[41,42] have been applied as the barrier layer in Heusler-based MTJs. Particularly, MTJs with Mn-rich CMS and $Co_2(Mn,Fe)_aSi$ with MgO barriers provided huge TMR exceeding 2000% at very low temperature,[38,40] indicating the potential of the halfmetallic electronic structures. However, the TMR also rapidly decreases with increasing temperature.

As is shown in Table 1, experiments on the TMR effect of MTJs with half-metallic Co-based full Heusler compounds have not been reported after 2019. There are two reasons for the decrease in experimental studies on TMR in Heusler-based MTJs. One is the large temperature dependence of the TMR ratios of MTJs with half-metallic Co-based full Heusler compounds.

Table 2 Summary of experimental results on GMR ratio % and ΔRA mΩ · μm² at room temperature (RT) and low temperature (LT) for CPP-GMR devices with Co_2YZ (exact temperatures differ between studies).

System	GMR % @ LT (ΔRA mΩ · μm²)	GMR % @ RT (ΔRA mΩ · μm²)	Year [Reference]
$Co_2MnSi/Cr/Co_2MnSi(001)$		2.4 (19)	2006[49]
$Co_2MnSi/Cu/Co_2MnSi(001)$		9	2008[50]
$Co_2Fe(Al_{0.5}Si_{0.5})/Ag/Co_2Fe(Al_{0.5}Si_{0.5})(001)$	14 (12.4)	6.9 (7.4)	2008[51]
$Co_2MnSi/Cr/Co_2MnSi(001)$		5.2 (6.5)	2009[52]
$Co_2MnSi/Ag/Co_2MnSi(001)$		28.8 (8.92)	2009[53]
$Co_2Fe(Al_{0.5}Si_{0.5})/Ag/Co_2Fe(Al_{0.5}Si_{0.5})(001)$	80 (17)	34 (8)	2010[54]
$Co_2Mn(Ga_{0.5}Sn_{0.5})/Ag/Co_2Mn(Ga_{0.5}Sn_{0.5})(001)$	17.2 (6.5)	8.8 (4)	2010[55]
$Co_2MnSi/Ag/Co_2MnSi(001)$	67.2	36.4 (11.5)	2010[56]
$Co_2Fe(Ga_{0.5}Ge_{0.5})/Ag/Co_2Fe(Ga_{0.5}Ge_{0.5})(001)$	129.1 (26.4)	41.7 (9.5)	2011[57]
$Co_2MnGe/Cu/Co_2MnGe(001)$		9 (6)	2011[58]
$Co_2(Fe_{0.4}Mn_{0.6})Si/Ag/Co_2(Fe_{0.4}Mn_{0.6})Si(001)$		74.8	2011[59]
$Co_2(Fe_{0.4}Mn_{0.6})Si/Ag/Co_2(Fe_{0.4}Mn_{0.6})Si(001)$	184	58 (11)	2012[60]
$Co_2Fe(Ga_{0.5}Ge_{0.5})/Ag/Co_2Fe(Ga_{0.5}Ge_{0.5})(001)$	183 (33)	57 (12)	2013[61]
$Co_2Fe(Ga_{0.5}Ge_{0.5})/NiAl/Ag/NiAl/Co_2Fe(Ga_{0.5}Ge_{0.5})(001)$	285 (78)	82 (31)	2016[62]
$Co_2Mn_{1.45}Si_{0.82}/CoFe/Ag/CoFe/Co_2Mn_{1.45}Si_{0.82}(001)$		20.7 (3.1)	2017[63]
$Co_2(Fe_{0.4}Mn_{0.6})Si/Ag_3Mg/Co_2(Fe_{0.4}Mn_{0.6})Si(001)$		63 (25)	2017[64]
$Co_2(Fe_{0.4}Mn_{0.6})Ge/AgSn/Co_2(Fe_{0.4}Mn_{0.6})Ge(001)$		25 (7.5)	2018[65]
$Co_2(Fe_{0.4}Mn_{0.6})Si/Ag_3Mg/Co_2(Fe_{0.4}Mn_{0.6})Si(001)$	100	30	2019[66]
$Co_2Fe(Ga_{0.5}Ge_{0.5})/Ni/Ag/Ni/Co_2Fe(Ga_{0.5}Ge_{0.5})(001)$		32.5	2021[67]
$CoFe/Co_2(Fe_{0.4}Mn_{0.6})Si/Ag/Co_2(Fe_{0.4}Mn_{0.6})Si/CoFe(001)$		50 (19.1)	2021[68]

The TMR ratio of Heusler-based MTJs at RT is still smaller than that of CoFe-based MTJs. Recently, a breakthrough in the RT TMR of CoFe-based MTJs was achieved by Scheike *et al.*, where a 631% TMR ratio at RT and 1143% TMR ratio at LT were observed for CoFe/MgO/CoFe(001) MTJs.[43] To demonstrate the potential of half-metallic Heusler compounds, it is important to achieve a larger TMR ratio at RT than that of CoFe-based MTJs. The other reason for the decrease in studies is requirement of MTJs with the perpendicular magnetic anisotropy (PMA). In spin-transfer torque switching of the magnetization direction in MTJs, PMA is required in order to reduce the effective anisotropy field of MTJs. Since the Co-based full Heusler compounds show basically cubic symmetry, the magneto-crystalline anisotropy (MCA) of Co_2YZ is zero. Thus, the magnetic anisotropy of Co_2YZ(001) thin films tends to have an in-plane easy axis due to the shape anisotropy. Some Mn-based Heusler compounds such as Mn_3Ga and Mn_3Ge with $D0_{22}$ structure have tetragonal structures, showing perpendicular MCA in the bulk.[44–47] However, the experimental results for the TMR effects of Mn_3Ga/MgO- and Mn_3Ge/MgO-based MTJs[44,48] are very small compared with those of Co_2YZ/MgO-based MTJs because of the large lattice mismatch of Mn_3Ga and Mn_3Ge with MgO[47] and the non-half-metallic behavior of the Δ_1 states of Mn_3Ga.[44] Therefore, achieving perpendicular MCA in Heusler-based MTJs will be also a future task.

Table 2 summarizes experimental studies on GMR ratios and the difference in resistance-area product between parallel and antiparallel magnetizations ΔRA at LT and RT for various CPP-GMR systems with Co-based full Heusler compounds.[49-68] Half-metallic Co_2YZ have also been applied in CPP-GMR devices, and relatively large GMR ratios have been observed for Heusler-based magnetic junctions with a Cr spacer,[49,52] Cu spacer,[50,58] Ag spacer,[51,53–57,59–61] Ag_3Mg spacer[64,66] and AgSn spacer.[65] Furthermore, insertions of an additional layer were attempted to enhance the matching of conductive channels between Co-based full Heusler compounds and NM spacers, such as NiAl insertion in the CFGG/Ag(001) interface,[62] Ni insertion in the CFGG/Ag(001) interface,[67] CoFe insertion in the CMS/Ag(001) interface[63] and $Co_2(Fe_{0.4}Mn_{0.6})Si$ insertion in the CoFe/Ag(001) interface,[68] which led to an increase in the CPP-GMR ratios.

In this review, I discuss the spin-dependent transport properties of TMR and CPP-GMR devices with half-metallic Co_2YZ based on first-principles electronic structure and ballistic transport calculations. Particularly, I focus on the spin-dependent transport of magnetic junctions with half-metallic Co_2YZ. First, I discuss the origin of the temperature dependence of the TMR ratios in MTJs. The spin-dependent conductance

of MTJs with CMS (or Fe) and MgO was investigated based on first-principles calculations in a noncollinear spin system. Noncollinear magnetic structures are formed as a result of spin fluctuation at finite temperatures. I focus on the spin-flip scattering of conducting electrons caused by the noncollinearity of local spin moments in various interfacial layers, and I discuss the electronic states at the interfaces that contribute to the spin-flip conductance. Our theoretical analysis confirmed the crucial contribution of the spin-flip process at the interface, which leads to a significant reduction in the MR ratio at RT. Then, I discuss the interface spin-asymmetry in CPP-GMR devices. I argue that the matching of the Fermi surface projected to the two-dimensional Brillouin zone in in-plane wave vector $\mathbf{k}_{\parallel}$ between the CMS and NM spacers is important to enhance the interface spin asymmetry. Furthermore, I clarify the correlation between experimental CPP-GMR ratios and the theoretical interface resistance in parallel magnetization in CPP-GMR.

2. Computational Method

I performed first-principles calculations for supercells consisting of Co-based Heusler compounds Co_2YZ (Y = Mn or Fe, Z = Si, Ga or Ge) and various non-magnetic (NM) layers X such as X = MgO, Ag, Cr, V, Al and Au using the DFT within the generalized-gradient approximation for the exchange-correlation energy.[69] In order to facilitate the optimization of atomic positions, which is important for determining the interface structure, I adopted plane-wave basis sets along with the ultra-soft pseudopotential method by using the quantum code ESPRESSO.[70] The number of k points is taken to be 15×15×1 for all cases, and Methfessel-Paxton smearing with a broadening parameter of 0.01 Ry is used. The cutoff energy for the wavefunction and charge density is set to 30 Ry and 300 Ry, respectively. These values are large enough to deal with all the elements considered here within the ultra-soft pseudopotential method. $Co_2YZ/X/Co_2YZ(001)$ magnetic junctions with Co (YZ) termination were constructed in a multilayer structure containing seventeen (fifteen) atomic layers of Co_2YZ and seven or nine atomic layers of NM. The in-plane lattice parameter of the supercell is fixed to that of Co_2YZ. These values correspond to $a_0/\sqrt{2}$, where a_0 is the lattice constant of the bulk Co_2MnSi (5.65 Å). Since the lattice constant of the NM layer X is different from that of Co_2YZ, the lattice mismatches between Co_2YZ and X on the 45° in-plane rotation at the (001) face are considered, leading to tetragonal distortion in the NM layer (X).

For transport calculations, I calculated the ballistic conductance of the magnetic junctions based on the Landauer formula.[71] I considered an open quantum system consisting of a scattering region corresponding to NM spacer X and a junction with Co_2YZ attached to left and right semi-infinite electrodes corresponding to bulk Co_2YZ. The transmittance can be obtained by solving the scattering equation with infinite boundary conditions, in which the wavefunction of the scattering region and its derivative are connected to the Bloch states of each electrode.[72] The potential in the scattering equation can be obtained from self-consistent filed electronic structure calculations for the supercell containing a left electrode and a scattering region. It was confirmed that five atomic layers of Co_2YZ between the right edge of the electrode region and the left-hand side of the Co_2YZ/X interface are sufficient to represent the shape of the local potential of bulk Co_2YZ in the electrode region.

Since our system is repeated periodically in the xy plane and propagating states can be assigned by an in-plane wave vector $\mathbf{k}_{\parallel} = (k_x, k_y)$ index, different $\mathbf{k}_{\parallel}$ do not mix and can be treated separately. Furthermore, our approach neglects the spin-orbit interaction and noncollinear spin configuration. Thus, I solved scattering equations for some fixed $\mathbf{k}_{\parallel}$ and spin index using Choi and Ihm's method.[72, 73]

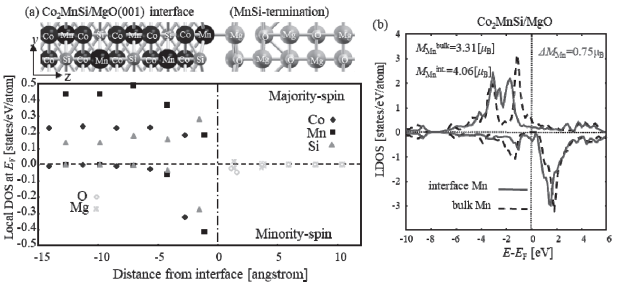

Fig. 1 Local density of states (LDOS) at Fermi level (E_F) projected onto each atomic sphere as a function of the distance from interface for Co_2MnSi(CMS) /MgO(001) with MnSi termination. Positive (negative) sign of y-axis indicates majority-spin (minority-spin) LDOS. Schematic figures of supercell of CMS/MgO/CMS(001) MTJ are shown above the LDOS. (b) The solid lines show LDOS of Mn d at MnSi-terminated CMS/MgO(001) interface as a function of energy relative to E_F. LDOS in bulk (electrode) region is also shown by dashed line as a reference. ref.[74]

3. Spin-dependent transport in TMR devices

3.1 Interface electronic structures

Figure 1(a) shows the majority- and minority-spin local density of states (LDOS) at the Fermi level projected onto each atomic sphere as a function of the distance from the Co_2MnSi(CMS)/MgO(001) junction.[74] It is found that in the case of MnSi termination, interface states appear in the minority-spin state at the Fermi level, reducing the half-metallicity of CMS. Similar results have been obtained in the Co termination of the CMS/MgO(001) junction.[75] Examining the electronic structure at the interface in

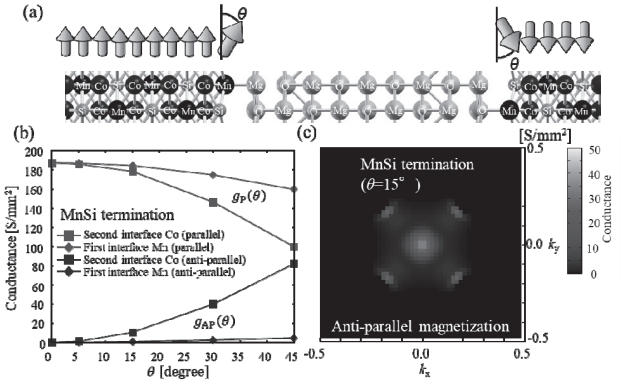

Fig. 2 (a) Schematic figure of CMS/MgO/CMS MTJs with MnSi termination and local spin moments for each layer, with a noncollinear magnetic structure on both sides of junction. (b) Parallel and antiparallel conductance of CMS/MgO/CMS MTJ as a function of the angle of interfacial local spin moments θ. (c) In-plane wave-vector (**k**∥) dependence of antiparallel conductance of CMS/MgO/CMS MTJ with θ = 15° for MgO thickness ~ 2.0 nm (nine atomic layers of MgO). ref. [81]

more detail, Fig. 1(b) presents the majority- and minority-spin LDOS of each atom and atomic orbital in the MnSi-terminated CMS/MgO(001). The LDOS in the bulk (electrode) region is also shown as a reference. In Fig. 1(b), it is found that the spin moment of the interfacial Mn (4.06 μ_B) is larger than those of the bulk CMS (3.31 μ_B) due to the charge transfer from the minority-spin to the majority-spin states. I considered that the relaxation of the atomic positions and the reduced symmetry at the interface cause charge transfer from the minority-spin to the majority-spin 3*d* states owing to the localization effect of 3*d* electrons.

Furthermore, in Fig. 1(b), minority-spin states are observed around the Fermi level in the LDOS of the interfacial Mn and Si atoms. The spin polarizations of interface Mn and Si are -0.4 and 0.01, respectively. At the interface, the Mn atom loses half of its first nearest neighbor Co atoms, and non-bonding Mn *d* states (possibly d_{yz}, d_{zx} and $d_{3z^2-r^2}$) can appear around the Fermi level. Since the Mn $d_{3z^2-r^2}$ orbital hybridizes with the O p_z orbital at the interface, the LDOS of the interfacial Mn d_γ states maintain a half-metallic character. Contrary to this, the interfacial Mn d_ε orbitals (d_{yz} and d_{zx}) become nonbonding in the O-top configuration, reducing the spin polarization at the MnSi termination. Mavropoulos, *et al.* suggested that the interface states that appear in the minority-spin gap at the junctions of MTJs can also contribute to the tunneling conductance in anti-parallel magnetization, through spin mixing processes such as magnon excitations and inelastic scattering at RT.[76-78]

3.2 Spin-flip scattering at interfaces

Since the CMS/MgO(001) interface is not half-metallic

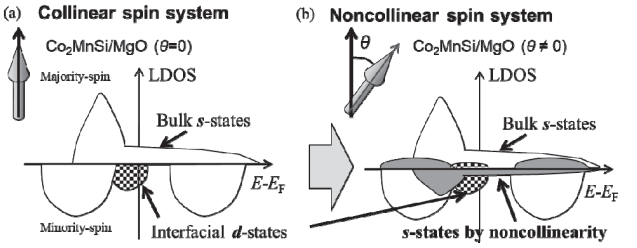

Fig. 3 Schematic images of LDOS for interface Co or Mn atoms of CMS in (a) collinear spin system (θ = 0) and (b) noncollinear spin system (θ ≠ 0), respectively. Gray areas and cross-hatched black areas indicate the interface *d*-states and interface *s*-states, respectively. ref. [81]

due to the appearance of non-bonding states in the minority-spin states around the Fermi level, the spin-flip scattering can be enhanced at finite temperature through the interface states as a result of the thermal fluctuation of magnetic spin moments.[79] Thus, the effects of thermal fluctuation and the noncollinear magnetic structure at the interface of MTJ on the spin-dependent transport are considered. The potential for a noncollinear-spin system was obtained by rotating the density matrix of a collinear-spin system with a spin-1/2 rotation matrix. According to Kübler's formulation,[79,80] off-diagonal elements of the effective potential that provide spin-mixing in the ballistic conductance are given by

$$(\delta E_{xc}/\delta n_\uparrow - \delta E_{xc}/\delta n_\downarrow)(\sin\theta\cos\varphi \pm i\sin\theta\sin\varphi)/2, \quad (1)$$

where $\delta E_{xc}/\delta n_s$ (s =↑, ↓) is the exchange and correlation potential in a collinear-spin system and θ and φ are the polar and azimuthal angles of a local spin moment with respect to the global spin-quantum axis, respectively. Since our calculations neglected spin-orbit interaction, the azimuthal angle φ did not affect the calculation results and was set to zero. The off-diagonal part of the local potential expressed by equation (1) is given at real-space positions of the supercell within each atomic sphere of interfacial atoms having a noncollinear spin moment.

Fig. 2 (a) shows the model system used for CMS/MgO/CMS MTJs with MnSi termination in the anti-parallel magnetization, where the interface Mn and sub-interface Co spin moments on both sides of the junction were canted by an angle θ in order to provide interfacial spin-flip scattering.[81] Figure 2(b) shows the conductance of a CMS/MgO/CMS MTJ with MnSi termination in parallel or anti-parallel magnetization as a function of the angle of the interface spin moments. zero conductance was obtained at θ = 0° for anti-parallel magnetization because of the half-metallic character of CMS. On the other hand, the anti-parallel conductance increased with increasing θ, while the parallel conductance decreased. This behavior can be attributed to spin-flip scattering because of the noncollinear interfacial magnetic structures. Fig. 2(c) shows the in-plane wave-vector (**k**∥) dependence of the tunneling conductance of the MTJ in anti-parallel magnetization with the interfacial Mn spin moment θ = 5°. It was already shown in ref. [74,75] that bulk CMS has a Δ_1 band at the Fermi level in the majority-spin states, and

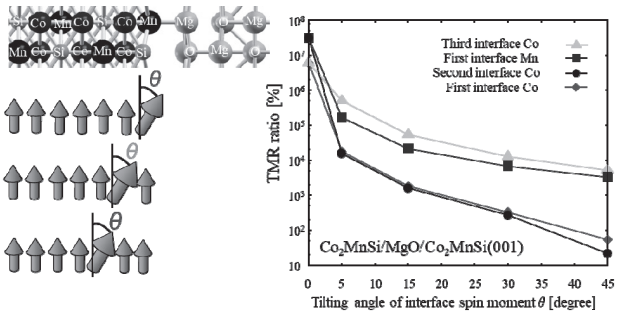

Fig. 4 Logarithmic plots of TMR ratios as a function of angle of local spin moment θ for noncollinear magnetic structures of various interfacial layers in CMS/MgO/CMS MTJs and Fe/MgO/Fe MTJs. ref. [81]

the $\mathbf{k}_{\parallel}$-dependence of the conductance of CMS/MgO/CMS MTJs in parallel magnetization has a broad peak at $\mathbf{k}_{\parallel} = (0,0)$ because of the slow decay of Δ_1 states in the MgO barrier.[9] As can be seen in Fig. 2(c), the $\mathbf{k}_{\parallel}$-dependence of the conductance in anti-parallel magnetization also shows a broad peak at $\mathbf{k}_{\parallel} = (0,0)$, indicating that the spin-flip conductance is dominated by the Δ_1 channel of the conducting electrons.

Fig. 3 shows schematic images of the LDOS of interface Mn and sub-interface Co atoms in collinear spin ($\theta = 0^\circ$) and noncollinear spin ($\theta \neq 0^\circ$) cases.[81] In the case of a collinear spin system, the CMS/MgO interface is not half-metallic and has interface states in the half-metallic gap of minority-spin states originating from the non-bonding Mn *d* orbital (see also Fig. 3 in ref. [75]). Then, the noncollinear spin moments of interface Mn and Co generate spin-mixing in the LDOS of CMS/MgO/CMS(001). At the Fermi level, as shown in Fig. 3(b), both bulk *s*-states and interfacial Mn *d*-states are projected on the majority-spin and minority-spin states of the global spin-quantum axis, providing spin-flip scattering of the Ballistic conductance. The broad peak at $\mathbf{k}_{\parallel} = (0,0)$ in Fig. 3(c) indicates that the projected minority-spin Δ_1 states mainly contribute to the conductance in anti-parallel magnetization. This means that the contribution of the interfacial d-states that appeared at the MnSi termination of CMS/MgO junctions in the collinear-spin system (cross-hatched black areas in Fig. 3(a) and (b)) was rather small compared to that of the *s*-states caused by the noncollinearity of interfacial Mn and Co spin moments (light-gray areas in Fig. 3(b)). Since the interface states were mainly composed of d_{xy} and $d_{x^2-y^2}$ orbitals of interfacial Mn and Co atoms, they show fast decay in the MgO barrier.

3.3 Effects of noncollinear magnetism on TMR

To examine the interfacial structure dependence of the spin-flip conductance, Fig. 4 shows logarithmic plots of TMR ratios as a function of the angle of the local spin moment θ in various interfacial layers of CMS/MgO/CMS. First, I can confirm that the TMR ratios of the MTJs decreased with increasing θ due to the spin-flip conductance in the interfacial region. In particular, the TMR ratios for CMS/MgO/CMS MTJs with noncollinear first and second interface Co spin moments had values similar to that of Fe/MgO/Fe MTJs for $\theta > 5^\circ$. This indicates that the advantage of half-metallic electrodes is valid only for small θ if the noncollinearity arises at interfacial Co spin moments. On the other hand, the decrease in the TMR ratio with increasing θ was rather gradual for MTJs with noncollinearity in the first interface Mn spin moment at the MnSi termination and the third interface Co spin moment, compared to that in the first and second Co layers, indicating that the spin-flip conductance was suppressed at the interfacial MnSi-layers and that spin-flip scattering mainly occurred in the first and second Co layers. Since the Si atom is nonmagnetic, the off-diagonal part of the effective potential expressed by $(\delta E_{xc}/\delta n_{\uparrow} - \delta E_{xc}/\delta n_{\downarrow})$ was rather small, which led to a suppression of the spin-flip probability at the MnSi-layer. In the calculations, the angle dependence of the size of the Co and Mn spin moments was neglected. This is a reasonable approximation for Mn spin moments in view of their localized character in bulk CMS[82,83] and MnSi-terminated interfaces.[84] For Co-terminated interfaces, the strong hybridization between Co and O atoms can cause angular dependence for the interfacial Co spin moments. As discussed for Ni spin moments in NiMnSb,[85] longitudinal fluctuations will increase the length of the local spin moments with increasing angle. This will enhance spin-flip scattering in interfacial regions, resulting in further decrease in the TMR ratio.

3.4 Exchange stiffness at interfaces

To estimate the exchange stiffness of the interfacial spin moments, The increase in the one-electron band energy $E(\theta)$ relative to the collinear-spin system ($\theta = 0^\circ$) was calculated. Fig. 5(a) shows $E(\theta)$ as a function of the angle of local moments θ for various interfacial layers in CMS/MgO(001) and Fe/MgO(001) junctions.[81] Then, the results were fitted using $E(\theta) = B(1-\cos\theta)$. Here, B is the inter-atomic-layer exchange stiffness constant; the value in Table 3 for each layer in the interfacial and bulk regions is shown in Table 3. This estimation corresponds to the magnetic force theorem method.[86,87]

It was confirmed that the increase in the band energy as a function of the canting angle shown in Fig. 5(a) can be fitted by $\sim \theta^2$ up to $\theta = 30^\circ$. This means that the error in the estimation of the exchange stiffness constant by the magnetic force theorem is very small in the present system.[88] First, it can be found that the exchange stiffness of the interfacial Co layer at the Co termination was much smaller than that of the interfacial MnSi-layer at the MnSi termination and that of bulk CMS. These results are consistent with the results of recent first-principles calculations of the exchange constant of CMS/MgO(001).[89]

Furthermore, the exchange stiffness of the

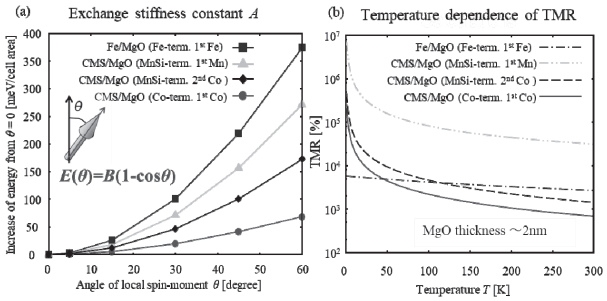

Fig. 5 (a) Increase in band energy relative to that of collinear-spin system $E(\theta)$ as a function of angle of local spin moments θ for first-layer Co spin moment at Co termination, first-layer Mn spin moment and second-layer Co spin moment of CMS/MgO(001), and first-layer Fe spin moment of Fe/MgO(001) junctions. ref. [81] (b) Temperature dependence of TMR ratios of CMS/MgO/CMS(001) and Fe/MgO/Fe(001) calculated by Eq. (2) including noncollinear spin structure of various spin moments.

sub-interfacial Co-layer at the MnSi termination was smaller than that of the interfacial MnSi-layer. This means that at the MnSi termination, the sub-interfacial Co spin moments fluctuate more easily than interfacial Mn spin moments. On the other hand, a very high exchange stiffness was found for the interfacial Fe-layer at Fe/MgO junctions compared to those of CMS/MgO junctions, indicating the robustness of interfacial Fe spin moments against thermal fluctuation. One possible reason for this behavior of the exchange stiffness in interfacial regions compared to that of bulk CMS is related to the change in the interfacial spin moments.

As is discussed in ref. [75,84] the majority-spin charge of interfacial Co atoms transfers to the MgO side because of the strong bonding between Co and O atoms. On the other hand, the interfacial Mn spin moments of the CMS/MgO junction[74,84] and interfacial Fe spin moments of the Fe/MgO junction[9,81] increase in comparison with those of the bulk because of the localization effect (and band-narrowing effect) of the non-bonding *d*-orbitals in the interfacial regions. Since $E(\theta)$ can be characterized by the off-diagonal elements of the local potential expressed by equation (1), the decrease (increase) of local spin moments reduced (enhanced) the off-diagonal terms, leading to the low (high) exchange stiffness.

3.5 Temperature dependence of TMR

Finally, I discuss the effect of interfacial spin-flip scattering on the TMR ratios at finite temperatures. To estimate the TMR ratio at a finite temperature, the Boltzmann average of the tunneling conductance was calculated using the following equation,

$$G_{P(AP)}(\theta) = \int g_{P(AP)}(\theta) \exp(-2E(\theta) / k_B T) \sin\theta \, d\theta \Big/ \int \exp(-2E(\theta) / k_B T) \sin\theta \, d\theta, \quad (2)$$

where $g_{P(AP)}(\theta)$ is the θ-dependence of the tunneling conductance in parallel (P) and anti-parallel (AP) magnetization, as shown in Fig. 2(b). $E(\theta)$ is the increase in the band energy caused by the noncollinearity of the local spin moments at each interfacial layer, as discussed in the previous paragraph. The factor of 2 for $E(\theta)$ indicates contribution from both sides of the MTJs.

Fig. 5(b) shows the calculated temperature dependence of the TMR ratio for the MTJs of CMS/MgO/CMS and Fe/MgO/Fe MTJs with 2 nm MgO thickness. As can be seen here, the reduction in the TMR ratios of CMS/MgO/CMS MTJs with the 1st layer Co spin fluctuation at Co termination and the 2nd layer Co spin fluctuation at MnSi termination are much faster than that of Fe/MgO/Fe MTJs with 1st layer Fe spin fluctuation. This means that the interfacial spin-flip scattering significantly reduces the TMR ratio at RT.

This result qualitatively agrees with the results of the temperature dependence of the TMR ratio. The temperature dependence of the TMR ratios of CMS/MgO/CMS MTJs with the 1st layer Mn spin fluctuation at the MnSi termination is also significant, but the TMR ratio maintains a large value at RT, indicating that the large exchange stiffness constant at the interface improves the TMR ratio at RT. The tunneling conductance evaluated at finite temperature using equation (2) is 700% at RT for CMS/MgO/CMS MTJs with the thermal fluctuation of the first layer Co spin moment at the Co termination, and 1500% at RT with the thermal fluctuation of the 2nd Co spin moment at the MnSi termination. These TMR ratios are smaller than the TMR ratio of 2500% at 300 K for Fe/MgO/Fe MTJs with thermal fluctuation of the 1st layer Fe spin moment.

From these results, I can conclude that the experimentally observed low TMR ratio of the MTJs at RT can be attributed to the spin-flip conductance caused by thermal fluctuation of the interfacial spin moments. Therefore, to suppress the reduction of the TMR ratios at finite temperature in CMS/MgO/CMS MTJs, the exchange stiffness of Co spin moments at the CMS/MgO(001) interface must be enhanced. In estimating the thermal average of the tunneling conductance, $E(\theta)$ was treated as the thermal excitation energy of the local spin moments per in-plane unit cell area, which corresponds to the replacement of various

Table 3 Inter-layer exchange stiffness constant B meV/u.c.a. fitted to increase in band energies $E(\theta)=B(1-\cos\theta)$ due to noncollinearity of local spin moments for CMS/MgO(001) and Fe/MgO(001) junctions. 1st and 2nd indicate first and second layer at the interface with MgO, respectively. u.c.a. is unit-cell area ~32 Å^2. Ref.[81]

B meV/u.c.a.	Co^{1st}	Co^{2nd}	Mn^{1st}	Fe^{1st}
Bulk (CMS or Fe)	414	414	565	600
MgO interface	145	347	529	753

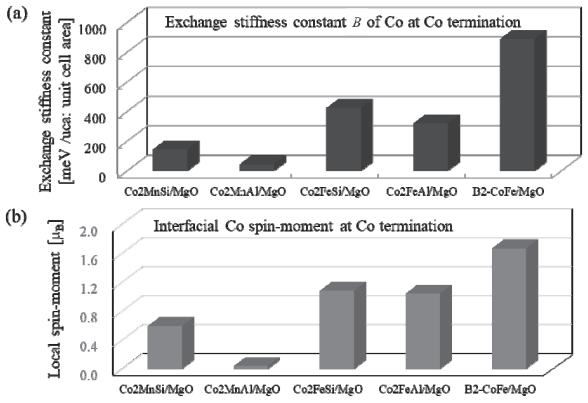

Fig. 6 (a) Exchange stiffness constant B of Co atom at Co termination of various MgO interfaces with Co-based Heusler compounds and B2-CoFe. Estimation of exchange stiffness constant B is same as in Fig. 5(a). (b) Interfacial Co spin moments at Co terminations of various MgO interfaces with Co-based Heusler compounds and B2-CoFe.

magnetic excitation modes at interfacial regions by a single excitation mode of interfacial spin moments given by the in-plane unit cell $E(\theta)$. If other magnon excitation modes are considered, the temperature dependence of TMR shown in Fig. 5(b) will change. However, the inclusion of the other excitation modes in equation (2) will lead to a further decrease in the TMR ratio at RT, and the chemical trend of the exchange stiffness at the interface has little dependence on the excitation modes. Therefore, our conclusion that the significant reduction of the TMR ratio of CMS/MgO/CMS MTJs at RT can be attributed to the interfacial spin-flip conductance does not change with a more accurate estimation of the thermally averaged tunneling conductance.

3.6 Enhancement of interface exchange stiffness

It was concluded that the reduction in the TMR ratio in CMS/MgO/CMS MTJs at RT can be attributed to spin-flip scattering in the interfacial region caused by thermal fluctuation of interfacial and sub-interfacial Co layers, and to suppress reduction in the TMR ratio at RT, it is important to enhance the exchange stiffness of Co layers at CMS/MgO junctions. Thus, I calculated the exchange stiffness constant at the interface of MgO for the other Heusler compounds and B2-CoFe. Fig. 6 shows a bar graph of the inter-atomic layer exchange stiffness constant at each interface. As shown in Fig. 6, very large exchange stiffness constants were obtained for the Co-terminated B2-CoFe/MgO interface, indicating that the B2-CoFe/MgO interface is very robust against thermal fluctuation.

Furthermore, the exchange stiffness of the Co-terminated Co_2FeSi(CFS)/MgO and Co_2FeAl(CFA)/MgO interfaces is larger than that of CMS/MgO and Co_2MnAl(CMA)/MgO interfaces. Thus, in order to suppress the thermal fluctuation at the interface with MgO, CFS and CFA are better than CMS and CMA. It was considered that the behavior of the exchange stiffness in the interfacial region is related to the behavior of the interfacial spin moments, because the exchange stiffness constant is proportional to the square of the local spin moments. In fact, as can be seen here, the behavior of the interfacial Co spin moments is consistent with the behavior of the interfacial exchange stiffness constant. This means that the enhancement of the interfacial Co spin moment is effective to obtain a large exchange stiffness constant and suppress the thermal fluctuation of Co spin moments at the MgO junction.

3.7 New physical property for temperature dependence of TMR

Recently, a new physical property characterizing the temperature dependence of TMR in MTJs was proposed in ref. [90] It was found that the intra-atomic s–d exchange coupling J_{sd} at the interface was also a key parameter in the reduction of TMR at RT. Masuda described the temperature dependent spin-flip Hamiltonian including J_{sd} at the interface Fe of Fe/MgO/Fe(001) MTJs by the coherent potential approximation of various magnetization directions according to the temperature dependence of the magnetization up to the Curie temperature. A smaller J_{sd} can disconnect the coupling between conductive s electrons and localized d electrons, leading to suppression of the spin-flip scattering at the interface. Therefore, ferromagnetic materials with smaller J_{sd} will be preferable to obtain larger TMR at RT. This new physical parameter J_{sd} will also be important for improving the large temperature dependence of the TMR of Heusler based-MTJs.

4. Spin-dependent transport in CPP-GMR devices

4.1 Valet-Fert model

According to Valet and Fert's two-current model,[91] the resistance change-area product between parallel and antiparallel magnetization configurations ($\Delta RA = R_{AP}A - R_PA$) can be expressed by two intrinsic factors in spin-dependent electron scattering. They are the bulk spin-asymmetry coefficient (β) in ferromagnetic (FM) layers and the interfacial spin-asymmetry coefficient (γ), which are included in the following equation,

$$\Delta RA = (\beta\,\rho^*_F + 2\,\gamma\,\rho^*_N\,r^*_b)/(\,\rho^*_F\,t_F + \rho^*_N\,t_N + 2\,r^*_b) \quad (3)$$

where ρ^*_F and ρ^*_N are the resistivity of the ferromagnetic electrode and the non-magnetic (NM) spacer layer in the bulk, and the t_F and t_N are the thickness of the FM and NM layers, respectively. The r^*_b is the spin-independent interface resistance. The β is enhanced by using the HMF in the FM layer, while enhancement of the γ is accomplished by reduction of the interface resistance RFM/NM through the choice of non-ferromagnetic (NM) spacers. Here, I mainly discuss the γ in HFM/NM interface, because the temperature dependence of is much larger than that of the bulk spin

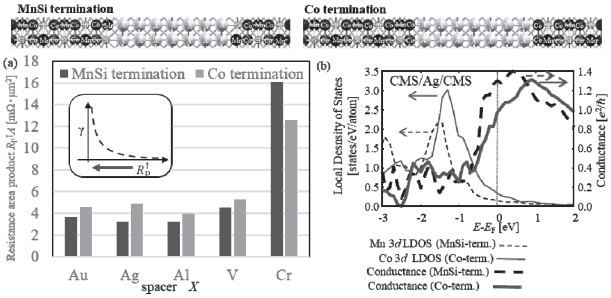

Fig. 7 (a) Bar graph comparing transmittance of CMS/*X*/CMS(001) for *X* = Au, Ag, Al, V and Cr with MnSi and Co termination. (b) LDOS of interfacial Co-*d* at Co termination and interfacial Mn-*d* at MnSi termination in CMS/Ag/CMS(001), together with transmittance averaged over the whole $\mathbf{k}_{\parallel}$ region as function of energy relative to Fermi energy. ref. [92].

asymmetry ß.

The γ is expressed by the majority-spin resistance ($R_P{}^{\uparrow}$) and minority-spin interface resistance ($R_P{}^{\downarrow}$) in the parallel magnetization configuration as follows,

$$\gamma = (R_P{}^{\downarrow} - R_P{}^{\uparrow})/(R_P{}^{\downarrow} + R_P{}^{\uparrow}) \quad (4)$$

The $R_P{}^{\downarrow}$ at the HMF/NM interface is determined by the interface state-mediated spin-flip scattering, as discussed in the previous section, because there are no states around the Fermi level of HMF minority-spin states in the bulk. In HMF/NM junctions, there are many scattering processes, making them complicated compared with HMF/insulator junctions such as Heusler/MgO. This results in a finite value for $R_P{}^{\downarrow}$ in the HMF/NM junctions, which will be difficult to control experimentally. On the other hand, the $R_P{}^{\uparrow}$ will be determined by the matching of the conductive channel between the majority-spin states of HMF and NM. Thus, in CPP-GMR devices with HMFs, matching of the majority-spin band dispersions with the NM spacer is important to reduce the $R_P{}^{\uparrow}$ of HMF/NM interfaces. As shown in the inset of Fig. 7(a), γ will rapidly increase with decreasing $R_P{}^{\uparrow}$ under fixed $R_P{}^{\downarrow}$. This means that the choice of NM spacer layer is very important to enhance the CPP-GMR with HFM Heusler compounds.

4.2 Comparison of the transmittance for CMS/*X*/CMS

As discussed in ref., [56] the transport properties obtained from the Landauer formula do not give the real conductance and resistance for a three-dimensional metallic multilayer. However, our aim in this paper is not to obtain the quantitatively correct conductance and resistance of HFM/NM/HFM junctions, but to clarify the differences in the conductance and resistance thorough HFM/NM junctions depending on the NM spacer and the interfacial termination. If the electrode region (ferromagnetic layer) consists of Co_2MnSi (CMS) for all cases, the difference in resistance between HFM/NM/HMF and HFM/NM'/HFM junctions indicates the difference in the interfacial resistance between the HFM/NM and HFM/NM' junctions, which can originate from electron scattering due to changes in the local potential and band structures at the interfacial region. Furthermore, a completely epitaxial multi-layer was assumed, where the crystal momentum parallel to the layer (or $\mathbf{k}_{\parallel}$) is conserved because of the two-dimensional periodicity of the system, and the number of conductive channels perpendicular to the plane is less than about five or six per $\mathbf{k}_{\parallel}$. Therefore, the ballistic transport calculations from the Landauer formula can be applied to evaluate the difference in the interfacial resistance depending on the band structures of the materials on both sides of the interface. This point has already been confirmed in our previous work in ref. [56] where the difference in the resistance-area products in the ballistic transport calculation between CMS/Cr/CMS(001) and CMS/Ag/CMS(001) is roughly comparable to that obtained experimentally. It is considered that this justifies the use of the Landauer formula for the investigation of the interfacial resistance of all metallic multilayers depending on the non-ferromagnetic spacer and the interfacial termination.

Figure 7 shows the majority-spin resistance-area product of CMS/*X*/CMS(001) with MnSi termination and Co termination for NM spacer *X* = fcc-Au, fcc-Ag, fcc-Al, bcc-V, and anti-ferromagnetic bcc-Cr in the parallel magnetization configuration.[92] First, Fig. 7 shows that the majority-spin resistance-area product $R_P{}^{\uparrow}A$ of the junctions with *X* = Au, Ag, Al, and V is about 3~5 mΩ·μm², which corresponds to a conductance of 0.6~1.0 G_0, where $G_0 = e^2/h$ is the ballistic conductance without scattering in the Landauer formula. On the other hand, the junctions with anti-ferromagnetic bcc-Cr spacer are about 13~16 mΩ·μm², which is 3~5 larger than that with the other spacer. These results qualitatively agree with recent experimental results on CPP-GMR devices incorporating epitaxial CMS/Ag/CMS and CMS/Cr/CMS, where a smaller resistance-area product has been obtained for the CMS/Ag(001) interface than for CMS/Cr(001).

The other feature of the transmittance of CMS/*X*/CMS(001) shown in Fig. 7 is the interface-structure dependence, i.e., the resistance-area product with Co termination is larger than that with MnSi termination except for the anti-ferromagnetic bcc-Cr spacer. Analyzing the $\mathbf{k}_{\parallel}$-dependence of the majority-spin transmittance at $E = E_F$ for CMS/*X*/CMS with Co and MnSi termination, I found that the difference in transmittance between the two terminations is significant at $k_x \neq 0$, especially for *X* = Ag, Au, Al and V. This means that the transmittance in the whole $\mathbf{k}_{\parallel}$ region contributes to the interface-structure dependence. To understand this, I show in Fig. 7(b) the local density of states (LDOS) of interfacial Co-*d* at the Co-terminated interface and interfacial Mn-3d at the MnSi-terminated interface in CMS/Ag(001), together with the transmittance averaged

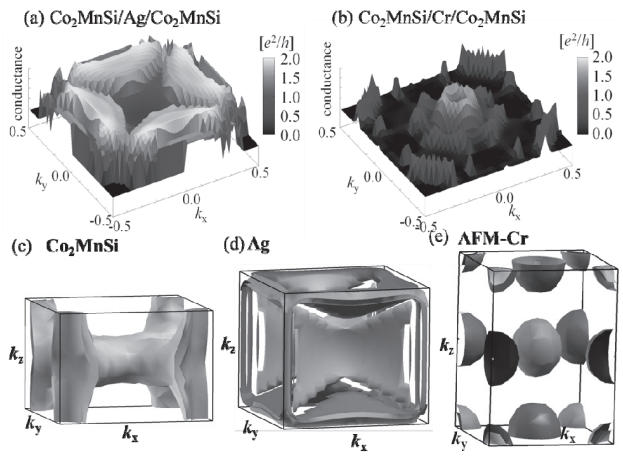

Fig. 8 Majority-spin conductance in parallel magnetization configuration calculated for (a) CMS/Ag/CMS and (b) CMS/Cr/CMS as function of $\mathbf{k}_{\parallel} = (k_x, k_y)$. Fermi surfaces in Brillouin zone corresponding to tetragonal unit cell of (c) $L2_1$-CMS, (d) fcc-Ag, and (e) anti-ferromagnetic (AFM) bcc-Cr plotted by XCRYSDEN.[93] ref.[56]

over the whole $\mathbf{k}_{\parallel}$ region as a function of the energy relative to the Fermi energy. It is evident that the transmittance increases with the decrease in the *d* component of the LDOS of interfacial atoms, indicating that the interfacial d-orbitals act as a scatterer of electrons. Furthermore, I found that the LDOS of Co-*d* at the Co termination shows large components at the Fermi level compared with those of Mn at the MnSi termination. The large *d*-components at the interfacial regions cause additional reflection of propagating electrons, leading to the large interfacial resistance in metallic multilayer. These features can be observed also in the LDOS of CMS/Au, CMS/Al and CMS/V interfaces.

4.3 Fermi surface matching at HFM/NM interface

Figures 8(a) and (b) show the $\mathbf{k}_{\parallel}$-dependence of the majority-spin conductance in the parallel magnetization configuration of CMS/Ag/CMS and CMS/Cr/CMS. It is clearly seen that the conducting channels of CMS/Cr/CMS are restricted to a small region around $\mathbf{k}_{\parallel} = (0,0)$. On the other hand, highly conducting channels spread over almost the entire region in the $\mathbf{k}_{\parallel}$ plane for CMS/Ag/CMS. The highly conducting region in the $\mathbf{k}_{\parallel}$ plane can be understood qualitatively by considering the matching of the Fermi surface over the $\mathbf{k}_{\parallel}$-plane between CMS and Ag.

Figures 8(c)-(e) show the Fermi surfaces in the Brillouin zones of $L2_1$-CMS, fcc-Ag, and AFM bcc-Cr with a tetragonal unit cell. A large overlapping area of the Fermi surface can be seen on the $\mathbf{k}_{\parallel}$-plane between CMS and Ag, resulting in the small resistance-area product ($2R_{\mathrm{CMS/Ag}}A$ = 3.21 mΩ·μm^2) for CMS/Ag/CMS, while the mismatch of the Fermi surface between CMS and Cr causes the large resistance-area product

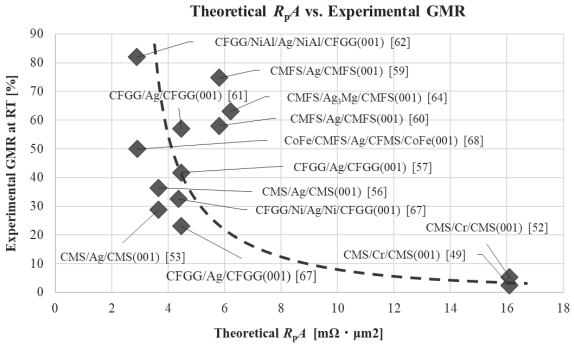

Fig. 9 Correlation between experimental CPP-GMR ratios at room temperature vs. theoretical resistance-area product R_P for various CPP-GMR devices in experiments. Broken line indicates interface spin asymmetry γ as function of majority-spin interface resistance in parallel magnetization $R_P{}^{\uparrow}$.

($2R_{\mathrm{CMS/Cr}}A$ = 16.1 mΩ·μm^2) of CMS/Cr/CMS. Although no conductance (infinite resistance) is expected in the minority-spin channel in ideal half-metals, a finite resistance-area product could appear in the minority-spin channel in real half-metals owing to such reasons such as atomic disorder, thermal fluctuation of magnetic moments, spin-orbit coupling, and so on. The minority-spin resistance-area product causes a reduction in both β and γ. Thus, one can expect a larger value of γ for CMS/Ag/CMS compared to CMS/Cr/CMS, since the majority-spin resistance-area product of CMS/Ag/CMS is much smaller than that of CMS/Cr/CMS.

Experimentally, the CMS/Ag/CMS and CMS/Cr/CMS junctions with the same annealing temperature (350°C) and exactly the same stacking structure except for the spacer layer showed *RA* of 51.4 and 66.9 mΩ·μm^2, respectively.[56] Here, the difference of *RA* (~ 15.5 mΩ·μm^2) between them is mainly caused by the difference in interface resistances, i.e., $R_{\mathrm{CMS/Ag}}A$ and $R_{\mathrm{CMS/Cr}}A$, because the contribution of the bulk resistance in Ag and Cr spacers is negligibly small. Although the experimental RA is much higher than the calculated $2R_{\mathrm{CMS/NM}}A$ (NM = Ag or Cr) since it includes all of resistances in the CPP-pillar, the difference in *RA*, i.e., $2R_{\mathrm{CMS/Cr}}A - 2R_{\mathrm{CMS/Ag}}A$ of 15.5 mΩ·μm^2 is roughly comparable to the calculated one (~ 12.9 mΩ·μm^2). This agreement is evidence of a small interface resistance and large γ between CMS and Ag due to good Fermi-surface matching, as predicted in our calculations.

4.4 Correlation between theoretical R_P and experimental CPP-GMR

Fig. 9 shows the experimental CPP-GMR in various systems as a function of the calculated majority-spin resistance-area product in parallel magnetization for the corresponding systems. As can be seen in Fig. 9, the

experimental CPP-GMR ratio increases with the decrease in the theoretical RPA, which is roughly consistent with the $R_P^{\uparrow}$ dependence of the interface spin asymmetry γ as shown in the inset of Fig. 7. This means that the enhancement of γ by the matching of the conductive channel between HFM and NM through Fermi surface matching is very important to obtain large CPP-GMR. In experiments, insertion of B2-type NiAl between $Co_2FeGa_{0.5}Ge_{0.5}$ (CFGG) and the Ag spacer dramatically enhanced the CPP-GMR and ΔRA both at LT and RT[62]. This modification was motivated by a theoretical calculation showing that the Fermi surface matching between CFGG and B2-type NiAl is much better than that of CFGG and Ag. Furthermore, the experimental results showed that not only NiAl but also Ni insertion between CFGG and the Ag spacer enhanced the CPP-GMR[67]. This result is also confirmed by theoretical calculations showing that CFGG/Ni/Ag/Ni/CFGG exhibits smaller $R_P^{\uparrow}$ than CFGG/Ag/CFGG. More recently, half-metallic $Co_2FeMnSi$ (CFMS) was inserted between A2-CoFe and Ag spacer, and the CPP-GMR was maximized when the thickness of CFMS was around 7 nm[68]. One possible reason for the large CPP-GMR was attributed to the better Fermi surface matching of CFMS/CoFe as compared with CoFe/Ag. All these results indicate that Fermi surface matching between HFM and the NM spacer layer is a key factor in enhancing the CPP-GMR for future ultra-sensitive magneto-resistive sensors.

5. Summary

In this paper, first-principles studies on electronic structures and ballistic transport properties of HMF Co-based Heusler compound-based magneto-resistive devices were reviewed.

The effects of spin-flip scattering by interfacial noncollinear magnetic structures on the TMR ratios of MTJs with Co_2MnSi(CMS) and MgO were investigated using first-principles calculations. It was found that the effects of the noncollinearity of interfacial Co spin moments on the TMR are significant in determining the spin-flip conductance. Furthermore, the inter-atomic layer exchange stiffness constant of interfacial and sub-interfacial Co spin moments at CMS/MgO junctions is much smaller than that in bulk regions. From these results, I conclude that the low TMR ratio at room temperature in MTJs with half-metallic Co-based full Heusler compounds can be attributed to spin-flip scattering by the noncollinear magnetic structures of interfacial Co as a result of thermal fluctuations. These results are validated by recent experimental results, i.e., the significant reduction in the TMR ratios of CMS/MgO/CMS MTJs at RT compared to those of Fe/MgO/Fe MTJs. This means that the spin-flip scattering at the interface is at least as important as any other effect. I showed that the interfacial exchange stiffness can be strongly enhanced by inserting an ultrathin B2-CoFe layer in CMS/MgO junctions, leading to a larger TMR ratio at room temperature.

For CPP-GMR, the ballistic conductance of HFM/NM/HFM was calculated in order to clarify the origin of interfacial resistance. The majority-spin transmittance of CMS/*X*/CMS(001) in the parallel magnetization configuration was calculated by the Landauer formula, and it was found that the matching of the Fermi surface projected to the two-dimensional Brillouin zone in in-plane wave vector $\mathbf{k}_{\parallel}$ between CMS and NM spacers is a main contributing factor to the interfacial resistance among spacers. The experimental CPP-GMR was well reproduced as a function of the theoretical resistance-area product in parallel magnetization through the equation of interface spin asymmetry γ.

All these findings suggest that the TMR ratios of MTJs and CPP-GMR with half-metallic Co-based full Heusler compounds can be designed by controlling their interfaces, which is worth further investigation.

Acknowledgements I am grateful to M. Shirai and K. Abe of Tohoku University, K. Hono, S. Mitani, Y. Sakuraba, H. Sukegawa, S. Kasai, K. Masuda and I. Kurniawan of the Na-tional Institute for Materials Science, and K. Nawa of Mie University for valuable discussions on this work. This work was partly supported by Grants-in-Aid for Scientific Research (Grant Nos. 17H06152, 20H00299, 20H02190, 20H02186, 21H01750 and 22H04966) from the Japan Society for the Pro-motion of Science, Center for Spintronics Research Network (CSRN) of Osaka University, and the Cooperative Research Project Program of the Research Institute of Electrical Communication in Tohoku University.

References

1) M. N. Baibich, J. M. Broto, A. Fert, F. Nguyen Van Dau, F. Petroff, P. Etienne, G. Creuzet, A. Friederich, and J. Chazelas: *Phys. Rev. Lett.* **61**, 2472 (1988).
2) G. Binasch, P. Grünberg, F. Saurenbach, and W. Zinn: *Phys. Rev. B* **39**, 4828 (1989).
3) T. Miyazaki and N. Tezuka: *J. Magn. Magn. Mater.* **139**, L231 (1995).
4) T. Hanyu, T. Endoh, D. Suzuki, H. Koike, Y. Ma, N. Onizawa, M. Natsui, S. Ikeda, and H. Ohno: *Proc. IEEE* **104**, 1844 (2016).
5) D. Ielmini and S. Ambrogio: *Nanotechnology* **31**, 092001 (2020).
6) S. Yuasa, T. Nagahama, A. Fukushima, Y. Suzuki, and K. Ando: *Nature Material* **3**, 868 (2004).
7) S. S. P. Parkin, C. Kaiser, A. Panchula, P. M. Rice, B. Hughes, M. Samant, and S.-H. Yang: *Nature Material* **3**, 862 (2004).
8) S. Ikeda, J. Hayakawa, Y. M. Lee, F. Matsukura, Y. Ohno, T. Hanyu, and H. Ohno: *IEEE Trans. Electron Dev.* **54**, 991 (2007).
9) W. H. Butler, X.-G. Zhang, T. C. Schulthess, and J. M. MacLaren: *Phys. Rev. B* **63**, 054416 (2001).
10) J. Mathon and A. Umerski: *Phys. Rev. B* **63**, 220403(R) (2001).
11) R. A. de Groot, F. M. Mueller, P. G. van Engen, and K. H. J. Buschow: *Phys. Rev. Lett.* **50**, 2024 (1983).
12) K. Schwarz: *J. Phys. F* **16**, L211 (1986).

13) W. E. Pickett and D. J. Singh: *Phys. Rev. B* **53**, 1146 (1996).
14) S. Ishida, S. Fujii, S. Kashiwagi, and S. Asano: *J. Phys. Soc. Jpn* **64**, 2152 (1995).
15) S. Picozzi, A. Continenza, and A. J. Freeman: *Phys. Rev. B* **66**, 094421 (2002).
16) I. Galanakis, P. H. Dederichs, and N. Papanikolaou: *Phys. Rev. B* **66**, 174429 (2002).
17) Y. Miura, K. Nagao, and M. Shirai: *Phys. Rev. B* **69**, 144413 (2004); *J. Appl. Phys.* **95**, 7225 (2004).
18) S. Picozzi, A. Continenza and A. J. Freeman: *Phys. Rev. B* **69**, 094423 (2004).
19) Y. Miura, M. Shirai, and K. Nagao: *J. Appl. Phys.* **99**, 08J112 (2006).
20) M. Miyamoto, A. Kimura, Y. Miura, M. Shirai, M. Ye, Y. Cui, K. Shimada, H. Namatame, M. Taniguchi, Y. Takeda, Y. Saitoh, E. Ikenaga, S. Ueda, K. Kobayashi and T. Kanomata: *Phys. Rev. B* **79**, 100405(R) (2009).
21) S. Ueda, Y. Miura, Y. Fujita and Y. Sakuraba: *Phys. Rev. B* **106**, 075101 (2022).
22) B. L. Gyorffy, A. J. Pindor, J. Staunton, G. M. Stocks and H. Winter: *J. Phys. F Met. Phys.* **15**, 1337 (1985).
23) K. Nawa, I. Kurniawan, K. Masuda, Y. Miura, C. E. Patrick and J. B. Staunton: *Phys. Rev. B* **102**, 054424 (2020).
24) I. Kurniawan, K. Nawa, K. Masuda, Y. Miura and K. Hono: *Acta Materialia* **218**, 117218 (2021).
25) I. Kurniawan, Y. Miura and K. Hono: *Phys. Rev. Mat.* **6**, L091402 (2022).
26) K. Inomata, S. Okamura, R. Goto, and N. Tezuka: *Jpn. J. Appl. Phys.* **42**, L419 (2003).
27) H. Kubota, J. Nakata, M. Oogane, Y. Ando, A. Sakuma, and T. Miyazaki: *Jpn. J. Appl. Phys.* **43**, L984 (2004).
28) S. Okamura, A. Miyazaki, S. Sugimoto, N. Tezuka, and K. Inomata: *Appl. Phys. Lett.* **86**, 232503 (2005).
29) Y. Sakuraba, M. Hattori, M. Oogane, Y. Ando, H. Kato, A. Sakuma, T. Miyazaki and H. Kubota: *Appl. Phys. Lett.* **88**, 192508 (2006).
30) N. Tezuka, N. Ikeda, A. Miyazaki, S. Sugimoto, M. Kikuchi and K. Inomata: *Appl. Phys. Lett.* **89**, 112514 (2006).
31) T. Marukame and M. Yamamoto: *Appl. Phys. Lett.* **101**, 083906 (2007).
32) S. Tsunegi, Y. Sakuraba, M. Oogane, K. Takanashi and Y. Ando: *Appl. Phys. Lett.* **93**, 112506 (2008).
33) T. Ishikawa, N. Itabashi, T. Taira, K-i. Matsuda, T. Uemura and M. Yamamoto: *Appl. Phys. Lett.* **94**, 092503 (2009).
34) N. Tezuka, N. Ikeda, F. Mitsuhashi and S. Sugimoto: *Appl. Phys. Lett.* **94**, 162504 (2009).
35) H. Sukegawa, W. Wang, R. Shan, T. Nakatani, K. Inomata and K. Hono: *Phys. Rev. B* **79**, 184418 (2009).
36) W. Wang, H. Sukegawa, K. Inomata: *Phys. Rev. B* **82**, 092402 (2010).
37) H. Liu, Y. Honda, T. Taira, K.-i. Matsuda, M. Arita, T. Uemura and M. Yamamoto: *Appl. Phys. Lett.* **101**, 132418 (2012).
38) H. Liu, T. Kawami, K. Moges, T. Uemura, M. Yamamoto, F. Shi and P. M. Voyles: *J. Phys. D: Appl. Phys.* **48**, 164001 (2015).
39) T. Scheike, H. Sukegawa, K. Inomata, T. Ohkubo, K. Hono and S. Mitani: *Appl. Phys. Exp.* **9**, 053004 (2016).
40) B. Hu, K. Moges, Y. Honda, H. Liu, T. Umemura and M. Yamamoto: *Phys. Rev. B* **94**, 094428 (2016).
41) S. Kasai, Y. K. Takahashi, P.-H. Cheng, Ikhtar, T. Ohkubo, K. Kondou, Y. Otani, S. Mitani and K. Hono: *Appl. Phys. Lett.* **109**, 032409 (2016).
42) K. Mukaiyama, J. W. Jung, H. Sepehri-Amin, S. Kasai, T. Furubayashi, T. Ohkubo and K. Hono: *Appl. Phys. Lett.* **114**, 172402 (2019).
43) T. Scheike, Z. Wen, H. Sukegawa and S. Mitani: *Appl. Phys. Lett.* **122**, 112404 (2023).
44) T. Kubota, Y. Miura, D. Watanabe, S. Mizukami, F. Wu, H. Naganuma, X. Zhang, M. Oogane, M. Shirai, Y. Ando and T. Miyazaki: *Appl. Phys. Exp.* **44**, 043002 (2011).
45) H. Kurt, N. Baadji, K. Rode, M. Venkatesan, P. Stamenov, S. Sanvito and J. M. D. Coey: *Appl. Phys. Lett.* **101**, 132410 (2012).
46) W. S. Yun, G.-B. Cha, I. G. Kim, S. H. Rhim and S. C. Hong: *J. Phys.: Condens. Matter* **24**, 416003 (2012).
47) Y. Miura and M. Shirai: *IEEE Trans. Mag.* **50**, 1400504 (2014).
48) T. Kubota, S. Mizukami, Q. L. Ma, H. Naganuma, M. Oogane, Y. Ando and T. Miyazaki: *J. Appl. Phys.* **115**, 17C704 (2014).
49) K. Yakushiji, K. Saito, S. Mitani, and K. Takanashi, Y. K. Takahashi, and K. Hono: *Appl. Phys. Lett.* **88**, 222504 (2006).
50) T. Mizuno, Y. Tsuchiya, T. Machita, S. Hara, D. Miyauchi, K. Shimazawa, T. Chou, K. Noguchi, and K. Tagami: *IEEE Trans. Magn.* **44**, 3584 (2008).
51) T. Furubayashi, K. Komada, T. Furubayashi, H. Sukegawa, Y. K. Takahashi, K. Inomata, and K. Hono: *Appl Phys. Lett.* **93**, 122507 (2008).
52) Y. Sakuraba, T. Iwase, K. Sato, S. Mitani and K. Takahashi: *Appl. Phys. Lett.* **94**, 012511 (2009).
53) T. Iwase, Y. Sakuraba, S. Bosu, K. Saito, S. Mitani, and K. Takanashi: *Appl. Phys. Exp.* **2**, 063003 (2009).
54) T. M. Nakatani, T. Furubayashi, S. Kasai, H. Sukegawa, Y. K. Takahashi, S. Mitani and K. Hono: *Appl. Phys. Lett.* **99**, 182505 (2011).
55) N. Hase, B. S. D. Ch. S. Varaprasad, T. M. Nakatani, H. Sukegawa, S. Kasai, Y. K. Takahashi, T. Furubayashi and K. Hono: *J. Appl. Phys.* **108**, 093916 (2010).
56) Y. Sakuraba, K. Izumi, T. Iwase, S. Bosu, K. Saito, K. Takanashi, Y. Miura, K. Futatsukawa, K. Abe, and M. Shirai: *Phys. Rev. B* **82**, 094444 (2010).
57) Y. K. Takahashi, A. Srinivasan, B. Varaprasad, A. Rajanikanth, N. Hase, T. M. Nakatani, S. Kasai, T. Furubayashi, and K. Hono: *Appl. Phys. Lett.* **98**, 152501 (2011).
58) M. J. Carey, S. Maat, S. Chandrashekariaih, J. A. Katine, W. Chen, B. York, and J. R. Childress: *J. Appl. Phys.* **109**, 093912 (2011).
59) J. Sato, M. Oogane, H. Naganuma and Y. Ando: *Appl. Phys. Exp.* **4**, 113005 (2011).
60) Y. Sakuraba, M. Ueda, Y. Miura, K. Sato, S. Bosu, K. Saito, M. Shirai, T. J. Konno and K. Takanashi: *Appl. Phys. Lett.* **101**, 252408 (2012).
61) S. Li, Y. K. Takahashi, T. Furubayashi and K. Hono: *Appl. Phys. Lett.* **103**, 042405 (2013).
62) J. W. Jung, Y. Sakuraba, T. T. Sasaki, Y. Miura and K. Hono: *Appl. Phys. Lett.* **108**, 102408 (2016).
63) M. Inoue, B. Hu, K. Moges, K. Inubushi, K. Nakada, M. Yamamoto and T. Uemura: *Appl. Phys. Lett.* **111**, 082403 (2017).
64) T. Kubota, Y. Ina, Z. Wen, H. Narisawa and K. Takanashi: *Phys. Rev. Mat.* **1**, 044402 (2017).
65) S. Li, T. Nakatani, K. Masuda, Y. Sakuraba, X. D. Xu, T. T. Sasaki, H. Tajiri, Y. Miura, T. Furubayashi and K. Hono: *Acta Materialia* **142**, 49 (2018).
66) T. Kubota, Y. Ina, Z. Wen and K. Takanashi: *J. Mag. Mag. Mat.* **474**, 365 (2019).
67) B. Büker, J. W. Jung, T. Sasaki, Y. Sakuraba, Y. Miura, T. Nakatani, A. Hütten and K. Hono: *Phys. Rev. B* **103**, L140405 (2021).
68) Y. Fujita, Y. Miura, T. Sasaki, T. Nakatani, K. Hono and Y. Sakuraba: *Phys. Rev. B* **104**, L140403 (2021).
69) J. P. Perdew, K. Burke, and M. Ernzerhof: *Phy. Rev. Lett.* **77**, 3865 (1996).
70) P. Giannozzi, S. Baroni, N. Bonini, M. Calandra, R. Car, C. Cavazzoni, D. Ceresoli, G. L. Chiarotti, M. Cococcioni, I. Dabo, A. Dal Corso, S. Fabris, G. Fratesi, S. de Gironcoli, R.

Gebauer, U. Gerstmann, C. Gougoussis, A. Kokalj, M. Lazzeri, L. Martin-Samos, N. Marzari, F. Mauri, R. Mazzarello, S. Paolini, A. Pasquarello, L. Paulatto, C. Sbraccia, S. Scandolo, G. Sclauzero, A. P. Seitsonen, A. Smogunov, P. Umari, R. M. Wentzcovitch: *J. Phys.: Condens. Matter* **21**, 395502 (2009).
71) R. Landauer: *Philos. Mag.* **21**, 863 (1970).
72) H. J. Choi and J. Ihm: *Phys. Rev. B* **59**, 2267 (1999).
73) A. Smogunov, A. Dal Corso, and E. Tosatti: *Phys. Rev. B* **70**, 045417 (2004).
74) Y. Miura, H. Uchida, Y. Oba, K. Abe and M. Shirai: *Phys. Rev. B* **78**, 064416 (2008).
75) Y. Miura, H. Uchida, Y. Oba, K. Nagao and M. Shirai: *J. Phys.: Condens. Matter* **19**, 365228 (2007).
76) P. Mavropoulos, M. Lezaic, and S. Blügel: *Phys. Rev. B* **72**, 174428 (2005).
77) M. Lezaic, P. Mavropoulos, J. Enkovaara, G. Bihlmayer and S. Blügel: *Phys. Rev. Lett.* **97**, 026404 (2006).
78) L. Chioncel, Y. Sakuraba, E. Arrigoni, M. I. Katsnelson, M. Oogane, Y. Ando, T. Miyazaki, E. Burzo, and A. I. Lichtenstein: *Phys. Rev. Lett.* **100**, 086402 (2008).
79) J. Kübler, K-H. Höck, J. Sticht and A. R.Williams: *J. Phys. F: Met. Phys.* **18**, 469 (1988).
80) K. Nakamura, T. Ito, A. J. Freeman, L. Zhong and J. Fernandez-de-Castro: *Phys. Rev. B* **67**, 014420 (2003).
81) Y. Miura, K. Abe and M. Shirai: *Phys. Rev. B* **83**, 214411 (2011).
82) J. Kübler, G. H. Fecher and C. Felser: *Phys. Rev B* **76**, 024414 (2007).
83) J. Kübler, A. R. Williams and C. B. Sommers: *Phys. Rev. B* **28**, 1745 (1983).
84) T. Saito, T. Katayama, T. Ishikawa, M. Yamamoto, D. Asakura, T. Koide, Y. Miura and M. Shirai: *Phys. Rev. B* **81**, 144417 (2010).
85) L. M. Sandratskii: *Phys. Rev. B* **78**, 094425 (2008).
86) M. Weinert, R. E. Watson and J. W. Davenport: *Phys. Rev. B* **32**, 2115 (1985).
87) G. H. O. Daalderop, P. J. Kelly and M. F. Schuurmans: *Phys. Rev. B* **41**, 11919 (1990).
88) S. Lounis and P. Dederichs: *Phys. Rev. B* **82**, 180404(R) (2010).
89) A. Sakuma, Y. Toga, and H. Tsuchiura: *J. Appl. Phys.* **105**, 07C910 (2009).
90) K. Masuda, T. Tadano and Y. Miura: *Phys. Rev. B* **104**, L180403 (2021).
91) T. Valet and A. Fert: *Phys. Rev. B* **48**, 7099 (1993).
92) Y. Miura, K. Futatsukawa, S. Nakajima, K. Abe and M. Shirai: *Phys. Rev. B* **84**, 134432 (2011).
93) A. Kokalj: *Comput. Mater. Sci.* **28**, 155 (2003).

Received Mar. 31, 2023; Accepted Apr. 19, 2023

J. Magn. Soc. Jpn., **47**, 103-107 (2023) <Paper>

Increase in coercivity of Sm(Fe-Co)-B thin films due to diffusion of Al element from cap layer

Y. Mori†, S. Hatanaka, M. Kambayashi, S. Nakatsuka*, K. Hirayama*, M. Doi, and T. Shima
Graduate School of Engineering, Tohoku Gakuin Univ., *1-13-1 Tagajo, 985-8537, Japan*
*Department of Engineering, Tohoku Gakuin Univ., *1-13-1 Tagajo, 985-8537, Japan*

The effects of Al diffusion and heat treatment on the structure and magnetic properties for Sm(Fe-Co)-B thin film have been investigated. In the X-ray diffraction patterns, peaks of (002) and (004) from $ThMn_{12}$-type compounds were clearly observed for all the samples. The coercivity $\mu_0 H_c$ was improved by introducing an Al cap layer and it was further increased by heat treatment. A high $\mu_0 H_c$ of 1.78 T was obtained at 400 ºC by increasing the annealing time to 4 hours. It was considered that infiltration of Al into the Sm(Fe-Co)-B layer contributed to the improvement of magnetic properties.

Keywords: coercivity, $ThMn_{12}$ compound, Sm(Fe-Co)-B film, grain boundary diffusion, Al cap layer

1. Introduction

RFe_{12} (R: Rare earth element) compounds with tetragonal $ThMn_{12}$-type crystal structure are expected to be new high-performance permanent magnetic materials because of their high saturation magnetization due to composition with high Fe content. Among these compounds, $SmFe_{12}$ based compounds exhibits high intrinsic magnetic properties[1)-7)]. For example, Hirayama et al. reported that high saturation magnetization ($\mu_0 M_s$ = 1.78 T), high anisotropy field ($\mu_0 H_A$ = 12 T) at room temperature and high Curie temperature (T_C = 879 K) were obtained in the $Sm(Fe_{0.8}Co_{0.2})_{12}$ epitaxial film with V buffer layer[2)], which were higher than those of $Nd_2Fe_{14}B$ sintered magnet, however obtained $\mu_0 H_c$ was less than 0.1 T. Since the RFe_{12} compounds are well known to exhibit thermo-dynamical instability in the bulk form, a method of substituting a part of Fe with stabilizing elements such as Al, Si, Ti, V, Co, W and Zr was used to control the microstructure, but as a result, a large decrease in saturation magnetization could not be avoided.

Recently, it was reported that a high $\mu_0 H_c$ above 1.1 T was successfully obtained for the $Sm(Fe_{0.8}Co_{0.2})_{12}B_{0.5}$ thin film[11)-12)]. From the result of the microstructural analysis, it was confirmed that the $SmFe_{12}$ (1:12) grains exhibiting a columnar structure were enveloped by a B-rich amorphous grain boundary (GB) phase consisting of 80 at.% of Fe and Co. Therefore, controlling the composition and increasing the number of pining sites in the GB phase play a very important role and will lead to further improvement of magnetic properties. The GB diffusion using non-magnetic elements is expected to improve magnetic properties, and many achievements have been made to improve magnetic properties [13)-16)]. Bolyachkin et al. reported that $\mu_0 H_c$ of $Sm(Fe_{0.8}Co_{0.2})_{12}B_{0.5}$ (100 nm) thin film was improved by Si diffusion into GB phase and based on the results of STEM-EDS observation, micromagnetic simulation was performed to predict the optimum microstructure. Then, it was confirmed that the Si deposited as the cap layer is diffused into the $Sm(Fe_{0.8}Co_{0.2})_{12}B_{0.5}$ layer by heat treatment. Most of the Si diffused into the GB phase was found to be in the region of about 25 nm from the top surface of the $Sm(Fe_{0.8}Co_{0.2})_{12}B_{0.5}$ layer. Therefore, according to the micromagnetic simulations, it was predicted that $\mu_0 H_c$ of 1.9 T will be obtained when the penetration depth of Si is 90 nm[15)]. Thus, increasing the region of non-magnetic elements diffused into the GB phase plays an important role for achieving large $\mu_0 H_c$. The optimum cap layer material for diffusing into grain boundary phase should be the one that forms a solid solution with Fe in the liquid phase at relatively low annealing temperature. In this study, in order to investigate the effect of Al diffusion and heat treatment on the crystal structure and magnetic properties for Sm(Fe-Co)-B thin film, different heat treatments have been performed to Sm(Fe-Co)-B (100 nm)/ Al (t_{Al} nm) thin films and their magnetic properties and crystal structures have been investigated.

2. Experimental procedure

The samples were prepared by using an ultra-high vacuum magnetron sputtering system with base

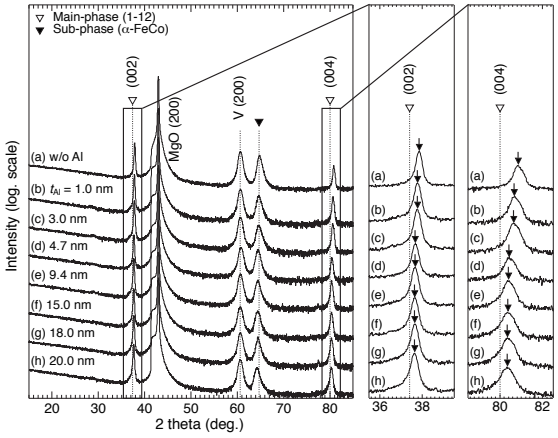

Fig. 1. XRD patterns for Sm(Fe-Co)-B/ Al thin films with different Al cap layer thicknesses between 0 (w/o Al) and 20 nm. Enlarged view of the (002) and (004) peaks from $ThMn_{12}$ phase are also shown.

Corresponding author: Y. Mori
(e-mail: mori.tohokugakuin.mml@gmail.com).

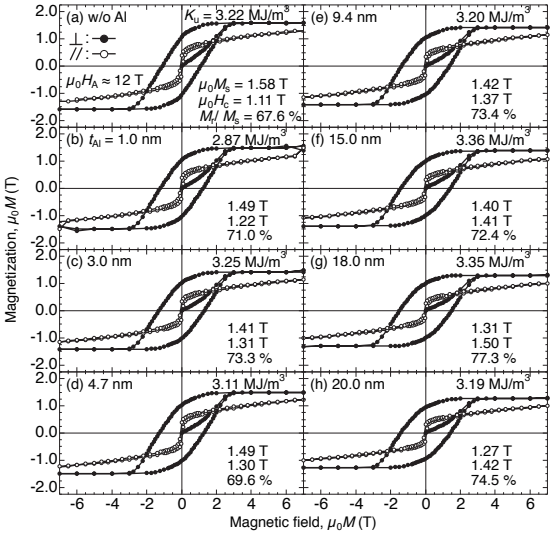

Fig. 2. Magnetization curves for Sm(Fe-Co)-B/ Al thin films with different Al layer thicknesses between 0 (w/o Al) and 20 nm.

pressure of less than 4.0 × 10^{-8} Pa. First of all, a V buffer layer of 20 nm was deposited onto MgO (100) single crystal substrate at substrate temperature T_s of 400 ºC. Then, the Sm(Fe-Co)-B layer of 100 nm was deposited at T_s of 400 ºC by co-sputtering with Fe, $Fe_{50}Co_{50}$, $Fe_{80}B_{20}$, and Sm targets. The composition of the film was determined to be $Sm_{7.3}Fe_{74.0}Co_{18.7}B_x$ (at.%) by Energy dispersive X-ray analysis (EDX). However, it is noted that due to the detection limit of light elements, the composition of B cannot be determined by EDX. Subsequently, an Al cap layer was deposited at T_s of 400 ºC onto Sm(Fe-Co)-B layer and the thickness t_{Al} was changed between 0 and 100 nm. Moreover, heat treatment was adjusted by annealing temperature T_a between 400 and 450 ºC and annealing time t_a from 0 to 5 hours. Finally, V layer of 10 nm was deposited as a protective layer for preventing of oxidation. The analysis of crystal structures was performed by X-ray diffraction (XRD) with Cu-K_α radiation from the out-of-plane configuration. The magnetic properties were evaluated by using a superconducting quantum interface device (SQUID) magnetometer. All measurements were performed at room temperature.

3. Results and discussion

X-ray diffraction patterns for Sm(Fe-Co)-B (100 nm)/ Al (t_{Al} nm) thin films with different Al cap layer thicknesses are shown in Fig. 1. The thickness of Al cap layer was changed in a range between 0 (w/o Al) and 20 nm. The enlarged view of the (002) and (004) peaks from $ThMn_{12}$ phase are also shown. The peaks from $ThMn_{12}$-type compound were clearly observed for all the films, and their position were shifted to lower angle with increasing the Al cap layer thickness up to 9.4 nm (e), showing that *c*-axis elongated by substituting a part of Fe-Co site with Al element which diffused into 1:12 phase in the Sm(Fe-Co)-B layer. No remarkable change in peak position of the 1:12 phase was observed above t_{Al} = 9.4 nm, and the intensity was almost the same, indicating that the *c*-axis elongation was saturated.

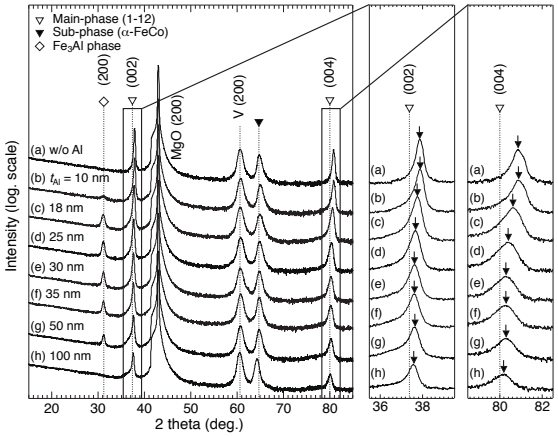

Fig. 3. XRD patterns of Sm(Fe-Co)-B/ Al thin films with different Al layer thicknesses between 0 (w/o Al) and 100 nm at annealing temperature of 450 ºC for 0.5 hours.

Magnetization curves for Sm(Fe-Co)-B (100 nm)/ Al (t_{Al} nm) thin films with different Al layer thicknesses are shown in Fig. 2. The filled circles and open ones are denoted the curves measured in the perpendicular and in the parallel directions to the film plane, respectively. The high $\mu_0 H_c$ of 1.11 T was obtained from the film without Al cap layer (a) and then it was increased with increasing the thickness of Al cap layer. The high $\mu_0 M_s$ of 1.31 T, high $\mu_0 H_c$ of 1.50 T, and moderate uniaxial magnetic anisotropy K_u of 3.35 MJ/m^3 were obtained for the film with t_{Al} of 18 nm (g). With further increase of t_{Al} to 20 nm, the $\mu_0 H_c$ was slightly decreased to 1.42 T (h). From these results, it was confirmed that the deposition of the Al layer was contributed to increase the coercivity of Sm(Fe-Co)-B thin films. The amount of Al diffused into the 1:12 phase is expected to increase since $\mu_0 M_s$ decreased above t_{Al} = 9.4 nm, which is thought to be due to the elongation of the *a*-axis, since the XRD results show no change in the *c*-axis.

In order to further improve the $\mu_0 H_c$, a heat treatment was adopted and the effect of Al cap layer thickness on the crystal structures for Sm(Fe-Co)-B thin film was investigated. XRD patterns of Sm(Fe-Co)-B (100 nm)/ Al (t_{Al} nm) thin films with different Al layer thicknesses at annealing temperature of 450 ºC for 0.5 hours are shown in Fig. 3. The thickness was changed between 0 (w/o Al) and 100 nm. The peaks of (002) and (004) from 1:12 phase were observed for all the films. The position of these peaks was shifted to lower angle with increasing t_{Al}. However, intensity of the peaks was slightly decreased with increasing t_{Al}. In addition, it was confirmed that the peak from 31.1º was determined to be from Fe_3Al (200), intensity of the peak was increased with increasing t_{Al} up to 35 nm (f) and then was decreased above 35 nm. Thus, formation of the Fe_3Al phase is observed with increasing the thickness of Al layer, but it was decreased above 50 nm, which is thought to be due to the decrease in the amount of Fe diffusing into the Al layer as the Al content increases.

Magnetization curves for Sm(Fe-Co)-B (100 nm)/ Al (t_{Al} nm) films with different Al cap layer thicknesses at annealing temperature of 450 ºC for 0.5 hours are shown in Fig. 4. The Al layer thickness was changed

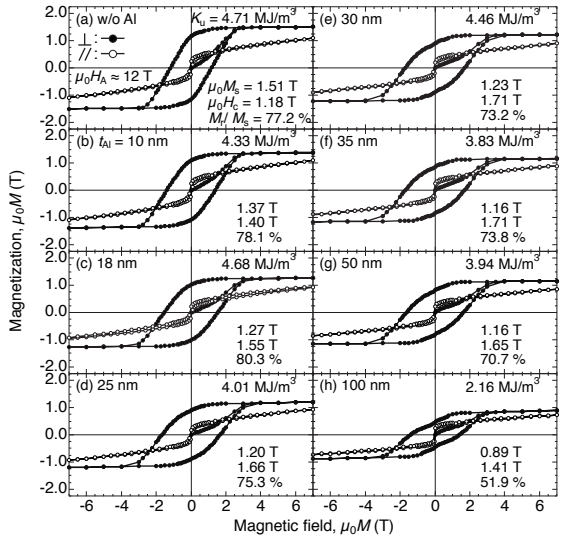

Fig. 4. Magnetization curves for Sm(Fe-Co)-B/ Al thin films with different Al cap layer thicknesses between 0 (w/o Al layer) and 100 nm at annealing temperature of 450 ºC for 0.5 hours.

between 0 (w/o Al) and 100 nm. The μ_0H_c of 1.18 T was obtained for the film without Al cap layer (a). Then, the μ_0H_c was increased with further increasing Al cap layer thickness and the high μ_0H_c of 1.71 T was obtained for the films with the thickness of Al cap layer of 30 (e) and 35 nm (f). Compared to the results of the optimum film thickness without heat treatment, the optimum thickness of Al layer was found to increase by addition of the heat treatment.

In order to sufficiently diffuse Al into the Sm(Fe-Co)-B layer, the optimum annealing temperature and annealing time must be determined. XRD patterns for Sm(Fe-Co)-B (100 nm)/ Al (35 nm) thin films with heat treatments at 450 ºC for t_a hours are shown in Fig. 5. The annealing time t_a was changed between 0 (w/o ann.) and 5 hours. The enlarged view of the (002) and (004) peaks from $ThMn_{12}$ phase are also shown. The position of these peaks was shifted to lower angle by increasing the annealing time from 0.5 (b) to 3.0 hours (d). Then, the peaks were shifted to higher angle when t_a was increased above 4.0 hours (e), indicating that the amount of Al element into the Sm(Fe-Co)-B layer was increased by increasing annealing time and in the case of extended heat treatment above 4.0 hours, *c*-axis was shrank. In addition, since intensity of the peak from Fe_3Al (200) was increased remarkably by increasing t_a and almost no change in the intensity was observed, it was considered that amount of Fe_3Al compound precipitation is increased by increase t_a.

Magnetization curves for Sm(Fe-Co)-B (100 nm)/ Al (35 nm) thin films with different annealing time are shown in Fig. 6. The large μ_0H_c of 1.71 T was obtained at t_a of 0.5 hours (b). However, the μ_0H_c was remarkably decreased with increasing t_a and it was decreased to 1.41 T above 4.0 hours (e). From this result, it was confirmed that the μ_0H_c takes a maximum value at annealing temperature of 450 ºC for a very short annealing time of 0.5 hours. Furthermore, since the Fe_3Al phase is known to be ferromagnetic[18], it is

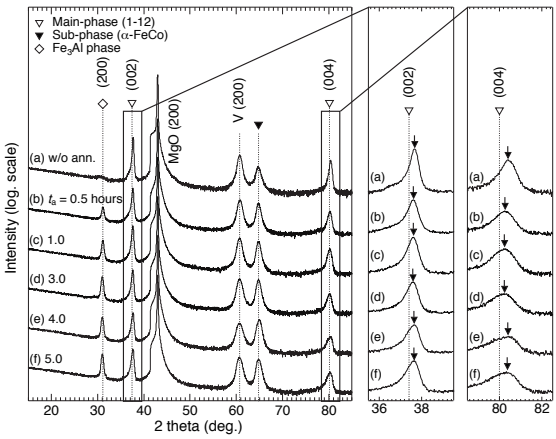

Fig. 5. XRD patterns for Sm(Fe-Co)-B (100 nm)/ Al (35 nm) thin films with annealing temperature of 450 ºC for t_a hours. Annealing time was changed between 0 (w/o ann.) and 5 hours.

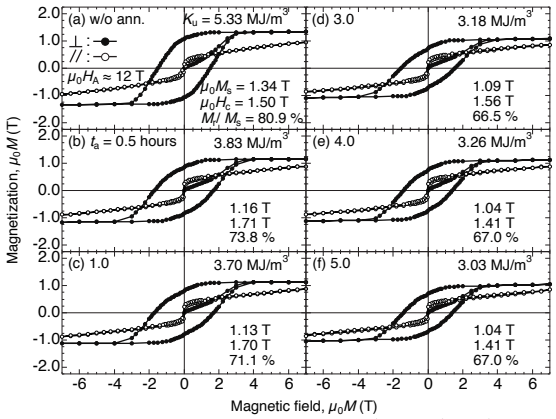

Fig. 6. Magnetization curves for Sm(Fe-Co)-B (100 nm)/ Al (35 nm) thin films with annealing temperature of 450 ºC for t_a hours. Annealing time was changed between 0 (w/o ann.) and 5 hours.

thought that μ_0H_c was decreased due to a magnetic coupling between 1:12 grains or nucleation of the reverse magnetic domain in the Fe_3Al phase which exists in the GB phase at the upper region of the Sm(Fe-Co)-B layer or at the interface between the Al layer and the Sm(Fe-Co)-B layer.

The annealing time was changed at low annealing temperature of 400 ºC to suppress the formation of Fe_3Al compound and promote the diffusion of Al into the Sm(Fe-Co)-B layer. XRD patterns of Sm(Fe-Co)-B (100 nm)/ Al (35 nm) thin films with different annealing time are shown in Fig. 7. The annealing time was changed between 0 (w/o ann.) and 5 hours, while annealing temperature was fixed at 400 ºC. The enlarged view of the (002) and (004) peaks from $ThMn_{12}$ phase are also shown. The peaks of (002) and (004) from 1:12 phase were observed for all the samples. When the annealing temperature was reduced to 400 ºC, the elongation of the *c*-axis did not depend on the duration of the annealing time, indicating that the amount of Al diffusion into 1:12 phase was decreased. Although, intensity of the peak from Fe_3Al phase increases by increasing annealing time, it was confirmed that formation of the Fe_3Al compound is suppressed

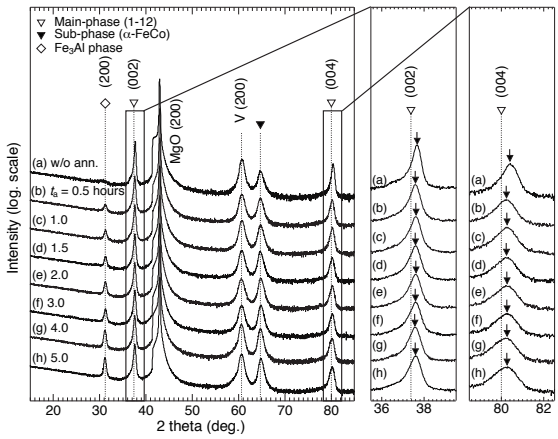

Fig. 7. XRD patterns of Sm(Fe-Co)-B (100 nm)/ Al (35 nm) thin films with annealing temperature of 400 °C for t_a hours. Annealing time was changed between 0 (w/o ann.) and 5 hours.

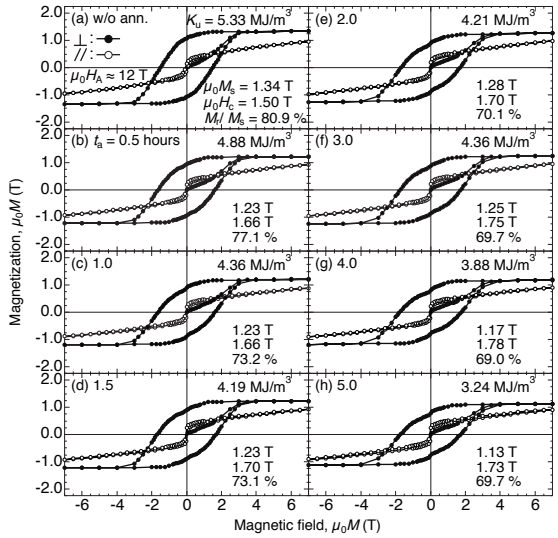

Fig. 8. Magnetization curves for Sm(Fe-Co)-B (100 nm)/ Al (35 nm) thin films with annealing temperature of 400 °C for t_a hours. Annealing time was changed between 0 (w/o ann.) and 5 hours.

compared to the case where the annealing temperature is 450 °C.

Magnetization curves of Sm(Fe-Co)-B (100 nm)/ Al (35 nm) thin films with different annealing time are shown in Fig. 8. Annealing time was changed between 0 (w/o ann.) and 5 hours and annealing temperature was fixed at 400 °C. The $\mu_0 H_c$ of 1.50 T was obtained for the film without heat treatment (a). However, with increasing t_a, the highest $\mu_0 H_c$ of 1.78 T, $\mu_0 M_s$ of 1.17 T and K_u of 3.88 MJ/m^3 were obtained for the film with annealing time of 4 hours (g). Further increase of t_a to 5 hours, the $\mu_0 H_c$ was slightly decreased to 1.73 T (h). It was confirmed that the heat treatment at 400 °C for 4 hours is found to be very effective to increase $\mu_0 H_c$ for Sm(Fe-Co)-B thin film with diffusion of Al. This increase in $\mu_0 H_c$ is considered to be due to the reduction of Al diffusion into the 1:12 phase and precipitation of the Fe_3Al phase, suggesting that Al element existing in the grain boundary phase is responsible for the high coercivity.

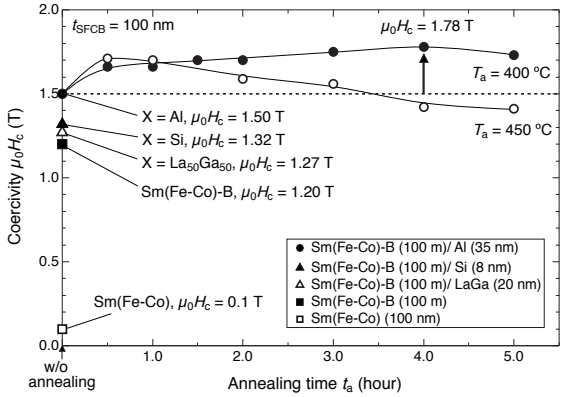

Fig. 9. Effect of annealing time on $\mu_0 H_c$ for Sm(Fe-Co)-B thin films. Closed circles and open ones are denoted the films with T_a = 400 °C and 450 °C, respectively. For comparison, $\mu_0 H_c$ of the film without B addition (□)[12] and Sm(Fe-Co)-B (■)[11], Sm(Fe-Co)-B/ $La_{50}Ga_{50}$ (△)[17] and Sm(Fe-Co)-B/ Si (▲)[16)-17)] thin films are plotted. Marks that overlap with the y-axis indicate the films without post annealing.

$\mu_0 H_c$ of Sm(Fe-Co)-B/ Al thin films as a function of annealing time are shown in Fig. 9. The filled circles and open ones are denoted the films with T_a = 400 °C and 450 °C, respectively. As comparison, $\mu_0 H_c$ of the film without B addition (□), Sm(Fe-Co)-B (■), Sm(Fe-Co)-B/ $La_{50}Ga_{50}$ (△) and Sm(Fe-Co)-B/ Si (▲) thin films are plotted. The $\mu_0 H_c$ was increased above 1.2 T by the diffusion of $La_{50}Ga_{50}$, Si, and Al into the Sm(Fe-Co)-B layer[16)-17)]. Among these materials, the highest $\mu_0 H_c$ of 1.5 T was obtained at the film with the diffusion of Al. Further enhancement of $\mu_0 H_c$ was obtained by appropriate heat treatment. When the annealing temperature was fixed at 450 °C, $\mu_0 H_c$ increased by the short annealing time of 0.5 hours, but it was decreased by longer heat treatment. In contrast, the highest $\mu_0 H_c$ of 1.78 T was obtained for longer annealing time of 4 hours at annealing temperature of 400 °C. It was considered that the diffusion of Al element into Sm(Fe-Co)-B layer is a very effective approach to increase the $\mu_0 H_c$ for Sm(Fe-Co)-B thin film.

4. Conclusion

The effect of Al cap layer deposition and different heat treatments on the crystal structures and magnetic properties for Sm(Fe-Co)-B thin films have been investigated. The peaks of (002) and (004) from $ThMn_{12}$-type compounds were observed and their position were shifted to lower angle with increasing the thickness of Al cap layer, indicating that Al element was diffused into Sm(Fe-Co)-B layer. In addition, $\mu_0 H_c$ of Sm(Fe-Co)-B thin film was increased with increasing the thickness of Al cap layer and the value of 1.50 T was obtained for Sm(Fe-Co)-B (100 nm)/ Al (18 nm) thin film. Although the $\mu_0 H_c$ of Sm(Fe-Co)-B (100 nm)/ Al (35 nm) thin film with annealing temperature of 450 °C was decreased with increasing annealing time, while at 400 °C, formation of the Fe_3Al compound and Al diffusion into 1:12 phase were thought to be suppressed and $\mu_0 H_c$ increased. As a result, the maximum $\mu_0 H_c$ of 1.78 T was

obtained in this study. Therefore, it was considered that the diffusion of Al element into Sm(Fe-Co)-B layer is a very effective approach to increase $\mu_0 H_c$ for Sm(Fe-Co)-B thin film, and it is believed that the result of diffusion/infiltration in the GB phase can pave the way to realize the application of $Sm(Fe\text{-}Co)_{12}$ based permanent magnet.

Acknowledgements This work was performed at the Research Institute for Engineering and Technology (High-Tech Research Center) at Tohoku Gakuin University. This work was partly supported by the Elements Strategy Initiative Center for Magnetic Materials (ESICMM) of National Institute for Materials Science (NIMS).

References

1) B. Fuquan, J. L. Wang, O. Tegus, W. Dagula, N. Tang, F. M. Yang, G. H. Wu, E. Brück, F. R. de Boer and K. H. J. Buschow: *J. Magn. Magn. Mater.,* **290**, 1192 (2005).
2) Y. Hirayama, Y. K. Takahashi, S. Hirosawa and K. Hono: *Scr. Mater.,* **138**, 62 (2017).
3) A. M. Gabay and G. C. Hadjipanayis: *Scr. Mater.,* **154**, 284 (2018).
4) P. Tozman, H. Sepehri-Amin, Y. K. Takahashi and K. Hono: *Acta Mater.,* **153**, 354 (2018).
5) P. Tozman, Y. K. Takahashi, H. Sepehri-Amin, D. Ogawa, S. Hirosawa and K. Hono: *Acta Mater.,* **178**, 114 (2019).
6) Y. K. Takahashi, H. Sepehri-Amin and T. Ohkubo: *Adv. Mater.,* **22** 449 (2021).
7) P. Tozman, H. Sepehri-Amin and K. Hono: *Scr. Mater.,* **194**, 113686 (2021).
8) X. C. Kou, T. S. Zhao, R. Grössinger, H. R. Kirchmayr, X. Li and F. R. de Boer: *Phys. Rev. B.,* **47**, 3231 (1993).
9) M. Artigas, C. Piquer, J. Rubin and J. Bartolome: *J. Magn. Magn. Mater.,* **196**, 653 (1999).
10) I. Dirba, J. Li, H. Sepehri-Amin, T. Ohkubo, T. Schrefl and K. Hono: *J. Alloys Compd.,* **804**, 155 (2019).
11) H. Sepehri-Amin, Y. Tamazawa, M. Kambayashi, G. Saito, Y. K. Takahashi and D. Ogawa, T. Ohkubo, S. Hirosawa, M. Doi, T. Shima, K. Hono: *Acta Mater.,* **194**, 337 (2020).
12) M. Kambayashi, H. Kato, Y. Mori, M. Doi and T. Shima: *J. Magn. Soc. Jpn.,* **45**, 66 (2021).
13) A. K. Srinithi, H. Sepehri-Amin, X. Tang, P. Tozman, J. Li, J. Zhang, S. Kobayashi, T. Ohkubo, T. Nakamura and K. Hono: *J. Magn. Magn. Mater.,* **529** 167866 (2021).
14) D. Ogawa, X. Xu, Y. K. Takahashi, T. Ohkubo, S. Hirosawa and K. Hono: *Scr. Mater.,* **164**, 140 (2019).
15) A. Bolyachkin, H. Sepehri-Amin, M. Kanbayashi, Y. Mori, T. Ohkubo, Y.K. Takahashi, T. Shima and K. Hono: *Acta Mater.,* **227**, 117716 (2022).
16) M. Kambayashi, H. Sepehri-Amin, Y. Mori, Y. K. Takahashi, T. Ohkubo, M. Doi, T. Shima and K. Hono: *170th JIM Spring Meeting*, online, S7.12 (2022).
17) M. Kambayashi, Y. Mori, S. Hatanaka, Y. Tamazawa, H. Kato, H. Sepehri-Amin, Y. K. Takahashi, T. Ohkubo, S. Hirosawa, T. Shima and K. Hono: *The CMSM-ESICMM Permanent Magnet Seminar* (2021).
18) A. Mulyawan, T. Terai and T. Fukuda: *J. Alloys Compd.,* **834**, 155 (2020).

Received Nov. 04, 2022; Revised Dec. 15, 2022; Accepted Mar. 19, 2023

J. Magn. Soc. Jpn., **47**, 108-114 (2023) <Paper>

Laser Induced Spin Current in GdFeCo/Cu/FeCo Trilayers Triggered by Ultrashort Pulsed Laser

K. Seguchi, E. Watanabe, D. Oshima, and T. Kato*

Department of Electronics, Nagoya Univ., *Furo-cho, Chikusa-ku, Nagoya 464-8603, Japan*

*Institute of Materials and Systems for Sustainability, Nagoya Univ., *Furo-cho, Chikusa-ku, Nagoya 464-8603, Japan*

The magnetization dynamics of GdFeCo / Cu / FeCo trilayers were studied by the time-resolved magneto-optical Kerr effect (TRMOKE) using an all-optical pump-probe technique. When the pump beam was illuminated from the FeCo layer side, the magnetization precession of the GdFeCo layer was confirmed to be enhanced compared with the case without the FeCo layer. Moreover, the precession angular frequency ω and inverse of the relaxation time $1/\tau$ of the GdFeCo layer were confirmed to be decreased by pumping the FeCo layer. The decreases in ω and $1/\tau$ were remarkable when the external field direction approached to the film normal. We considered spin transfer torque (STT) due to the spin current injected by triggering the precession of the FeCo layer, and we obtained a positive field-like STT and negative anti-damping STT acting on the GdFeCo layer. Moreover, the spin current J_s injected from the FeCo layer can be expected to be ~ 1 MA/cm^2 from the magnitude of the anti-damping STT.

Key words: magnetic recording, soft magnetic material, superconductor, magneto-optical recording, thin film

1. Introduction

The spin polarized current is known to exert torques (spin transfer torque: STT) that switches the magnetization of magnetic materials[1), 2)], and it is practically used as an efficient writing scheme in the magnetic random access memories (MRAMs). A pure spin current can also exert torques on magnetization[3)] and it can be generated by flowing the charge current in non-magnetic materials through the spin Hall effect[4), 5)]. This phenomenon is known as spin-orbit torque (SOT), and SOT switching has been extensively studied as a next-generation MRAM technology[6), 7)], since it is expected to be ten-times faster and ten times more energy efficient compared with STT switching[8)].

A pure spin current is also reported to be generated by pumping ferromagnetic thin films using an ultrashort pulsed laser. Ultrafast demagnetization of ferromagnets through the illumination of an ultrashort pulsed laser launches the spin current into the adjacent non-magnetic layer[9), 10)], which results in the precession and the switching of another ferromagnetic layer through the transfer of angular momentum between two ferromagnetic layers[11)–13)]. However, further study is necessary to understand spin currents launched and transferred by an ultrashort pulsed laser.

Here, we report the magnetization dynamics of GdFeCo / Cu / FeCo trilayers pumped by the ultrashort pulsed laser. The laser pulse excites the electrons in the FeCo layer and launches the spin current to the adjacent Cu layer. The spin current affects the magnetization precession of the ferrimagnetic GdFeCo layer, which is probed by the time resolved magneto-optical Kerr effect (TRMOKE). The GdFeCo amorphous alloy films are known to exhibit a perpendicular magnetic anisotropy, and Gd moments are antiferromagnetically coupled to FeCo moments. The net magnetization and net angular momentum of GdFeCo are known to be easily tuned by varying its composition[14), 15)]; thus, GdFeCo is an interesting material to discuss the relationship between the injected spin current and the angular momentum of the magnetic materials. We have studied STT[16)–18)] and SOT switching for GdFeCo[19)], and we reported an increase in the damping-like and field-like SOT effective fields near the compensation composition and the sign change of the field-like SOT effective field across the compensation composition[20)]. This report also studied the effective fields due to the spin current injection triggered by an ultrashort pulsed laser.

Corresponding author: T. Kato
(e-mail: kato.takeshi.i6@f.mail.nagoya-u.ac.jp).

2. Experiments

Samples with a stack of SiO_2 substrate / $Fe_{90}Co_{10}$(0 or 2 nm) / Cu(t_{Cu} nm) / $Gd_{21}(Fe_{90}Co_{10})_{79}$(10 nm) / SiN(5 nm) were prepared by an RF magnetron sputtering system, where the Cu thickness t_{Cu} was varied from 40 nm to 160 nm. The GdFeCo layer was deposited by co-sputtering of Gd and $Fe_{90}Co_{10}$ targets, and the SiN layer was deposited using an Si_3N_4 alloy target. Hysteresis loops were measured by an alternating gradient field magnetometer (AGM). The magnetic properties of GdFeCo and FeCo were checked by a magneto-optical Kerr spectrometer, where the light was incident from the GdFeCo or FeCo side. The magnetization dynamics of GdFeCo were monitored by TRMOKE using an ultrashort pulse fiber laser with a pulse width of 500 fs, a wavelength of λ = 1040 nm, and a repetition frequency of 100 kHz. As shown in Fig. 1 (a), a pump beam with λ = 1040 nm was incident from the substrate side, and a frequency doubled probe beam with λ = 520 nm was focused on the GdFeCo layer to monitor the precession after the pump beam

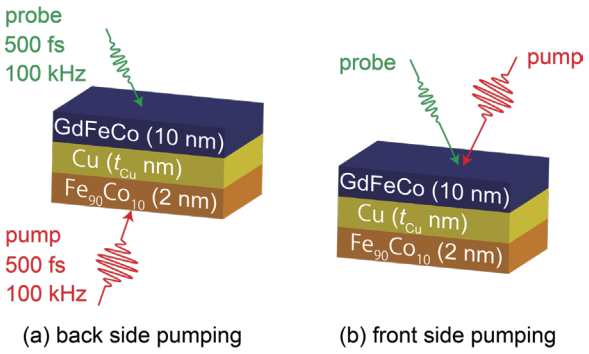

Fig. 1 Schematic of experiments. (a) Back side pumping illumination: the pump beam is illuminated from the substrate (FeCo) side. (b) Front side pumping: the pump and probe beams are illuminated on the same surface.

illumination. An external field H_{ext} of up to 5 kOe was applied in the direction of θ_H = 0–60° from the film normal. We refer to this TRMOKE setup as back side pumping. A standard all-optical pump-probe measurement shown in Fig. 1 (b) was also carried out to monitor the magnetization precession of the GdFeCo and FeCo layers. We refer to this setup as front side pumping, and an external magnetic field H_{ext} in the range of 4–14 kOe was applied in the direction of θ_H = 40–85° from the film normal for this case.

3. Results and Discussions

Figure 2 shows hysteresis loops of (a) GdFeCo / Cu (80) bilayer and (b) GdFeCo / Cu (80) / FeCo trilayer. The magnetic field was applied perpendicular (blue) and parallel (red) to the film plane. The vertical axis for the trilayer (Fig. 1 (b)) is shown in a magnetic moment per unit area $M \cdot d$, where M and d are the magnetization and total thickness of the magnetic layer, respectively. From Fig. 1 (a), the GdFeCo exhibited perpendicular magnetic anisotropy, whose magnetization was ~ 200 emu/cc and

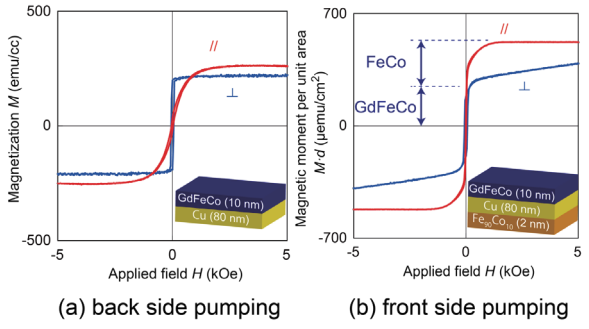

Fig. 2 Hysteresis loops of (a) GdFeCo / Cu (80) bilayer and (b) GdFeCo / Cu (80) / FeCo trilayer. Magnetic field was applied perpendicular (blue) and parallel (red) to the film plane. Magnetization of the (b) trilayer is shown per unit area.

anisotropy field was ~ 1 kOe. The estimated effective anisotropy and perpendicular anisotropies were 2 × 10^5 erg/cc and 5 × 10^5 erg/cc, respectively. As for the trilayer film, the hysteresis loops had two contributions: perpendicular magnetized GdFeCo and in-plane magnetized FeCo. The magnetizations per unit area of the GdFeCo and FeCo were estimated to be 200 μemu/cm² and 360 μemu/cm² by assuming the magnetizations of 200 emu/cc and 1800 emu/cc, respectively. The estimated magnetizations agreed well with the experimental loops shown in Fig. 1 (b), and the GdFeCo and FeCo layers are considered to be completely decoupled by a thick Cu layer.

Figure 3 shows TRMOKE waveforms of the GdFeCo / Cu (80) bilayer and GdFeCo / Cu (80) / FeCo trilayer, where the pump beam was illuminated from the substrate side (back side pumping). An external field H_{ext} of 5 kOe was applied along θ_H = 15° from the film normal. The pump power was 350 mW, which corresponds to a fluence of 4.4 mJ/cm², in order to trigger a significant precession of the FeCo layer with the pump beam (see Appendix). As shown in Fig. 3, the precession amplitude of the GdFeCo layer was confirmed to be enhanced by pumping the FeCo layer. Moreover, the precession frequency of the GdFeCo was reduced from 19 GHz to 16 GHz by inserting the FeCo layer, which will be discussed in detail later. This suggests that the spin current injected from the FeCo layer has an influence on the magnetization precession of the GdFeCo layer.

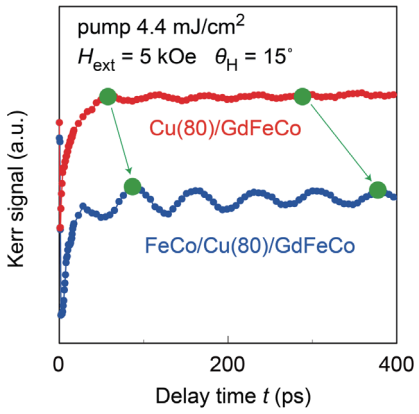

Fig. 3 TRMOKE waveforms of GdFeCo / Cu (80) bilayer and GdFeCo / Cu (80) / FeCo trilayer, where the pump beam was illuminated from the substrate side (back side pumping).

Figure 4 shows the Cu thickness dependence of the precession amplitude of GdFeCo estimated from TRMOKE waveforms of the GdFeCo / Cu (t_{Cu}) bilayer and GdFeCo / Cu (t_{Cu}) / FeCo trilayer for back side pumping. As shown in Fig. 4, the GdFeCo of the trilayer exhibited a larger precession amplitude than the GdFeCo of the bilayer. When the Cu thickness t_{Cu} was no less than 80 nm, the precession amplitude of the GdFeCo / Cu bilayer

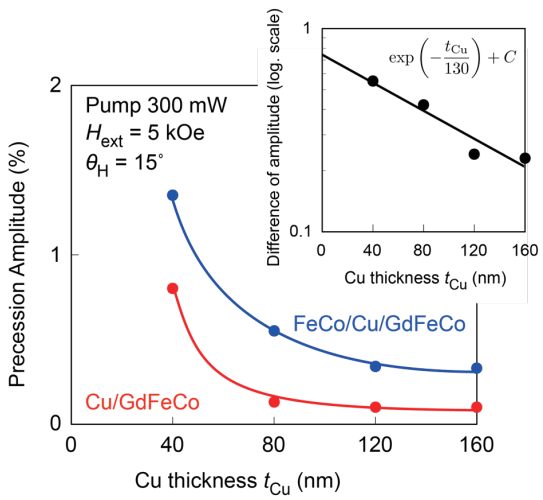

Fig. 4 Cu thickness dependence of precession amplitude of GdFeCo estimated from TRMOKE waveforms of GdFeCo / Cu (t_{Cu}) bilayer and GdFeCo / Cu (t_{Cu}) / FeCo trilayer for back side pumping. Inset shows log-normal plot of the t_{Cu} dependence of the difference in precession amplitude between GdFeCo / Cu / FeCo trilayer and GdFeCo / Cu bilayer.

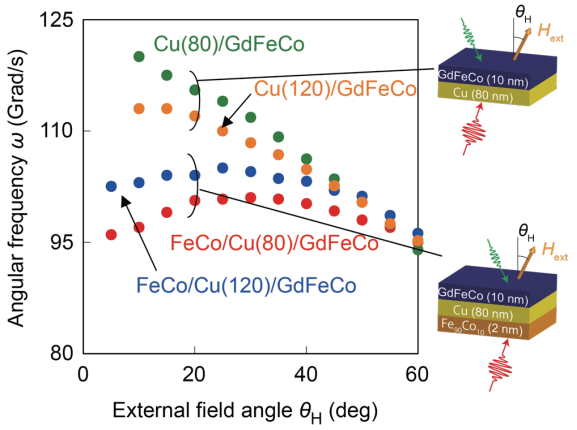

Fig. 5 External field angle θ_H dependence of the precession angular frequency ω of the GdFeCo layer for the samples of GdFeCo / Cu (80, 120) / FeCo trilayers and GdFeCo / Cu (80, 120) bilayers. External field H_{ext} was 5 kOe and the pump beam of 120 mW was irradiated from the back side as in the schematic illustrations.

became quite small due to the low transparency through the thick Cu layer. In the inset of Fig. 4, we plot t_{Cu} dependence of the difference in the precession amplitude of the GdFeCo between the trilayers and bilayers on a log-normal plot. From the slope of the inset, the spin diffusion length of the Cu layer was estimated to be λ = 130 nm, which is smaller than the values in previous reports[10), 21), 22)]. However, the spin diffusion length of Cu is sensitive to the crystal disorder of the Cu layer[22)]. The Cu layer in this study was grown on bcc FeCo (2 nm), which may induce the crystal disorder in the Cu layer compared with a Cu layer grown on the film with an fcc structure[10)].

Figure 5 shows the dependence of the precession angular frequency ω of the GdFeCo layer on the external field angle θ_H measured for the samples of the GdFeCo / Cu (80, 120) / FeCo trilayers and GdFeCo / Cu (80, 120) bilayers. The external field H_{ext} was 5 kOe and a pump beam with a power of 120 mW was illuminated as in Fig. 1 (a) (back side pumping). Here, we do not use the data for Cu (160 nm), since the perpendicular anisotropy of the GdFeCo was significantly reduced (not shown here) by depositing GdFeCo on a thick Cu (160 nm) layer. For the GdFeCo / Cu bilayers, the precession angular frequency ω increased as θ_H decreased, which is typical for the magnetic materials with perpendicular anisotropy. The effective anisotropy fields H_{keff} estimated from the θ_H dependence of ω were 1.3 and 0.95 kOe for the GdFeCo / Cu (80) and GdFeCo / Cu (120) bilayers, respectively. and these values roughly agreed with H_{keff} estimated from the corresponding hysteresis loops (see Fig. 2 (a) for the GdFeCo / Cu (80) bilayer). On the other hand, for the GdFeCo / Cu / FeCo trilayers, the precession angular frequency ω of GdFeCo increased when θ_H decreased from 60° to 30° and then decreased when θ_H decreased from 30° to 0°. This trend was remarkable for the trilayer with a thinner Cu layer. The reduction in ω at a small θ_H was disappeared, when a thin Pt (4 nm) layer was inserted in the Cu layer (see Appendix). This suggests the existence of a spin transfer torque due to the spin current injected from the FeCo layer by the back side pumping of the GdFeCo / Cu / FeCo trilayers. One possible origin of the spin current is the precession of the FeCo layer triggered by ultrashort pulsed laser. The precession of FeCo was confirmed to be increased by increasing the pump fluence and external field angle θ_H (see Appendix).

From the TRMOKE waveforms, the inverse of the relaxation time $1/\tau$ of the precession of GdFeCo was estimated together with the angular frequency ω (see Eq. (A1)). Figure 6 shows the θ_H dependence of $1/\tau$ of GdFeCo precessions estimated for the samples of the GdFeCo / Cu (80, 120) / FeCo trilayers and GdFeCo / Cu (80, 120) bilayers. The inverse of the relaxation time $1/\tau$ is known to be proportional when the extrinsic contributions, such the anisotropy distribution and two magnon scattering[23), 24)], are ignored, and it is expressed as,

$$1/\tau = \alpha_{eff}\omega, \qquad (1)$$

where α_{eff} is the effective Gilbert damping. As shown in Fig. 6, the $1/\tau$ for the GdFeCo / Cu (80, 120) bilayers gradually increased as θ_H decreased, which roughly agreed with the proportional relation between $1/\tau$ and ω in Eq. (1). From Eq. (1), the effective damping α_{eff} of $Gd_{21}(Fe_{90}Co_{10})_{79}$ was estimated to be 0.03–0.04, which is slightly larger than our previous report[14)], which is

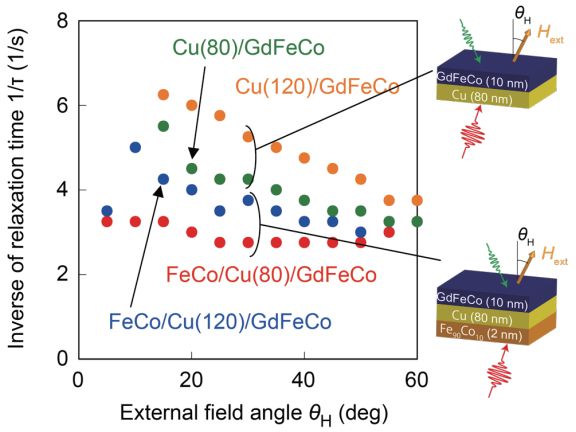

Fig. 6 External field angle θ_H dependence of the inverse of relaxation time $1/\tau$ of the GdFeCo layer for the samples of GdFeCo / Cu (80, 120) / FeCo trilayers and GdFeCo / Cu (80, 120) bilayers. The external field H_{ext} was 5 kOe and the pump beam of 120 mW was irradiated from the back side as in the schematic illustrations.

probably due to the anisotropy distribution of the GdFeCo grown on the Cu layer. For the samples of the GdFeCo / Cu (80, 120) / FeCo trilayers, a significant reduction in $1/\tau$ was confirmed compared with those for the GdFeCo / Cu (80, 120) bilayers. For instance, $1/\tau \sim 4.5$ GHz around $\theta_H \sim 20^\circ$ for the GdFeCo / Cu (80) bilayer significantly reduced to $1/\tau \sim 3$ GHz for the GdFeCo / Cu (80) / FeCo trilayer (~30% reduction), while ω reduced from 115 Grad/s to 105 Grad/s (only ~10% reduction) as shown in Fig. 5. This suggests a reduction in the effective damping α_{eff} due to the spin current injected from the FeCo layer by the back side pumping of the GdFeCo / Cu / FeCo trilayers.

In order to discuss the variation in the magnetization dynamics of GdFeCo between the GdFeCo / Cu / FeCo trilayers and GdFeCo / Cu bilayers, we consider the spin transfer torque due to the spin current injected by triggering the precession of the FeCo layer. The divergence of the spin current $\boldsymbol{J}_s$ is expressed by two components, field-like and anti-damping terms, as follows[25],

$$\frac{1}{e}\mathrm{div}\boldsymbol{J}_s = g_\perp \boldsymbol{s}\times\boldsymbol{p} + g_{//}\frac{\boldsymbol{s}}{|\boldsymbol{s}|}\times(\boldsymbol{s}\times\boldsymbol{p}), \qquad (2)$$

where e, $\boldsymbol{s}$, and $\boldsymbol{p}$ are an electron charge, a local spin vector per unit volume, and the spin direction of the spin current. $g_\perp$ and $g_{//}$ are the coefficients of the field-like and anti-damping terms. By adding the spin current contribution (Eq. (2)) to the following Landau–Lifshitz–Gilbert equation,

$$\dot{\boldsymbol{s}} = -\gamma \boldsymbol{s}\times\boldsymbol{H}_{\mathrm{eff}} - \alpha_{\mathrm{eff}}\frac{\boldsymbol{s}}{|\boldsymbol{s}|}\times\dot{\boldsymbol{s}}, \qquad (3)$$

we have a differential equation for the magnetization dynamics under the injection of the spin current as,

$$\dot{\boldsymbol{s}} = -\gamma\left(1-\frac{g_\perp}{\gamma H_{\mathrm{eff}}}\right)\boldsymbol{s}\times\boldsymbol{H}_{\mathrm{eff}} - \alpha_{\mathrm{eff}}\left(1+\frac{g_{//}}{\alpha_{\mathrm{eff}}\gamma H_{\mathrm{eff}}}\right)\frac{\boldsymbol{s}}{|\boldsymbol{s}|}\times\dot{\boldsymbol{s}}, \qquad (4)$$

where γ and $\boldsymbol{H}_{\mathrm{eff}}$ are a gyromagnetic ratio and an effective field vector of GdFeCo layer. Here, we simply assumed that $\boldsymbol{p}$ is parallel to $\boldsymbol{H}_{\mathrm{eff}}$ and also that the damping term is much smaller than the precession term in Eq. (3). We note that $\boldsymbol{p}$ is actually not parallel to $\boldsymbol{H}_{\mathrm{eff}}$; however, the component perpendicular to $\boldsymbol{H}_{\mathrm{eff}}$ has a smaller effect on the precession frequency.

From the precession angular frequency for the GdFeCo / Cu bilayers in Fig. 5, γH_{eff} was roughly estimated to be 115 Grad/s around $\theta_H \sim 20^\circ$. The precession angular frequency reduced to ~100 Grad/s and ~104 Grad/s for the GdFeCo / Cu (80) / FeCo and GdFeCo / Cu (120) / FeCo trilayers, respectively. Thus, we can simply get $g_\perp = 1.5 \times 10^{10}$ s^{-1} and 1.1×10^{10} s^{-1} for the trilayers with $t_{Cu} = 80$ and 120 nm, respectively. Similarly, from the reduction of $1/\tau$ in the trilayers as shown in Fig. 6, we can roughly obtain $g_{//} \sim -10^9$ s^{-1} for both trilayers. One may note that the different sign between $g_\perp$ and $g_{//}$. This is consistent with the results for the SOT of the GdFeCo / Ta bilayers, where the sign of the field-like SOT changes across the magnetization compensation point and $Gd_{21}(Fe_{90}Co_{10})_{79}$ exhibits a negative damping-like SOT and positive field-like SOT[20]. However, in the previous study, the field-like SOT was reported to be much smaller than the damping-like SOT, although the field-like $g_\perp$ is roughly 10 times larger than the anti-damping $g_{//}$ in this study. The temperature increase of the GdFeCo layer due to the pump illumination is ruled out in describing the large field-like $g_\perp$, since the GdFeCo / Cu bilayers (see Fig. 5) and GdFeCo / Cu / Pt / Cu /FeCo (see Appendix) did not show a decrease in the precession frequency. The reason for the large field-like $g_\perp$ is partly due to the variation of the effective anisotropy in GdFeCo between bilayer and trilayer as described in Appendix, however more detailed study will be necessary to discuss the effects on superdiffusive spin currents due to hot electrons[26] and spin currents due to spin Seebeck effect[10), 12]. Also, the time dependent spin current should be considered for the detailed analysis[10), 12]. The superdiffusive spin current, spin current due to spin Seebeck effect, and ultrafast demagnetization of FeCo are considered to relax in picosecond time scale, however, such pulse spin currents may induce the precession of GdFeCo in nanosecond timescale[12]. As described in Eq. (2), the decayed precession of FeCo (see Apendix) will generate constant spin current in nanosecond time scale. The origin of the spin current for the precession of GdFeCo will be studied in future work. Finally, we discuss the magnitude of J_s from the anti-damping $|g_{//}| \sim 10^9$ s^{-1}. If we assume that the net spin angular momentum per atom S and atoms per unit volume N of GdFeCo are $S = 0.1$ and $N = 6 \times 10^{22}$ cm^{-3} [27], respectively, the magnitude of local spin vector $\boldsymbol{s}$

in Eq. (2) is calculated to be $|\boldsymbol{s}| = SN = 6 \times 10^{21}$ cm^{-3}. Thus, J_s is estimated to be $J_s = eg_{//}|\boldsymbol{s}|t_{GdFeCo} \sim 1$ MA/cm^2 from Eq. (2), which will be sufficient enough to induce the precession of the GdFeCo(t_{GdFeCo} = 10 nm) layer. Thus, it is concluded that a large J_s of ~ 1 MA/cm^2 is injected from the FeCo layer triggered by ultrashort pulsed laser.

4. Summary

The magnetization dynamics of GdFeCo / Cu / FeCo trilayers after pumping the FeCo side with an ultrashort pulsed laser were studied and the results were compared with those of GdFeCo / Cu bilayers. The magnetic properties of the GdFeCo / Cu / FeCo trilayers showed that the GdFeCo layer exhibits perpendicular anisotropy, and the GdFeCo and FeCo layers are considered to be decoupled by a thick Cu layer. The precession amplitude of the GdFeCo layer was confirmed to be enhanced by pumping the FeCo layer, and the amplitude decreased as the intermediate Cu thickness increased. The precession frequency and inverse of the relaxation time of the GdFeCo layer were confirmed to be decreased by pumping the FeCo layer. The decreases in the precession frequency and inverse of the relaxation time were remarkable when the external field angle θ_H from the film normal was reduced. We considered spin transfer torque due to the spin current injected by triggering the precession of the FeCo layer to understand the the magnetization dynamics of the GdFeCo / Cu / FeCo trilayers. Positive field-like and negative anti-damping torques due to the injection of the spin current were obtained, which is consistent with the results for the SOT of GdFeCo / Ta bilayers. From the magnitude of the anti-damping torque ($|g_{//}| \sim 10^9$ s^{-1}), the spin current J_s injected from the FeCo layer can be expected to be ~ 1 MA/cm^2. However, 10 times larger field-like torque than the anti-damping torque was obtained, and further study will be necessary to understand the magnetization dynamics of GdFeCo / Cu / FeCo triggered by an ultrashort pulsed laser.

Appendix

Effect of insertion of thin Pt in Cu layer

Figure A1 shows the external field angle θ_H dependence of the precession angular frequency ω of the GdFeCo layer for the samples of GdFeCo / Cu (120), GdFeCo / Cu (120) / FeCo, and GdFeCo / Cu (58) / Pt(4) / Cu (58). An external field H_{ext} was 5 kOe and a pump beam of 120 mW was irradiated from the back side as in Fig. 1 (a). The angular frequency ω for the GdFeCo / Cu bilayer monotonically increased as θ_H decreased, while ω for the GdFeCo / Cu / FeCo trilayer exhibited a maximum near $\theta_H \sim 30$ deg as discussed in Fig. 5. When a thin Pt (4 nm) layer was inserted in Cu layer, the reduction of ω at small θ_H disappeared as shown in Fig. A1. This suggests that the spin current produced by pumping the FeCo layer was blocked by thin Pt layer, since Pt exhibits much shorter spin diffusion length than Cu.

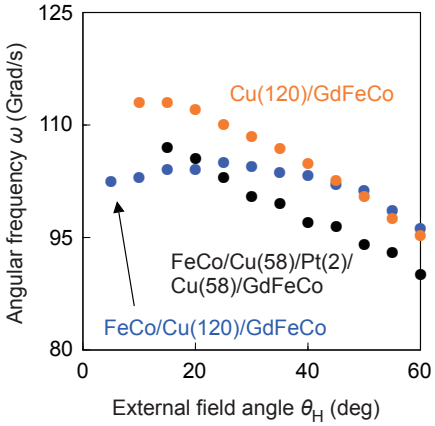

Fig. A1 External field angle θ_H dependence of the precession angular frequency ω of the GdFeCo layer for the samples of GdFeCo / Cu (120), GdFeCo / Cu (120) / FeCo, and GdFeCo / Cu (58) / Pt(4) / Cu (58) / FeCo. The external field H_{ext} was 5 kOe and the pump beam of 120 mW was irradiated from the back side as in Fig. 1 (a).

Magnetization dynamics of GdFeCo in trilayers

The magnetization dynamics of the GdFeCo in GdFeCo / Cu / FeCo trilayers were confirmed by front side pumping as shown in Fig. 1 (b). For the front side pumping setup, the applied field angle can be varied θ_H = 40–85° from the film normal direction. Thus, we have measured ω of the GdFeCo under the applied field H_{ext} of 4–14 kOe along $\theta_H = 40^\circ$. The H_{ext} dependence of ω was fitted with Shul's equation[28], and the detail of the fitting was described in our previous paper[29]. Table A1 summarizes H_{keff} and g-factor of the GdFeCo for GdFeCo / Cu / FeCo trilayers. Moreover, from the θ_H dependence of ω of the GdFeCo / Cu bilayers shown in Fig. 5, H_{keff} and g-factor of the GdFeCo in GdFeCo / Cu bilayers were estimated, which were also listed in Table A1. In Table A1, the ω values under the condition $\theta_H = 0$ were also listed, which were estimated using the following equation,

$$\omega = g\frac{\mu_0 e}{2m_e}(H_{ext} + H_{keff}), \quad \text{(A1)}$$

where μ_0, e, m_e are the permeability of vacuum, electron

Table A1 g-factor, H_{keff} and ω at $\theta_H = 0^\circ$ of GdFeCo in GdFeCo/Cu bilayers and GdFeCo / Cu / FeCo trilayers.

Sample	g-factor	H_{keff} (Oe)	ω at $\theta_H = 0^\circ$ (Grad/s)
GdFeCo/Cu(80)	2.15	1300	120
GdFeCo/Cu(120)	2.18	950	114
GdFeCo/Cu(80)/FeCo	2.18	500	106
GdFeCo/Cu(120)/FeCo	2.25	700	113

charge, and electron mass, respectively. An external field was H_{ext} = 5 kOe. As in Table A1, due to the deviation in H_{keff} of the GdFeCo among 4 samples, the ω values at θ_H = 0 deg were slightly distributed from 106 to 120 Grad/s. However, the reduction of ω at small θ_H as discussed in Fig. 5 is not explained by the variation of the perpendicular anisotropy of the GdFeCo.

Magnetization precession of FeCo layer

The magnetization precession of the FeCo layer of GdFeCo / Cu (80) / FeCo was monitored by TRMOKE, where the pump and probe beams were irradiated from the substrate side (front side pumping). Figure A2 shows the typical magnetization precession of the FeCo for a pump fluence of 3.8 mJ/cm^2, which corresponds to a pump power of 300 mW. An external field of 7 kOe was applied along 40° from the film normal. Clear damped precession was confirmed, and the waveform was fitted with the function,

$$f(t) = A\exp(-t/\tau)\sin(\omega t - \phi_0) + B\exp(-t/\tau_0) + C, \quad \text{(A1)}$$

where the ω and τ are the angular frequency and decay of the FeCo precession, respectively, and τ_0 is the decay of the recovery of the FeCo magnetization after the laser induced demagnetization at t = 0. The coefficients A, B, and C are fitting parameters, representing the amplitude of FeCo precession, intensity of laser induced demagnetization, and DC bias of the TRMOKE waveform, respectively. Figure A3 shows the dependence of the precession amplitude A on the pump power (pump fluence). The precession amplitude of FeCo became obvious when the pump power was more than 100 mW, corresponding to a fluence of 1.25 mJ/cm^2.

Figure A4 shows the dependence of the precession amplitude of FeCo on the direction of the external field

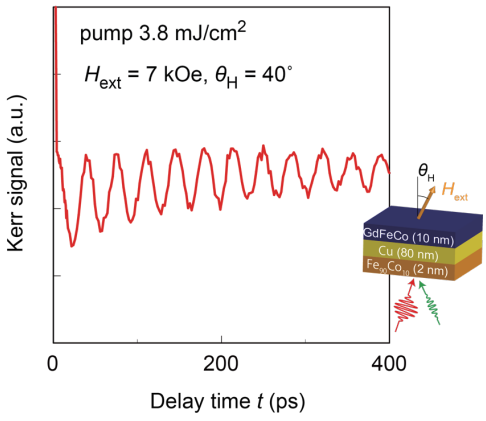

Fig. A2 TRMOKE waveforms of FeCo layer of GdFeCo / Cu (80) / FeCo trilayer, where the pump beam was illuminated from the substrate side as in the schematic illustrations. External field of 7 kOe was applied θ_H = 40° from the film normal.

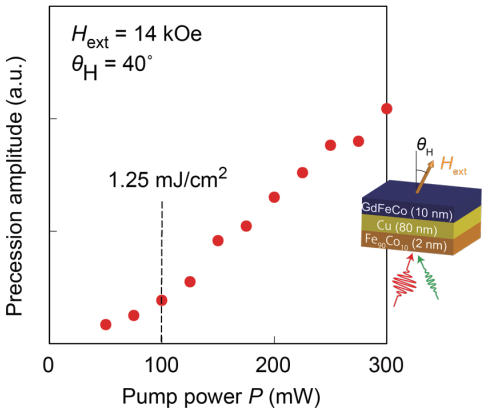

Fig. A3 Pump power dependence of the precession amplitude of the FeCo layer for the samples of GdFeCo / Cu (80) / FeCo trilayers, where the pump beam was illuminated from the substrate side as in the schematic illustrations. External field of 14 kOe was applied θ_H = 40° from the film normal.

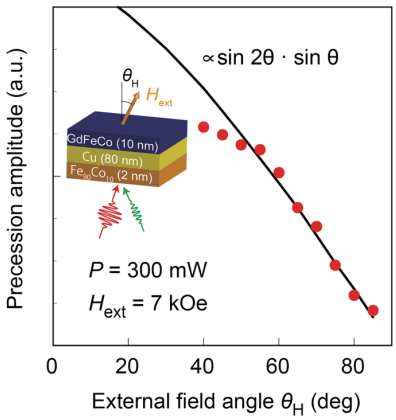

Fig. A4 External field angle θ_H dependence of the precession amplitude of the FeCo layer for the samples of GdFeCo / Cu (80) / FeCo trilayers, where the pump beam was illuminated from the substrate side as in the schematic illustrations. Pump power was 300 mW and the external field of 7 kOe was applied.

θ_H from the film normal. From Fig. A4, the amplitude decreased as θ_H increased, since the stable angle θ of FeCo moments from the film normal, which is determined by the competition between demagnetizing field and external field, increases with increasing θ_H. In Fig. A4, a curve fitted with a function of $D\sin2\theta\cdot\sin\theta$, which is proportional to the amplitude of magnetization precession of the FeCo moment[30], is also shown. It is confirmed that the dependence of the precession amplitude A on the direction of the external field θ_H is roughly fitted with the function of $D\sin2\theta\cdot\sin\theta$.

Acknowledgements The authors would like to thank Mr. M. Kumazawa, Nagoya University for the assistance in the experiments. This work was supported in part by JSPS KAKENHI Grant Number of 17K19068 and 20H02182. This work was also supported in part by the Project of Creation of Life Innovation Materials for Interdisciplinary and International Researcher Development of the Ministry of Education, Culture, Sports, Science and Technology (MEXT), Japan. A part of this work was performed under the Research Program of "Dynamic Alliance for Open Innovation Bridging Human, Environment and Materials" in "Network Joint Research Center for Materials and Devices." A part of this work was conducted at the Next-generation biomaterials Hub, Nagoya University, supported by "Advanced Research Infrastructure for Materials and Nanotechnology in Japan" of MEXT, Japan.

References

1) J. C. Slonczewski: *J. Magn. Magn. Mater.*, **159**, L1 (1996).
2) L. Berger: *Phys. Rev. B*, **54**, 9353 (1996).
3) J. Shi, P. Zhang, D. Xiao, and Q. Niu: *Phys. Rev. Lett.*, **96**, 076604 (2006).
4) Y. K. Kato, R. C. Myers, A. C. Gossard, and D. D. Awschalom: *Science*, **306**, 1910 (2004).
5) J. Sinova, S. O. Valenzuela, J. Wunderlich, C. H. Back, and T. Jungwirth: *Rev. Mod. Phys.*, **87**, 1213 (2015).
6) L. Liu, C. -F. Pai, Y. Li, H. W. Tseng, D. C. Ralph, and R. A. Buhrman: *Science*, **336**, 555 (2012).
7) L. Liu, O. J. Lee, T. J. Gudmundsen, D. C. Ralph, and R. A. Buhrman: *Phys. Rev. Lett.*, **109**, 096602 (2012).
8) X. Han, X. Wang, C. Wan, G. Yu, and X. Lv: *Appl. Phys. Lett.*, **118**, 189902 (2021).
9) T. Kampfrath, M. Battiato, P. Maldonado, G. Eilers, J. Nötzold, S. Mährlein, V. Zbarsky, F. Freimuth, Y. Mokrousov, S. Blügel, M. Wolf, I. Radu, P. M. Oppeneer, and M. Münzenberg: *Nat. Nanotech.*, **8**, 256 (2013).
10) G. -M. Choi, B. -C. Min, K. -J. Lee, and D. G. Cahill: *Nat. Commun.*, **5**, 4334 (2014).
11) A. J. Schellekens, K. C. Kuiper, R. R. J. C. de Wit, and B. Koopmans: *Nat. Commun.*, **5**, 5333 (2014).
12) J. Kimling and D. G. Cahill: *Phys. Rev. B*, **95**, 014402 (2017).
13) S. Iihama, Y. Xu, M. Deb, G. Malinowski, M. Hehn, J. Gorchon, E. E. Fullerton, and S. Mangin: *Adv. Mater.*, **30**, 1804004 (2018).
14) T. Kato, K. Nakazawa, R. Komiya, N. Nishizawa, S. Tsunashima, and S. Iwata: *IEEE. Trans. Magn.*, **44**, 3380 (2008).
15) K. -J. Kim, S. K. Kim, Y. Hirata, S. -H. Oh, T. Tono, D. -H. Kim, T. Okuno, W. S. Ham, S. Kim, G. Go, Y. Tserkovnyak A. Tsukamoto, T. Moriyama, K. -J. Lee, and T. Ono: *Nat. Mater.*, **16**, 1187 (2017).
16) B. Dai, T. Kato, S. Iwata, and S. Tsunashima: *IEEE Trans. Magn.*, **48**, 3223 (2012).
17) B. Dai, T. Kato, S. Iwata, and S. Tsunashima: *IEEE Trans. Magn.*, **49**, 4359 (2013).
18) B. Dai, Y. Guo, J. Zhu, T. Kato, S. Iwata, S. Tsunashima, L. Yang, and J. Han: *J. Phys. D Appl. Phys.*, **50**, 135005 (2017).
19) N. Roschewsky, T. Matsumura, S. Cheema, F. Hellman, T. Kato, S. Iwata, and S. Salahuddin: *Appl. Phys. Lett.*, **109**, 112403 (2016).
20) K. Kawakami, T. Kato, D. Oshima, and S. Iwata: *Jpn. J. Appl. Phys.*, **59**, SEEF01 (2020).
21) F. J. Jedema, A. T. Filip, and B. J. van Wees: *Nature*, **410**, 345 (2001).
22) K. P. McKenna and G. J. Morgan: *Eur. Phys. J. B*, **59**, 451 (2007).
23) J.-M. Beaujour, D. Ravelosona, I. Tudosa, E. E. Fullerton, and A. D. Kent: *Phys. Rev. B*, **80**, 180415(R) (2009).
24) A. Sakoguchi, D. Oshima, S. Iwata, and T. Kato: *IEEE Trans. Magn.*, **58**, 4200105 (2022).
25) D. M. Edwards, F. Federici, J/ Mathon, and A. Umerski: *Phys. Rev. B*, **71**, 054407 (2005).
26) M. Battiato, K. Carva, and P. M. Oppeneer: *Phys. Rev. Lett.*, **105**, 027203 (2010).
27) S. Yanai, D. Oshima, S. Takahashi, Y. Hirayama, and T. Kato: Jpn. *J. Appl. Phys.*, **62**, SB1004 (2023).
28) H. Shul: *Phys. Rev.*, **97**, 555 (1955).
29) N. Kamiya, D. Oshima, S. Iwata, and T. Kato: *J. Magn. Soc. Jpn.*, **45**, 96 (2021).
30) D. M. Lattery, J. Zhu, D. Zhang, J. -P. Wang, P. A. Crowell, and X. Wang: *Appl. Phys. Lett.*, **113**, 162405 (2018).

Received Sep. 29, 2022; Accepted Mar. 29, 2023

J. Magn. Soc. Jpn., **47**, 115-117 (2023) <Letter>

First-order reversal curve analysis of superparamagnetic nanoparticles with oriented easy axis of magnetization

Eisuke Sasaoka, Chao Yang*, Suko Bagus Trisnanto, Zenglu Song*, Satoshi Ota**, and Yasushi Takemura

Division of Electrical and Computer Engineering, Yokohama National University, *Yokohama 240-8501, Japan*
*School of Electrical Engineering, Nanjing Vocational University of Industry Technology, *Nanjing 210023, China*
**Department of Electrical and Electronic Engineering, Shizuoka University, *Hamamatsu 432-8561, Japan*

We analyzed the magnetization process of magnetic nanoparticles using first-order reversal curve (FORC) analysis and verified a superparamagnetic feature and the orientation of the easy axis of the particles. The FORCs and FORC diagram of magnetic nanoparticles dispersed in water exhibited a superparamagnetic feature. The differences in the magnetizations and distributions of the coercive force of the solid-state samples were used to identify the orientation of the easy axes of magnetization.

Key words: magnetic nanoparticles, first-order reversal curve (FORC), superparamagnetism, magnetic anisotropy, magnetization easy axis

1. Introduction

Magnetic nanoparticles are expected to be used in various biomedical applications[1]. To prevent aggregation of particles in blood vessels, superparamagnetic nanoparticles with diameters of or less than 10–20 nm and exhibiting no residual magnetization have been widely studied. In our previous studies, we reported the static and dynamic magnetization properties of magnetic nanoparticles and found that the self-heating characteristic of hyperthermia can be enhanced by orienting the easy axes of the magnetic particles[2-4].

The current study aims to evaluate the magnetization properties of magnetic nanoparticles with oriented or non-oriented easy axes. We performed a first-order reversal curve (FORC) analysis[5,6]. FORC is an advanced hysteresis measurement method used for deriving the distribution of and information regarding the magnetization properties of magnetic materials, which can otherwise not be achieved using the normal hysteresis curves of magnetization measurement that provides a total or average magnetization property in magnetic materials.

In this paper, we report a superparamagnetic feature and the distribution of the coercive force of superparamagnetic nanoparticles evaluated using FORC analysis. A reversible change in magnetization without any remanent magnetization or a coercive field was observed in the magnetic nanoparticles dispersed in a liquid medium; however, remanent magnetization was clearly observed in the nanoparticles that remained fixed in a solid state. The distribution of the coercive force and interaction fields according to the direction of the easy axis of magnetization was identified in the FORC diagrams of the solid-state samples.

Corresponding author: Yasushi Takemura
(e-mail: takemura@ynu.ac.jp).

2. Experimental method

A commercial magnetic fluid distributed as a contrast agent in magnetic resonance imaging, Resovist® (FUJIFILM RI Pharma, Japan), was employed in this study. It contains multi-core particles of γ-Fe_2O_3 dispersed in water. The single core diameter and effective multi-core diameter were 5–10 nm and 5–30 nm, respectively[7,8]. We prepared three samples from Resovist®: one liquid sample and two types of solid samples. The density of all the samples was adjusted to 2.8 mg-Fe/ml. The liquid sample was prepared by diluting Resovist® whose original density was 28 mg-Fe/ml.

The solid samples were prepared by mixing Resovist® with epoxy (CEMEDINE, Japan). A DC magnetic field of $\mu_0 H$ = 870 mT was applied to one of the solid samples using NdFeB magnets during epoxy solidification. The magnetization of the original Resovist® in its liquid state under this intensity of the applied magnetic field was 0.95 M/M_s, where M/M_s denotes the magnetization normalized by saturation. The easy axes of the magnetic nanoparticles were aligned in this solid sample. The magnetic field applied during the FORC measurement of this sample was either parallel (easy axis field) or perpendicular (hard axis field) to the oriented easy axis, respectively, as shown in Fig. 1.

Another solid sample was prepared without applying a magnetic field during the epoxy solidification. The easy axes of the particles were randomly oriented. The details of the sample preparation and both static and dynamic magnetization measurements have been previously reported[3,4].

Static magnetization curves, including the FORCs, were measured using a vibrating sample magnetometer (model 8600 series, Lake Shore Cryotronics, USA) at room temperature.

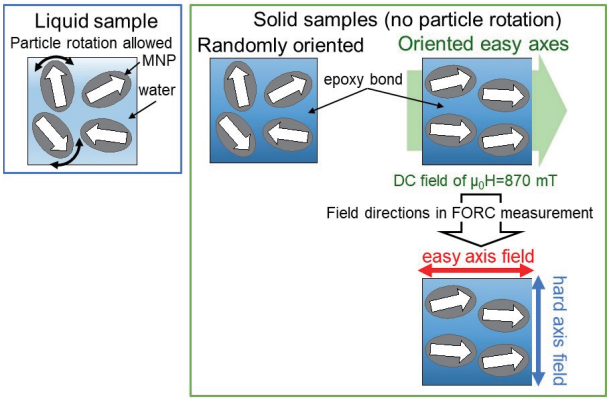

Fig. 1 Preparation of liquid and solid samples. Magnetic field applied in FORC measurements was either parallel (easy axis field) or perpendicular (hard axis field) to oriented easy axes of solid sample.

3. Results and discussion

The FORCs were first measured, and the samples were saturated in a large positive field, H_{sat} = 2.0 T/μ_0. Then, the applied field intensity was decreased, thereby forming a reversal magnetic field, H_a = −2.0 T/μ_0. FORC is defined as the magnetization curve derived by increasing H_a to H_{sat}. This process was repeated for several values of $\mu_0 H_a$ to yield a series of FORCs. A sweep rate of the applied magnetic field was 5 mT/s.

Figures 2(a)–(d) show the FORCs of the liquid, random-oriented, and oriented easy axis samples, respectively. As can be seen, the FORCs of the liquid sample exhibit a superparamagnetic feature without a coercive field and any remanent magnetization. The curves traced using various overlapping values of H_a suggest a reversal of magnetization. The two solid samples exhibit remanent magnetization due to the fixed easy axes having magnetic anisotropy. The magnetization of the liquid sample is greater than that of the randomly orientated solid sample because of the additional magnetization reversal caused by particle rotation[4]. The differences observed in the magnetization processes of the three solid samples are consistent with the previously reported major and minor magnetization loops of our similar samples[3].

The FORC distribution is defined as a mixed second derivative and can be expressed as follows:

$$\rho(H_a, H_b) = -\frac{\partial^2 M(H_a, H_b)}{\partial H_a \, \partial H_b} \quad (1)$$

Here, the magnetization value measured under a specific applied magnetic field, $\mu_0 H_b$ is defined as M (H_a, H_b), where $H_b \geq H_a$. The calculated FORC distributions are described as a contour plot of the parameter space of H_a and H_b, which is called a FORC diagram[6]. To analyze the coercive field, H_c, and the interaction field, H_u, the FORC distribution of $\rho(H_c, H_u)$ was obtained via coordinate

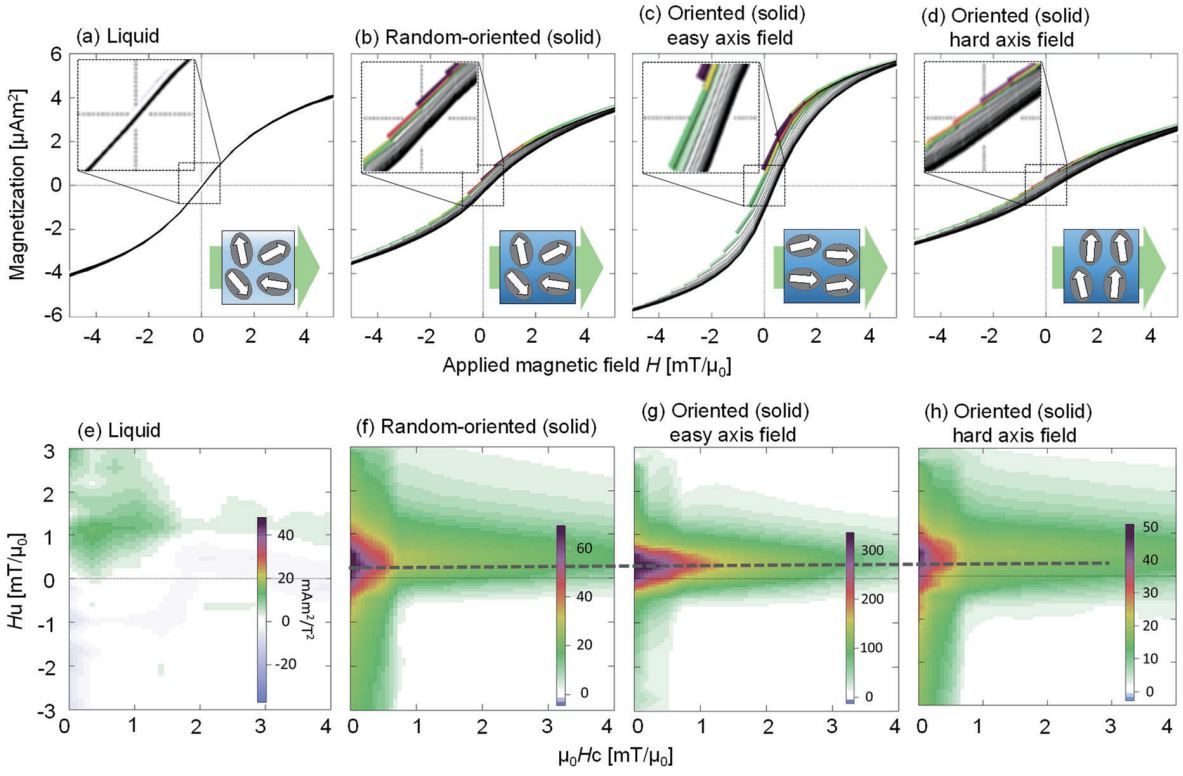

Fig. 2 Magnetization reversal curves, FORCs (a-d) and FORC diagrams (e-h): (a, e) liquid sample, (b, f) random-oriented sample, (c, g) oriented sample under easy axis field, and (d, h) oriented sample under hard axis field. Colors in FORC and FORC diagrams of each sample are corresponding.

transformation as follows:

$$\mu_0 H_c = (\mu_0 H_b - \mu_0 H_a)/2 \quad (2)$$

$$\mu_0 H_u = (\mu_0 H_b + \mu_0 H_a)/2 \quad (3)$$

An open-source software, FORCinel[9] was used for calculating the FORC distributions.

Figures 2(e)-(h) show the FORCs of the four samples. The colors in the FORCs and FORC diagram of each sample are corresponding. As shown in Fig. 2(e), the liquid sample has a negligible change of intensity in the FORC distribution, $\rho(H_c, H_u)$; this change caused by slight deviations from the several repeated magnetization curves.

A significant finding in this study is the apparent differences in the FORC diagrams of the solid samples depending on the orientation of the easy axis of magnetization. The peaks of $\rho(H_c, H_u)$ in the FORC diagrams of the solid samples are observed on the H_u axis, where H_c=0, suggesting that the magnetization property is dominantly superparamagnetic. The diagram of the randomly oriented sample shows a distribution of the coercive field in the range of 0–1 mT/μ_0, as shown in Fig. 2(f). The particle diameter of Resovist® has a wide distribution and ranges between 5 and 30 nm[7,8]. The coercive force of the solid samples is commonly attributed to the larger particles exhibiting ferromagnetism. The distributions of $\rho(H_c, H_u)$ along the H_c axis of the solid samples are attributed to the ferromagnetic particles, whose contribution monotonically increases with increasing their diameter. Additionally, the enhanced anisotropic energy associated with the binding of the easy axis induces a coercive field in the solid samples[10,11]. The ferromagnetic particles in the liquid sample do not show a coercive force because of particle rotation that is sufficiently activated at room temperature. These features are supported by Brownian and Néel relaxation times depending on a particle diameter[12]. As for a 30-nm particle, the Néel relaxation time is sufficiently long for exhibiting ferromagnetism of solid samples. The Brownian relaxation time is approximately 10 μs for particles with 5–30 nm, resulting in superparamagnetic properties of liquid samples.

The coercive field under an applied field along the easy axis is more widely distributed toward the greater range than that of the randomly oriented sample and under the hard axis field. This demonstrates an enhanced magnetic anisotropy caused by the alignment the easy axis of magnetization. Opposingly, the coercive field under the hard axis field is the lowest among three measurements of the solid samples as shown in Figs. 2(f)-(h). This denotes magnetization rotation with small amplitude responding to an applied magnetic field with small intensity. The wider distribution of $\rho(H_c, H_u)$ under the hard axis field is observed along the large H_c region than those of the other solid samples. This suggests that further rotation of magnetization toward the direction of an applied field, which is a hard axis of magnetization with higher anisotropic energy, requires an applied field with higher intensity.

As shown by the dotted line in Figs. 2(f)-(h), a slight difference in the distributions of the interaction field, H_u, reflecting the magnetic interaction between the particles[13] was observed in the solid samples. However, the intrinsic mechanism modifying H_u by the orientation of the easy axis of magnetization is not elucidated in this study.

In summary, the FORCs and FORC diagrams of the magnetic nanoparticles were studied. The liquid sample exhibited a superparamagnetic feature; however, the solid samples had coercive forces depending on the orientation of the magnetization easy axes. These results are explained by the distribution of particle size in the samples and the magnetic anisotropy associated with the easy axis of the samples.

Acknowledgements This work was partially supported by the JSPS KAKENHI JP20H05652 and JP20H02163.

References

1) Q. A. Pankhurst, N. K. T. Thanh, S. K. Jones, and J. Dobson: *J. Phys. D*, **42**, 224001 (2009).
2) T. Yoshida, Y. Matsugi, N. Tsujimura, T. Sasayam, K. Enpuku, T. Viereck, M. Schilling, and F. Ludwing: *J. Magn. Magn. Mater.*, **427**, 162 (2017).
3) G. Shi, R. Takeda, S. B. Trisnanto, T. Yamada, S. Ota, and Y. Takemura: *J. Magn. Magn. Mat.*, **473**, 148 (2019).
4) T. Yamaminami, S. Ota, S. B. Trisnanto, M. Ishikawa, T. Yamada, T. Yoshida, K. Enpuku, and Y. Takemura: *J. Magn. Magn. Mat.*, **517**, 167401 (2021).
5) S. Okamoto, T. Yomogita, K. Miyazawa, N. Kikuchi, O. Kitakami, N. Watanabe, and N. Suita:. *Mater. Jpn.*, **56**, 533 (2017) [in Japanese].
6) C. Pike, A. Roberts, and K. Verosub: *J. Appl. Phys.*, **85**, 6660 (1999).
7) S. Ota, S. B. Trisnanto, S. Takeuchi, J. Wu, Y. Cheng, and Y. Takemura: *J. Magn. Magn. Mat.*, **538**, 168313 (2021).
8) T. Yoshida, N.B. Othman, and K. Enpuku: *J. Appl. Phys.*, **114**, 173908 (2013).
9) R. J. Harrison and J. M. Feinberg: *Geochem. Geophys. Geosyst.*, **9**, Q05016 (2008).
10) R. Takeda, S. Ota, T. Yamada, and Y. Takemura: *J. Magn. Soc. Jpn.*, **42**, 56 (2018).
11) S. Ota and Y. Takemura: *J. Magn. Soc. Jpn.*, **43**, 34 (2019).
12) R. Kötitz, W. Weitschies, L. Trahms, W. Brewer, and W. Semmler: *J. Magn. Magn. Mater.*, **194**, 62 (1999).
13) H. Mamiya, I. Furukawa, J. L. C. Huaman, K. Suzuki, H. Miyamura, and B. Jeyadevan: *J. Phys. Commun.*, **5**, 045003 (2021).

Received Jan. 03, 2023; Revised Jan. 31, 2023; Accepted Apr. 20, 2023

J. Magn. Soc. Jpn., **47**, 118-127 (2023) <Paper>

Development of Ultra-Low Field Magnetic Resonance Imaging System at 1 mT

D. Oyama[1], N. Tsuyuguchi[1,2,3], J. Hirama[4], Y. Adachi[1], and J. Kawai[1]

[1]Applied Electronics Laboratory, Kanazawa Institute of Technology, *3 Amaike, Kanazawa, Ishikawa, 920-1331, Japan*

[2] Department of Neurosurgery, Kindai University, *377-2 Ono-higashi, Osakasayama, Osaka, 589-8511, Japan*

[3] Neurosurgery, Naniwaikuno Hospital, *1-10-3 Daikoku, Naniwa, Osaka, Osaka, 556-0014, Japan*

[4] Department of Electrical and Electronics Engineering, Kanazawa Institute of Technology, *7-1 Ohgigaoka, Nonoichi, Ishikawa, 921-8501, Japan*

Ultra-low field (ULF) magnetic resonance imaging (MRI) is considered an innovative MRI technique that can be combined with magnetoencephalography (MEG). In this study, a 1-mT ULF-MRI system without a pre-polarization technique aiming at combining an MEG system is developed. The intensity of the static magnetic field B_0 is decided considered to be 1 mT because of the limitation of the magnetic field exposed to our MEG sensor made of superconducting quantum interference devices (SQUIDs). A square-shaped (750 mm × 750 mm) B_0-coil based on a Merritt-type configuration is fabricated. The inhomogeneity of B_0 is less than 0.07 % in the ±125 mm area. Further, an induction coil is employed to detect the magnetic resonance signal instead of the SQUID sensors of the MEG to confirm the feasibility of realizing MRI measurement at 1 mT without the pre-polarization technique. Relaxation time measurements and MR imaging of a phantom made of a $CuSO_4$ aqueous solution are performed. Reasonable longitudinal and transverse relaxation times are obtained, and clear shapes of the phantom are obtained using the gradient- and spin-echo pulse sequences with this ULF-MRI system. These results indicate the potential of the proposed 1-mT ULF-MRI to effectively integrate ULF-MRI and MEG systems without pre-polarization.

Key words: magnetic resonance imaging, magnetoencephalography, ultra-low field MRI

1. Introduction

Magnetic resonance imaging (MRI) is an indispensable imaging tool used in modern medicine. Superconducting magnets are widely used in clinical applications to generate a high magnetic field (>1 T) because the amplitude of the MR signal is approximately proportional to the square of the magnetic flux density. Therefore, the quality of the obtained MR image can generally be improved by increasing the static magnetic field B_0 of the MRI.

Recently, MRI systems with much lower magnetic fields have been developed[1]. A lower magnetic field has some benefits to compensate for some of the disadvantages of high-field MRIs, such as initial and running costs, portability, weight, size, sound noise, and safety. Several research groups have developed low-field MRI systems using magnetic fields between several mT to several tens of mT and realized the imaging of a human head with a quality to distinguish some lesions[2)–4)].

Further, MRI measurements in the magnetic fields of micro-Tesla range, called ultra-low field MRI (ULF-MRI), have also been studied as innovative MRI since the early 2000s[5)–7)]. An expected application of the ULF-MRI is combining it with magnetoencephalography (MEG) measurements. MEG observes the magnetic signals generated by neuronal activities in the human brain using ultra-high-sensitivity magnetic sensors, such as superconducting quantum interference devices (SQUIDs). The source of the magnetic signal can be estimated from the MEG signal detected by a multi-channel magnetic sensor array, normally several tens or over 100 channels. An anatomical image is necessary to precisely estimate the signal source and show the results of signal source localization. MR images are commonly employed for this purpose; however, the co-registration error between the MEG and MRI systems causes source localization errors. Therefore, both MEG and MRI data must be acquired using a single modality. High-field MRI cannot be combined with the MEG machine because a high magnetic field, which is usually greater than the critical magnetic field of SQUID, disrupts the superconductivity of SQUID sensors. ULF-MRI has the best prospect for combining the MEG and MRI measurements.

Several research groups have developed SQUID-based ULF-MRI systems using magnetic fields ranging from tens of μT to 200 μT to capture human head MR image[8)-14)]. We also developed a ULF-MRI system to combine small-animal MEG with a B_0 of 33 μT[15), 16)]. In these ULF-MRI systems, a pre-polarization technique that applies a magnetic field pulse (B_p-pulse) to the samples or subjects was used to increase the amplitude of the MR signal. The B_p-pulse has to be much stronger than B_0; therefore, the intensities of the B_p-pulse in previous studies were more than 10 mT (sometimes over 100 mT). Even though the protection techniques for SQUID sensors have been proposed and included in the developed ULF-MRI systems[7), 9), 10), 17), 18)], some difficulties still arise for their

Corresponding author: D. Oyama (e-mail: oyama@neptune.kanazawa-it.ac.jp).

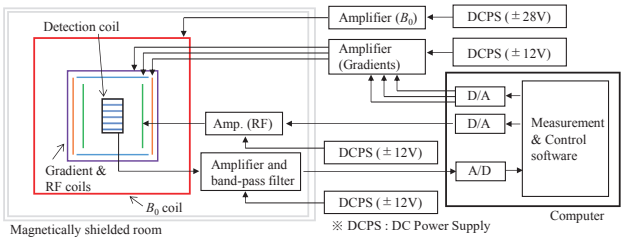

Fig. 1 Block diagram of our ULF-MRI system.

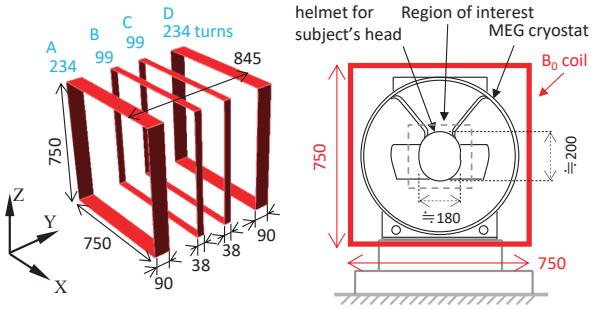

Fig. 2 Simplified drawings of the designed static magnetic field (B_0) coil and the MEG cryostat.

practical applications, such as increase in the measurement time due to applying the B_p-pulse, difficulty in avoiding the eddy current in the metal material such as electromagnetic shields, and increasing the equipment scale to generate the B_p-pulse.

The purpose of this study is to develop a ULF-MRI system integrated with MEG. Rather than applying a B_p-pulse to boost the amplitude of the MR signal to be detected, the static magnetic field was increased from 33 μT to 1 mT. As described above, increasing B_0 not only increases the amplitude of the MR signal but also affects the SQUID sensors. The static magnetic field was set to 1 mT, in reference to the limitation in the magnetic field, whereby the SQUIDs of the MEG system could maintain their frequency response sufficient for detecting the MR signal (refer to Appendix A).

However, no research has been conducted to demonstrate the possibilities of MRI measurement at approximately 1 mT[1]. This study aims to fabricate a 1-mT ULF-MRI system and reveal the advantages, possibilities, and problems in realizing MRI measurements at 1 mT without pre-polarization techniques. Section 2 presents the system configuration. Sections 3 and 4 present some experiments, including relaxation time and MRI measurements using a phantom. Section 5 discusses the advantages and problems of the 1-mT ULF-MRI.

2. Instrumentation

2.1 System overview

Fig. 1 shows the configuration of the ULF-MRI system. The coil set to generate the B_0-field, gradient fields, and RF pulse was installed inside a magnetically shielded room made of two layers of mu-metal and one layer of copper.

These coils were driven by current-amplifier electronics. The DC current of the B_0-coil was manually tuned to generate the desired magnetic field density. The current pulses for the gradient fields and RF pulse are generated by digital-to-analog (D/A) converters (for the gradient fields: DAQe-2502, ADLINK Inc., for the RF pulse: PCIe-6353, National Instruments) with sampling frequencies of 100 kHz and 2 MHz, respectively.

Further, an induction coil was employed to detect the MR signal instead of SQUID sensors to demonstrate the possibility of MRI measurements without pre-polarization at 1 mT. The induced voltage was recorded using an analog-to-digital (A/D) converter (PCIe-6353, National Instruments) with a sampling frequency of 1.25 MHz. Although a high-field MRI system typically uses a signal mixer to generate the RF pulse or record the MR signal, the proposed system generates the RF pulse and records the MR signal directly by the D/A and A/D converters because the sampling frequencies of the devices are much higher than the signal frequency (approximately 42–43 kHz).

2.2 B_0-coil

A Merritt-type configuration was employed for the B_0-coil[19]. The Merritt-type configuration generates a uniform magnetic field distribution compared with other coil configurations, such as the Helmholtz-type configuration coil[20]. One purpose for developing the ULF-MRI was to combine it with our MEG system[21]. Fig. 2 shows simplified drawings of the designed B_0-coil which is virtually combined with the MEG cryostat. To observe the human head, the size of the region of interest (ROI) and length of the coil side were set to 250 and 750 mm, respectively.

The total number of turns of the coil was 666 and the estimated magnetic flux density was 1.0 mT by applying an electric current of 1.79 A. A copper wire with a diameter of 1.4 mm was wound on a frame made of resin. The total resistance and inductance were 24.1 Ω and 300 mH, respectively. The total weight of the B_0-coil was approximately 30 kg. The coil frames, labeled as A-D shown in Fig. 2 (a), can be separated; therefore, this B_0-coil can be easily carried and assembled by a single person.

Fig. 3 shows the magnetic field inhomogeneity of the B_0-field calculated based on the B_0-coil design. The magnetic field strength can be calculated using the Biot–Savart law, assuming a 666-turn coil as 2664 (4×666) linear currents. Inhomogeneity was defined as the difference from the magnetic flux density at the coil center (X = 0, Y = 0, and Z = 0) in percentage. An inhomogeneity of less than 0.07 % (700 ppm) was obtained in the designated ROI (±125 mm), as indicated by dashed lines.

Typically, a magnetic field inhomogeneity of less than 50 ppm is necessary for high-field MRIs. To confirm that the uniformity of our B_0 field has acceptable for MRI measurements, an MRI measurement was simulated

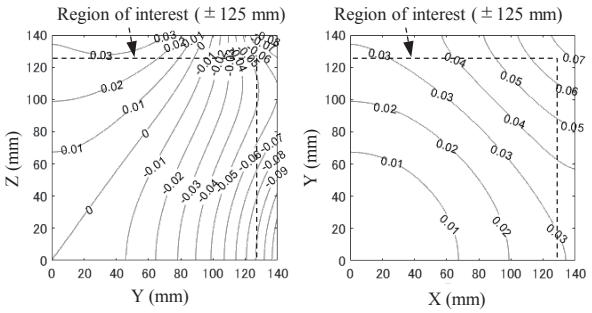

Fig. 3 Calculated magnetic field distribution of the designed B_0-coil; owing to the symmetry, the calculation is performed only in positive quadrants ($X \geqq 0$, $Y \geqq 0$, and $Z \geqq 0$). The values on the contour lines indicate the difference in percentage from the magnetic flux density at the center of the coil ($X = 0$, $Y = 0$, and $Z = 0$).

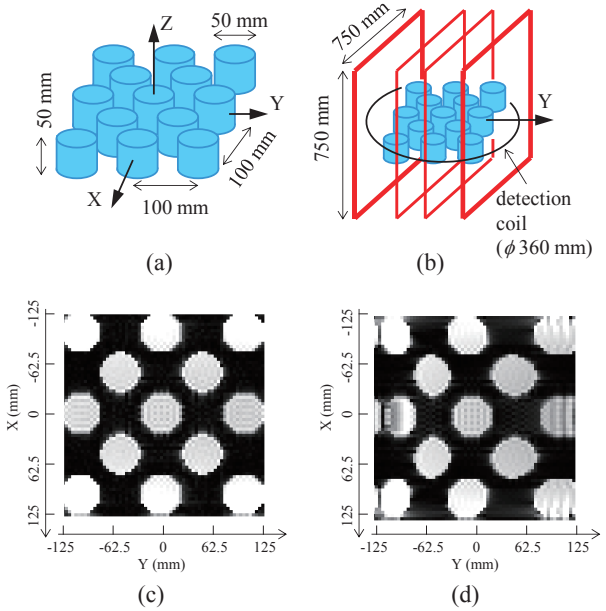

Fig. 4 Simulation of the effect of the distortion of the static magnetic field. (a) Simulation model, (b) arrangement of the coils, (c) obtained MR image at 1 mT, and (d) obtained MR image at 10 mT.

using the calculated magnetic field distribution; the simulation conditions are shown in Figs. 4 (a) and (b). The subject model of the MRI simulation consisted of 13 cylinders, as shown in Fig. 4 (a), and a circular coil with a diameter of 360 mm was assumed as the detection coil, as shown in Fig. 4 (b). The MR signals were calculated assuming the gradient-echo pulse sequence, and subsequently, the MR images were reconstructed. The algorithm of the simulation is presented in Appendix B. To reduce the calculation time, two-dimensional (2D) imaging in the X-Y plane sequences was assumed, and the reconstructed images showed the projection image on the Z-axis. For comparison, MRI measurements at 1 and 10 mT were simulated, as shown in Figs. 4 (c) and (d), respectively. The magnetic field distribution with $B_0 = 10$ mT was calculated by applying an electric current of 17.9

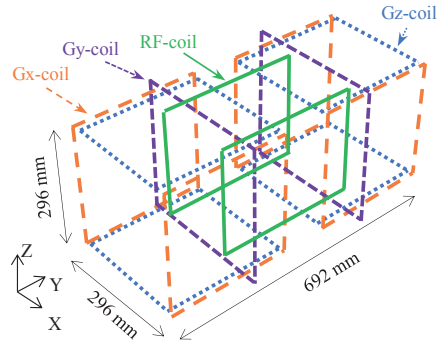

Fig. 5 Coil-set for the gradient magnetic field and RF pulse coils.

A to the designed B_0-coil. Therefore, the magnetic field inhomogeneity was same as that shown in Fig. 3. As shown in Fig. 4 (c), an MR image indicating 13 cylinders was obtained with $B_0 = 1$ mT. In contrast, the MR image obtained with $B_0 = 10$ mT was distorted owing to the static magnetic field inhomogeneity as shown in Fig. 4 (d). These results show that the designed B_0-coil has sufficient magnetic field homogeneity for 1-mT ULF-MRI measurements.

2.3 Current driver for the B_0-coil

The signal frequency is given by $f_{signal} = \gamma \cdot B_0$, where γ is the geomagnetic ratio (42.58 MHz/T for proton). Therefore, the signal frequency is 42.58 kHz when B_0 is 1 mT. The stability of the B_0-field is important for obtaining clear MR images. The current driver circuit for the B_0-coil was fabricated using a constant-current circuit configuration to maintain the current fluctuation within 1 mA. The corresponding fluctuation in B_0 and f_{signal} were calculated as 559 nT (1mT / 1.79 A × 1 mA) and 23.8 Hz, respectively.

A dropper-type DC power supply (GPP-4323G, Good Will Instrument Co., Ltd.) was selected to eliminate magnetic noise from the power supply to the MRI and MEG systems. The use of a benchtop DC power source also helped keep the system compact. The power consumption necessary to apply 1.79 A to the B_0-coil was estimated to be 77.2 W (24.1 Ω × $(1.79\ \mathrm{A})^2$).

2.4 Gradients and RF pulse coils

In this study, these coils were designed to realize a field-of-view (FOV) of 120 mm for confirmation of the measurement principle. Fig. 5 shows the coil set for the gradient field and RF pulse. This coil set was installed at the center of the B_0-coil that generates a static magnetic field in the y-direction. The designed gradient fields were $G_X = dB_Y/dX = 398$ nT/mm/A, $G_Y = dB_Y/dY = 631$ nT/mm/A, and $G_Z = dB_Y/dZ = 418$ nT/mm/A.

The orientation of the RF pulse was set in the x-direction, and the strength of the RF pulse was calculated minimized at 42.6 kHz, which corresponds to the Larmor frequency of the proton at 1 mT by attaching a capacitance in series to the RF coils.

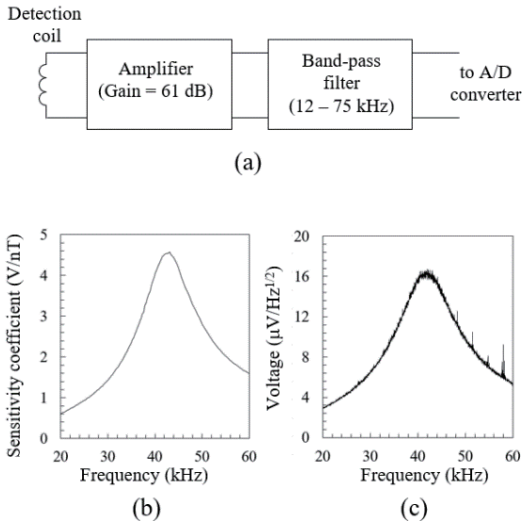

Fig. 6 Block diagram and characteristics of the detection unit: (a) block diagram, (b) sensitivity coefficient, and (c) noise spectrum.

2.5 Detection coil and amplifier

The detection coil has inner diameter, outer diameter, and length of 76, 90, and 80 mm, respectively. The coil was wound using a Litz wire and 583 turns in six layers. The inductance and internal resistance of the coil were 17 mH and 9 Ω, respectively. Fig. 6 shows the block diagram and characteristics of the detection unit consisting of the detection coil, amplifier (61 dB), and a band-pass filter (12–75 kHz).

Figs. 6 (b) and (c) show the sensitivity coefficient and noise spectrum of the detection unit output, respectively. The sensitivity coefficient was measured by applying a uniform magnetic field to the detection coil, and the noise level was recorded when the current driver circuits for the coil set were turned off. Although an additional capacitor to make the LC resonance circuit was not implemented between the detection coil and amplifier, a peak at 43 kHz appeared in both graphs. The LC resonance was assumed to occur due to the inductance and stray capacity of the detection coil and input capacitance of the amplifier circuit. The sensitivity coefficient and voltage noise at 43 kHz were 4.6 V/nT and 16.7 μV/Hz$^{1/2}$, respectively. Therefore, the corresponding noise level of the detection unit was estimated to be 3.6 fT/Hz$^{1/2}$ at 43 kHz.

3. Experimental Method

3.1 Sample

Herein, the experiments were conducted using a phantom to confirm the feasibility of our MRI system. The concentric container was made from acrylic plastic tubes, and the gaps in the tubes were filled with a 0.1 % copper sulfate ($CuSO_4$) aqueous solution, which is employed for conventional MRI phantoms. The total volume of the aqueous solution was approximately 190 g.

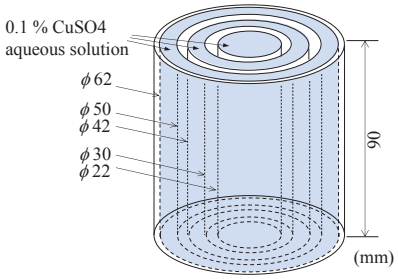

Fig. 7 Dimension of a phantom used for experiments.

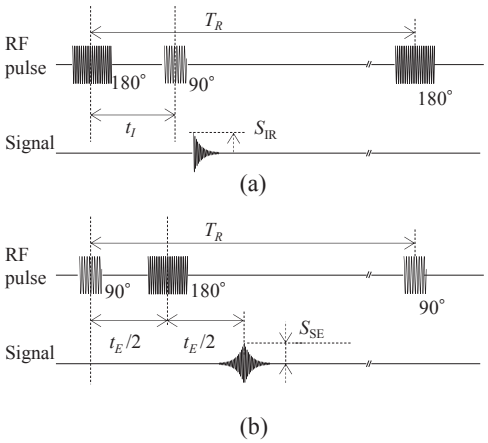

Fig. 8 Pulse sequences for relaxation time measurement: (a) inversion recovery sequence and (b) spin-echo sequence.

3.2 Relaxation time measurements

To design the pulse sequence for MRI measurements, the relaxation time of the aqueous solution of the phantom must be known. Herein, the relaxation time was measured using the inversion recovery (IR) sequence for the longitudinal relaxation time (T_1) and the spin-echo (SE) sequence for the transverse relaxation time (T_2), as shown in Fig. 8.

In the IR sequence, 180° and the 90° pulses were applied to the phantom, and the free-induction-decay (FID) signal was observed immediately after the 90° pulse. By changing the time gap of the pulses (t_I), the amplitude of the FID signal S_{IR} varied as follows.

$$S_{IR}(t_I) = S_{0,FID} \times (1 - 2e^{-\frac{t_I}{T_1}}) \quad , \tag{1}$$

where $S_{0,FID}$ is the FID signal amplitudes when the protons are in the thermal equilibrium state. The relaxation time T_1 is the time constant of the exponential curve; thus, it can be estimated by solving an inverse problem, such as the least-squares method. Herein, T_1 relaxation time was measured with t_I = 20, 30, 40, … 330 ms and a repetition time of T_R = 800 ms.

In the SE sequence, the 90° and the 180° pulses were applied to the phantom with a time gap $t_E/2$; subsequently, the echo signal was observed $t_E/2$ after the 180° pulse. By changing t_E, the amplitude of the echo signal S_{SE} varied as follows.

$$S_{SE}(t_E) = S_{0,SE} \times e^{-\frac{t_E}{T_2}} \quad , \tag{2}$$

where $S_{0,SE}$ is the echo-signal amplitudes when t_E is

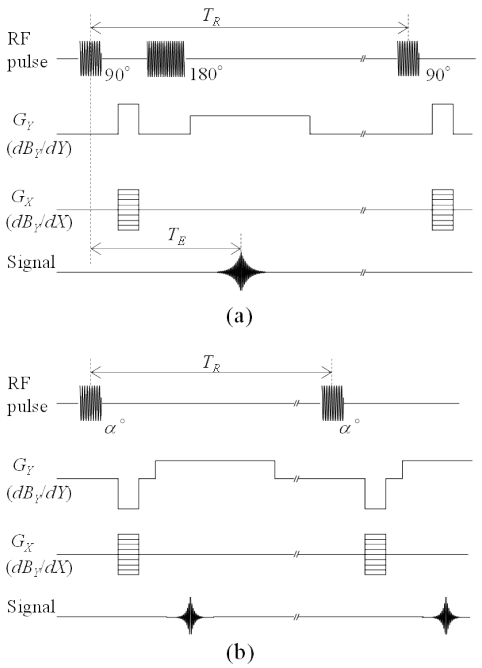

Fig. 9 Pulse sequences for MRI measurements: (a) spin-echo and (b) gradient echo.

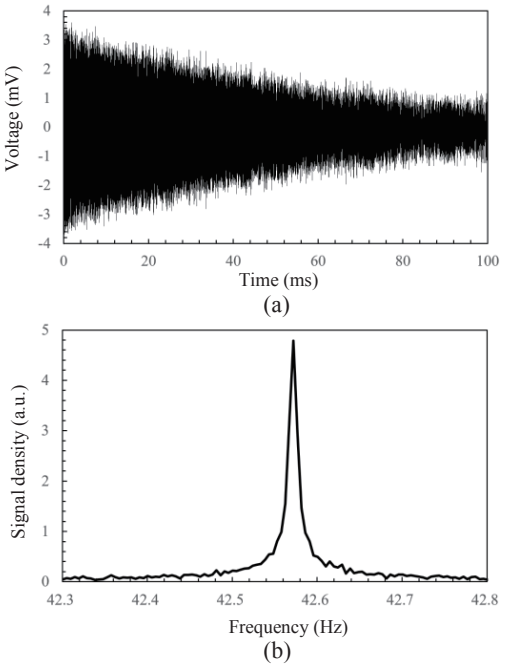

Fig. 10 Results of the spin-echo signal recording: (a) waveform and (b) frequency spectrum.

assumed to be zero. Similar to the T_1 relaxation time, the value of T_2 can be estimated by solving the inverse problem. Herein, the T_2 relaxation time was measured with t_E = 20, 30, 40, … 330 ms and a repetition time of T_R = 800 ms.

3.3 Imaging

In this study, two pulse sequences, namely spin-echo and gradient-echo (GE) sequences, were demonstrated for the 2D MRI measurements, as shown in Fig. 9. Generally, the SE sequence is more robust against the inhomogeneity of the static magnetic field compared with the GE sequence; however, it requires a longer measurement time because the repetition time (T_R) must be much longer than the T_1 relaxation time of the aqueous solution. The GE sequence is easily influenced by the inhomogeneity of the static magnetic field; however, the measurement time can be reduced by short T_R with an arbitrary flip angle (α) of the RF pulse.

These encoding schemes were designed based on the 2D Fourier protocol with a frequency encoding gradient G_Y = ±195 nT/mm (8.33 Hz/mm, 31.25 Hz/pixel) and a phase-encoding gradient G_X = ± 390 nT/mm/32-steps (1.04 Hz/mm). The size of the produced image was 32 × 32 pixels, and the FOV was set to 120 mm × 120 mm in the X- and Y-directions, respectively. Therefore, the pixel size was calculated to be 3.75 mm × 3.75 mm.

The timing parameters of T_R and T_E for the SE pulse sequence and T_R for the GE sequence were 350, 32, and 100 ms, respectively. These values were defined based on the relaxation-time measurements reported in the next section. The recording was repeated 100 times for averaging; therefore, the total acquisition times were 1120 and 320 s for the SE and GE sequence, respectively.

The amplitude and exposure time of the RF pulse were adjusted to maximize the MR signal before the MRI measurements. Herein, α for the GE sequence was 72°.

4. Results

A direct current was applied to the gradient coils to compensate for the static magnetic field inhomogeneity owing to the background magnetic field distribution in the MSR. The intensity of the applied current was tuned to maximize the amplitude of the observed magnetic resonance signal.

4.1 Spin-echo signal

First, the SE signal was recorded to confirm that the MR signal can be detected by the 1-mT MRI system. The pulse sequence shown in Fig. 8 (b) with t_E = 20 ms was used for measurements. Each data point was obtained by 100-times averaging and applying a digital band-pass filter (42.6±0.5 kHz) after recording.

The shape of the obtained echo signal is shown in Fig. 10 (a). The spin-echo magnetic resonance signal is typically observed as a bilaterally symmetric waveform, as shown in Fig. 8 (b). In this experiment, the attenuation time of the magnetic resonance signal caused by the inhomogeneity of the static magnetic field, usually denoted as T_2*, was much longer than the echo time t_E. Therefore, the echo signal was observed as a simple attenuation waveform, not bilateral symmetry.

Fig. 10 (b) shows the frequency spectrum of the observed signal. The peak frequency of 42.57 kHz was good agreement with the Larmor frequency at 1 mT. Therefore, it was confirmed that the SE signal was successfully observed by the 1-mT ULF-MRI system without pre-polarization technique.

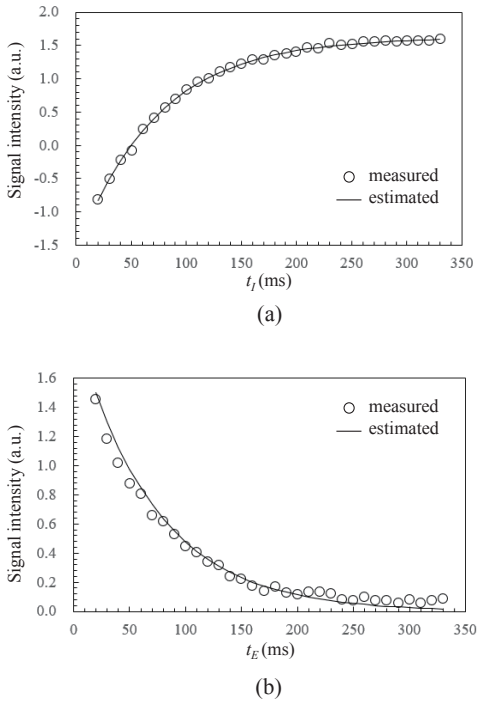

Fig. 11 Results of the relaxation time measurements: (a) T_1 and (b) T_2 relaxation time.

Additionally, the sufficient stability of the signal frequency was also confirmed by continuous recording of the SE signal. The frequency shift in 3 hours was approximately 14 Hz (refer to Appendix C). This signal frequency shift is less than 31.25 Hz, which corresponds to one pixel of the MR image in the frequency-encoding direction as defined in Subsection 3.3, confirming that the generated static magnetic field is sufficiently stable for ULF-MRI measurements.

4.2 Relaxation time

Fig. 11 shows the results of the relaxation time measurements for (a) T_1 and (b) T_2 relaxation times. The recorded data were preprocessed (100-times averaged and band-pass filtered), as described in the data shown in Fig. 10, and then the signal amplitudes S_{IR} and S_{SE} were calculated and plotted in Figs. 11 (a) and (b) as circles, respectively. The lines are the fitting curves obtained using the estimated variables included in equations (1) and (2). The relaxation times T_1 and T_2 of the phantom were estimated as 71.7 ms and 69.6 ms, respectively. The timing parameters of T_R and T_E for the SE imaging sequence were $T_R > T_1$ and $T_E < T_2$.

4.3 Imaging

Fig. 12 shows the results of the MRI measurements using the GE and SE sequences, as shown in Fig. 9. The recorded data were preprocessed (100-times averaging and band-pass filtered), as described in subsections 4.1 and 4.2; subsequently, they were digitally frequency-converted using the sine and cosine function with a frequency of 42.6 kHz corresponding to the Larmor frequency at 1 mT. Figs. 12 (a) and (b) show the

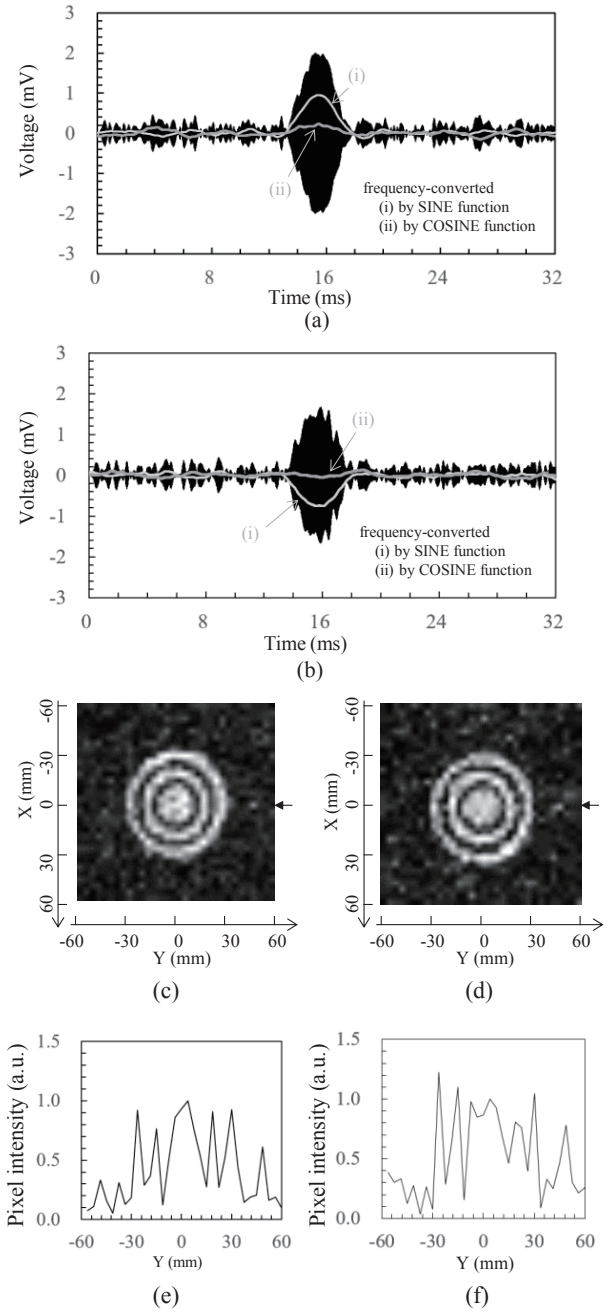

Fig. 12 Results of the MR imaging using the (a), (c), (e) spin-echo and (b), (d), (f) gradient-echo sequences; (a), (b) observed echo signals, (c), (d) reconstructed MR images, and (e), (f) pixel intensity along the line indicated by arrows in (c) and (d), respectively.

preprocessed waveforms and frequency-converted signals with the SE and GE sequences, respectively, when the phase encoding (G_x) pulses were zero. The frequency-converted signal was down sampled to 1 kHz to ensure that the number of data points per recording was 32. The number of phase encodings was 32; therefore, the size of the k-space data matrix was 32 × 32 for each dataset.

Figs. 12 (c) and (d) show the reconstructed MR images obtained by applying a 2D fast Fourier transform (FFT)

to the *k*-space data. Concentric circles separated by a 4-mm-thick cylinder, as shown in Fig. 7, clearly appear in both figures. Figs. 12 (e) and (f) show the pixel intensity of the MR images shown in Figs. 12 (c) and (d) along the line indicated by the arrows. The pixel intensity was normalized to the pixel intensity at the center of the MR image. Assuming that the MR signal was not included in the images with $|Y| > \pm 31$ mm, the noise levels were estimated to be 0.20 and 0.31 in Figs. 12 (c) and (d), respectively. Therefore, the signal-to-noise ratio (SNR) was estimated as 5.0 and 3.2 in Figs. 12 (c) and (d), respectively.

5. Discussions

In this study, a 1-mT ULF-MRI system without a pre-polarization technique was proposed and the feasibility of MRI measurement was demonstrated. The static magnetic field was set to 1 mT to balance the intensity of the MR signal and the compatibility for integrating with the MEG system. This attempt is the first to achieve ULF-MRI measurements at approximately 1 mT[1].

The highest static magnetic field with the B_p-pulse and the lowest without the B_p-pulse were 200 μT [13] and 6.5 mT [2, 22], respectively. Compared with these MRI systems, the proposed 1-mT MRI system does not require large-scale equipment, such as a larger power supplier or cooling system for the coils. The power consumption necessary to generate the B_p-pulse of 100 mT and B_0 of 6.5 mT were 14.8 kW[13] and 6–7 kW [22], respectively. As described in Subsection 2.3, the power consumption of the 1-mT ULF-MRI system to generate the static magnetic field was 77.2 W. Utilizing the small electric power supply has the benefit of power saving and suppression of magnetic noise interference into the MEG system. This is particularly relevant because the MEG system is sensitive to magnetic noise, including power line noise.

By employing the Merritt-type configuration for the B_0-coil, both weight savings and sufficient homogeneity of the static magnetic field were achieved. The weight of the B_0-coil was approximately 1/10 that of the 6.5-mT MRI system (~ 340 kg[22]). Although the inhomogeneity of 700 ppm was worse than that of the 6.5-mT MRI system (350 ppm), it was negligible for MRI measurement at 1 mT because the robustness against the inhomogeneity was improved by employing a lower static magnetic field, as shown in Figs. 4 (c) and (d).

The suitable homogeneity of B_0 also aided in the reduction of the recording time enabling the use of the GE sequence. Whereas the GE imaging sequence is more easily influenced by the inhomogeneity of the static magnetic field compared with the SE imaging sequence, the MR image obtained using the GE sequence is not distorted, as shown in Fig. 12. In the GE imaging sequence, the repetition time T_R was set to less than the longitudinal relaxation time T_1, which is suitable for fast imaging. The recording time with the GE sequence was 1/3.5 shorter than that with the SE sequence. Furthermore, using the B_p-pulse requires $T_R > T_1$ (normally more than 4–5 times), even when using the GE sequence. It is because the exposure time of the B_p-pulse has to be longer than T_1 (normally more than 2–3 times). Therefore, the recording time of the ULF-MRI can be reduced by avoiding the use of a B_p-pulse.

The spatial resolution and SNR of the obtained MR images were 4 mm and 3.2–5.0, respectively. Although the B_p-pulse was not used to boost the MR signal, the resolution and SNR were comparable with those of previous studies that used the B_p-pulse to combine MEG systems [11, 13]. However, the SNR must be considerably improved to realize three-dimensional MR imaging and reduce the recording time for practical use in human heads. In this study, an induction coil was used instead of the SQUID sensors of the MEG system to detect MR signals. As described in Subsection 2.5, the noise level of the detection unit composed of the induction coil and amplifiers (3.6 fT/Hz$^{1/2}$) was comparable to that of SQUID sensors (approximately 5 fT/Hz$^{1/2}$) [21]. Although the SNRs of single sensors are comparable, it is expected that using a SQUID sensor array composed of more than 100 SQUID sensors will be effective in improving the SNR of the MR image. Optimization of the sensor array for MRI measurements is underway to realize the integration of ULF-MRI and MEG systems.

The experiments were conducted in a smaller FOV than that of the MEG system to investigate the feasibility of MRI measurements at 1 mT without the B_p-pulse. In the future, we aim to develop larger gradients and RF coils to ensure the homogeneity of B_0 in the entire ROI and expand the FOV for capturing the human head.

6. Conclusion

A ULF-MRI system with a static magnetic field of 1 mT was fabricated for integration with the MEG system. Suitable homogeneity and stability of the static magnetic field were successfully generated using a Merritt-type coil driven by MEG-compatible electronics. MRI measurements at 1 mT without a pre-polarization technique were performed using a phantom. The spatial resolution and signal-to-noise ratio were comparable to those obtained in previous studies using the pre-polarization technique. The signal-to-noise ratio of the MR image must be improved for practical MRI measurements.

Appendix A

In this appendix, the influence of applying a strong magnetic field to SQUIDs and the basis for determining a static magnetic field of 1 mT are presented.

Generally, the critical current of Josephson junctions decreases in a strong magnetic field[23]. This results in the SQUID's inoperative condition in a strong magnetic field because the output voltage of the SQUIDs also decreases following the decrease in the critical current. This decreasing trend depends on the orientation of the magnetic field applied to the SQUID[24].

To investigate the acceptable magnetic flux density of our SQUIDs, the output voltage of the SQUID was measured by applying a DC external magnetic field to the SQUID chip. Fig. A.1 shows the measurement results. The flux–voltage characteristics of the SQUID were observed by applying a small AC magnetic flux signal to the SQUID, as shown in Fig. A.1 (a) and the peak-to-peak values are plotted in Fig. A.1 (b).

Evidently, the output voltage of the SQUID was could be maintained at 90 % of the maximum value of less than 1 mT when an external magnetic field was applied to the SQUID chip in the parallel direction. Attenuation of the SQUID output voltage commonly results in a decrease in the bandwidth of the SQUID sensor. The frequency response of the MEG system showed flatness below 50 kHz without applying a magnetic field [25]. It is estimated that the flatness of the frequency response decreased to approximately 45 kHz at 1 mT owing the attenuation of the output voltage of the SQUID. Therefore, the static magnetic field of the ULF-MRI was set to 1 mT, and the corresponding magnetic resonance frequency was 42.58 kHz.

Appendix B

In this appendix, the simulation algorithm for the ULF-MRI measurement is presented.

B. 1 Definition of simulation voxel and equivalent magnetic moment

The cylindrical simulation models illustrated in Fig. 4 (a) are virtually separated by small voxels. The size of the voxel is 4 × 4 × 4 mm^3, and the total number of voxels (N_{voxel}) is 18768. Assuming that each voxel is filled with water, the density of proton ρ can be given by

$$\rho = \frac{2\rho' N_A}{M_{H2O}}, \tag{A1}$$

where N_A, M_{H2O}, and ρ' are Avogadro's number, molar mass, and molecular density of water, respectively. The spin of the protons in the i th voxel was assumed to be an equivalent magnetic moment $\Delta \boldsymbol{m}_i$. In the thermal equilibrium state with the static magnetic field B_0 applied along the y-axis, $\Delta \boldsymbol{m}_i$ can be expressed as a vector (0, $\Delta m_{0,i}$ 0). The magnitude of the magnetic moment $\Delta m_{0,i}$ can be calculated as

$$\Delta m_{0,i} = \frac{\rho \gamma^2 \hbar^2 \Delta V}{4 k_B T} B, \tag{A2}$$

where $\hbar$, k_B, T, ΔV, and B are the Planck constant, Boltzmann constant, temperature, voxel volume, and magnetic field density, respectively.

B. 2 Precession of the magnetic moment

In the "real" MRI, the orientation of the magnetic moment is controlled by RF pulses, such as 90- and 180-degree pulses. In this simulation, the orientation was changed numerically, that is, the magnetic moment in the thermal equilibrium state (0, $\Delta m_{0,i,}$ 0) changed to (0, 0, $\Delta m_{0,i}$) by applying 90-degree pulse virtually. In the simulation presented in Subsection 2.2, the gradient-

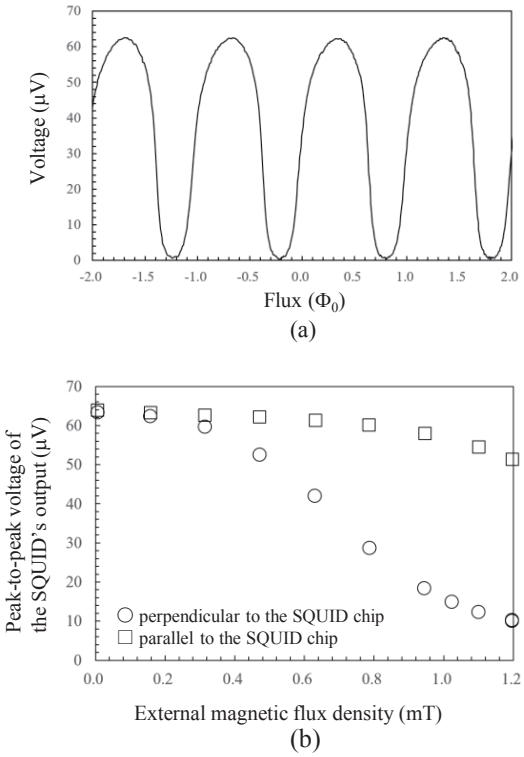

Fig. A.1 Results of the SQUID's output voltage measurement when applying the external magnetic field: (a) flux–voltage characteristic when the external magnetic field was zero, (b) decline curves of the SQUID's output voltage by increasing the external magnetic field.

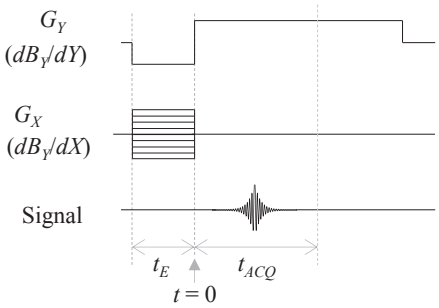

Fig. B.1 Two dimensional gradient echo pulse sequence that is used for the simulation.

echo pulse sequence shown in Fig. B1 was simulated. The gradient fields G_X and G_Y were applied to t_E (8 ms) after applying the virtual 90-degree pulse for 2D imaging. Here, time t = 0 at the end of the phase encoding pulse was defined. The phase shift φ^e_{xz} of the magnetic moment at t = 0 can be expressed as

$$\varphi^e_{xz} = \gamma \times (B_{0,i} + G_Y \cdot r_{i,y} + G_X \cdot r_{i,z}), \tag{A3}$$

where r_i = ($r_{i,x}$, $r_{i,y}$, $r_{i,z}$) is the position of the magnetic moment $\Delta \boldsymbol{m}_i$ and $B_{0,i}$ is the static magnetic field at $\boldsymbol{r}_i$.

The precession of the spin is emulated as the rotation of the magnetic moment vector $\Delta \boldsymbol{m}_i(t)$ = ($\Delta m_{i,x}(t)$, $\Delta m_{i,y}(t)$, $\Delta m_{i,z}(t)$) as follows:

$$\Delta m_{i,y}(t) = \Delta m_{0,i} \times (1 - e^{-(t+t_E)/T_1}) \tag{A4}$$

$$\Delta m_{i,x}(t) = \Delta m_{0,i} \times e^{-(t+t_E)/T_2} \times \sin(\omega_i t + \varphi_{xz}^e) \quad \text{(A5)}$$

$$\Delta m_{i,z}(t) = \Delta m_{0,i} \times e^{-(t+t_E)/T_2} \times \cos(\omega_i t + \varphi_{xz}^e). \quad \text{(A6)}$$

In the above equations, ω_i is the angular frequency of the precession, given by

$$\omega_i = \gamma \times (B_{0,i} + G_Y \cdot r_{i,y}), \quad \text{(A7)}$$

where $B_{0,i}$ is the static magnetic field at each voxel position calculated based on the design of the Merritt-type B_0-coil. T_1 and T_2 are the longitudinal and transverse relaxation times of the samples, respectively. In this simulation, T_1 and T_2 are defined as 70 ms, in accordance with those of the $CuSO_4$ aqueous solution phantom used for the experiments.

B.3 Magnetic resonance signal waveform

The detection coil is also defined, as shown in Fig. 4 (b). The interlinking magnetic flux generated by each equivalent magnetic moment $\Delta\Phi_i(t)$ can be calculated as

$$\Delta\Phi_i(t) = \Delta \boldsymbol{m}_i(t) \cdot \boldsymbol{\beta}_i \quad \text{(A8)}.$$

$\boldsymbol{\beta}_i$ is the lead-field vector given as

$$\boldsymbol{\beta}_i = \frac{\mu_0}{4\pi} \int_{\boldsymbol{l}} \frac{d\boldsymbol{l} \times (\boldsymbol{r}_i - \boldsymbol{q})}{|\boldsymbol{r}_i - \boldsymbol{q}|^3} , \quad \text{(A9)}$$

where μ_0 is the vacuum permeability, $\boldsymbol{l}$ is the path of integration for the detection coil, and $\boldsymbol{q} = (q_x, q_y, q_z)$ is the center of the detection coil.

As the sensor output, the magnetic flux density $B_{detected}$ is calculated as follows:

$$B_{detected}(t) = \frac{1}{A_{coil}} \sum_{i=1}^{N_{voxel}} \Delta\Phi_i(t) , \quad \text{(A10)},$$

where A_{coil} is the area of the detection coil.

The waveform of the simulated magnetic resonance signal can be obtained by calculating every time point between $t = 0$ and t_{ACQ} (16 ms in this simulation) with sampling frequencies of 500 kHz and 2 MHz for B_0 = 1 mT and 10 mT, respectively. To obtain an MR image with 64 × 64 pixels, the calculation was repeated 64 times by changing the intensity of the phase-encoding Gx. The obtained MR waveform data were preprocessed and frequency-converted, and the MR images were reconstructed by applying 2D FFT, similar to the processing of the real experimental data. In this study, the signal-to-noise ratio (SNR) was not considered in the simulation to simply compare the influence of the inhomogeneity of the static magnetic field. To simulate the SNR, the induced voltage of the detection coil can be obtained by multiplying the frequency of the MR signal, and voltage noise can be easily added to the calculated induced voltage data.

Appendix C

As described in Subsection 4.1, the spin-echo (SE) signal was continuously recorded for approximately 4 hours after turning on the current driver for the B_0-coil to confirm the stability of the static magnetic field B_0. Fig. C.1 shows the frequency shift of observed SE signal. The frequency rapidly decreased between 0 and 60 min and then slowly shifted. This frequency shift is assumed to be caused by the time required to stabilize the current driver circuit, including the warm-up time of the circuit elements. The shift from 60 to 240 min was approximately 14 Hz. The corresponding magnetic flux density of B_0 was calculated as 336 nT (0.0336 % of 1 mT).

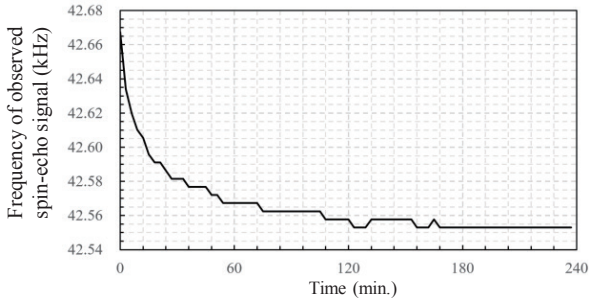

Fig. C.1 Frequency shift of observed spin-echo signal.

Acknowledgements This work was partly supported by JSPS KAKENHI (grant number: 20K12680). This study includes some results of collaborative research with RICOH Co. Ltd. The authors are grateful to Mr. Shinsuke Shibata formerly with RICOH Co., Ltd. for valuable discussions and Ms. Miki Kawabata with the Applied Electronics Laboratory, Kanazawa Institute of Technology, for supporting the experiments. The authors would like to thank Editage (www.editage.jp) for English language editing.

References

1) M. Sarracanie and N. Salameh: *Front. Phys.*, **8**, 172 (2020).
2) M. Sarracanie, C. LaPierre, and N. Salameh: *Sci. Rep.*, **5**, 15177 (2015).
3) M. H. Mazurek, B. A. Cahn, M. M. Yuen, et al.: *Nat. Commun.*, **12**, 5119 (2021).
4) Y. Liu, A. T. L. Leong, Y. Zhao, et al.: *Nat. Commun.*, **12**, 7238 (2021).
5) R. McDermott, A. H. Trabesinger, M. Mück, E. L. Hahn, A. Pines, and J. Clarke: *Science*, **295**, pp. 2247-2249 (2002).
6) R. McDermott, S. K. Lee, B. Haken, A. H. Trabesinger, A. Pines, and J. Clarke: *PNAS*, **101**, pp7857-7861 (2004).
7) J. Clarke, M. Hatridge, and M. Mößle: *Annu. Rev. Biomed. Eng.*, **9**, pp. 389-413 (2007).
8) V. S. Zotev, A. N. Matlashov, P. L. Volegov, I. M. Savukov, and M. A. Espy: *J. Magn. Reson.*, **194**, pp. 115-120, (2008).
9) V. S. Zotev, A. N. Matlashov, I. M. Savukov, et al.: *IEEE Trans. Appl. Supercond.*, **19**, pp.823-826 (2009).
10) J. Luomahaara, P. T. Vesanen, J. Penttilä, et al.: *Supercond. Sci. Technol.*, **24**, 075020 (2011).
11) P. T. Vesanen, J. O. Nieminen, K. C. Zevenhoven, et al.: *Magn. Reson. Med.*, **69**, pp. 1795-1804 (2013).
12) B. Inglis, K. Buckenmaier, P. SanGiorgio, A. F. Pedersen, M. A. Nichols, and J. Clarke: *Proc. Natl. Acad. Sci. USA*, **110**, pp. 19194-19201 (2013).
13) M. A. Espy MA, P. E. Magnelind, A. N. Matlashov, S. G. Newman, et al.: *IEEE Trans. Appl. Supercond.*, **25**, 1601705 (2015).
14) P. Hömmen, J. H. Storm, N. Höfner, and R. Körber: *Magn. Reson. Imag.*, **60**, pp. 137-144 (2019).
15) D. Oyama, J. Hatta, M. Miyamoto, Y. Adachi, J. Kawai, M.

Higuchi, and G. Uehara: *IEEE Trans. Appl. Supercond.*, **23**, 1601604 (2013).
16) D. Oyama, M. Higuchi, J. Kawai, N. Tsuyuguchi, M. Miyamoto, et al.: *2015 15th International Superconductive Electronics Conference (ISEC)*, pp. 1-3 (2015).
17) K. C. J. Zevenhoven, H. Dong, R. J. Ilmoniemi, and J. Clarke: *Appl. Phys. Lett.*, **16**, 034101 (2015).
18) Y. Hatsukade, T. Abe, S. Tsunaki, M. Yamamoto, H. Murata, and S. Tanaka: *IEEE Trans. Appl. Supercond.*, **23**, 1602204 (2013).
19) R. Merritt, C. Purcell, and G. Stroink: *Rev. Sci. Inst.*, **54**, pp. 879-862 (1983).
20) J. L. Kirschvink: *Bioelectromagnetics*, **13**, pp. 401-411 (1992).
21) H. Kado, M. Higuchi, M. Shimogawara, Y. Haruta, Y. Adachi, et al.: *IEEE Trans. Appl. Supercond.*, **9**, pp. 4057-4062 (1999).
22) L. L. Tsai, R. W. Mair, M. S. Rosen, S. Patz, and R. L. Walsworth: *J. Magn. Reson.*, **193**, pp. 274-285 (2008).
23) J. M. Rowell: *Phys. Rev. Lett.*, **11**, pp. 159-160 (1963).
24) J. Kawai, M. Kawabata, and D. Oyama: Extended Abstract of The 82nd JSAP Autumn Meeting 2021, 11p-N403-1, September 2021, Nagoya, Japan (in Japanese).
25) D. Oyama, Y. Adachi, M. Higuchi, J. Kawai, M. Miyamoto, et al.: *J. Magn. Soc. Jpn.*, **36**, 345-351 (2012).

Received Jan. 11, 2023; Revised Feb. 27, 2023; Accepted Mar. 28, 2023.

Editorial Committee Members・Paper Committee Members

Notice for Photocopying

編集委員・論文委員

複写をされる方へ

Journal of the Magnetics Society of Japan

Vol. 47 No. 4 (通巻第328号) 2023年7月1日発行

Vol. 47 No. 4 Published Jul. 1, 2023
by the Magnetics Society of Japan
Tokyo YWCA building Rm207, 1–8–11 Kanda surugadai, Chiyoda-ku, Tokyo 101–0062
Tel. +81–3–5281–0106 Fax. +81–3–5281–0107

Printed by JP Corporation Co., Ltd.
Sports Plaza building 401, 2–4–3, Shinkamata Ota-ku, Tokyo 144–0054
Advertising agency: Kagaku Gijutsu-sha

発行：(公社)日本磁気学会 101–0062 東京都千代田区神田駿河台 1–8–11 東京YWCA会館 207 号室
製作：ジェイピーシー 144–0054 東京都大田区新蒲田 2–4–3 スポーツプラザビル401 Tel.（03）6715–7915
広告取扱い：科学技術社 111–0052 東京都台東区柳橋 2–10–8 武田ビル 4F Tel.（03）5809–1132